Experimental study of a human-like exhaled airflow configuration and droplets dynamics in indoor environment

Khansa Mahjoub Mohammed Merghani

Dissertation presented to obtain Doctoral degree from
Université Paris-Est Créteil
École doctorale Sciences, Ingénierie et Environnement
Specialty: Environmental Science and Technology

Experimental study of a human-like exhaled airflow configuration and droplets dynamics in indoor environment

by
Khansa MAHJOUB MOHAMMED MERGHANI

Thesis director: Evelyne Géhin
Supervisor: Benoit Sagot
Co-supervisor: Charles Motzkus

Members of defense committee:
Prof. Laurence Le Coq (IMT Atlantique, Nantes)
Prof. Dominique Thomas (Université de Lorraine)
Dr. Jeanne Malet (IRSN)
Prof. Evelyne Géhin (UPEC)
Dr. Benoit Sagot (ESTACA)
Dr. Charles Motzkus Co-supervisor (CSTB

Abstract

The infection rates of the coronavirus disease 2019 pandemic revealed the gaps in our understanding of the transmission of airborne diseases. In literature, both short-range transfer of pathogens by droplets, and long-range transfer by airborne dry residues were studied. However, the results are contradictory, and the role of each of these transmission routes is not clear. This was translated to ineffective control measures at the beginning of the pandemic. The research gap in the transmission of infectious diseases is linked to the lack of quantitative data about the physics of human exhalation in gaseous and droplet phases. This study started with a comprehensive literature review on the experimental techniques applied to the characterization of the exhaled air flow and droplets. A new methodology is proposed to tackle the problem using a non-intrusive measurement technique to explore the droplets dynamics in a well-defined gas flow field and providing quantitative data. The objective of this study is to analyze the evolution of the droplet size and droplet velocity with respect to distance. The experiment comprises two parts: airflow field measurements and droplet measurements. The first part targets the characterization of the airflow field in terms of the velocity field and turbulence. While the droplets' part studies the change of the size and velocity in this flow field at different distances from the source. The measurements were conducted inside an environmental chamber (2.7 m x 2.0 m x 3.0 m) that is designed as part of this study. Air is injected inside this chamber at a temperature of 34°C and humidity of more than 95% through a nozzle of 1 cm diameter. In the first part of the experiment, DEHS was used as a tracer to characterize the airflow velocity field using a two-component Laser Doppler Anemometry (LDA) and Phase Doppler Anemometry (PDA) system. In the of 0.8 m, we identified the jet characterizing parameters, namely, centerline velocity decay, axial and radial velocity profiles, in addition to the turbulent intensity. For the study of the droplets, the airflow is laden with 48 µm monodispersed droplets of NaCl-water solution. The analysis of the droplet dynamics is carried out by exploring the change of droplet size and velocity in the horizontal axis and vertical profiles at a distance up to 0.4 m from the jet source. In this range, the effect of the droplet evaporation on the size distribution was not observed.

Résumé

Les taux d'infection de la pandémie de coronavirus de 2019 ont révélé les lacunes de notre compréhension de la transmission des maladies par voie aérienne. Dans la littérature, le transfert à courte distance des agents pathogènes par les gouttelettes et le transfert à longue distance par les résidus secs en suspension dans l'air ont été étudiés. Cependant, les résultats sont contradictoires, et le rôle de chacune de ces voies de transmission n'est pas clair. Cela s'est traduit par des mesures de contrôle inefficaces au début de la pandémie. Les lacunes de la recherche sur la transmission des maladies infectieuses sont liées au manque de données quantitatives sur la physique de l'exhalation humaine en phases gazeuse et de gouttelettes. Cette étude a commencé par une revue détaillée de la littérature sur les techniques expérimentales appliquées à la caractérisation du flux d'air expiré et des gouttelettes. Une nouvelle méthodologie est proposée pour aborder le problème en utilisant une technique de mesure non intrusive pour explorer la dynamique des gouttelettes dans un champ d'écoulement gazeux bien défini et fournir des données quantitatives. L'objectif de cette étude est d'analyser l'évolution de la taille et de la vitesse des gouttelettes en fonction de la distance. Cette étude comprend deux parties : les mesures du champ d'écoulement de l'air et les mesures des gouttelettes. La première partie vise à caractériser le champ d'écoulement de l'air en termes de champ de vitesse et de turbulence. Alors que la partie concernant les gouttelettes étudie le changement de la taille et de la vitesse dans ce champ d'écoulement à différentes distances de la source. Les mesures ont été effectuées à l'intérieur d'une chambre environnementale (2,7 m x 2,0 m x 3,0 m) qui est conçue dans le cadre de cette étude. L'air est injecté à l'intérieur de cette chambre à une température de 34°C et une humidité de plus de 95% à travers une buse de 1 cm de diamètre. Dans la première partie de l'expérience, le DEHS a été utilisé comme traceur pour caractériser le champ de vitesse de l'écoulement d'air à l'aide d'un système d'anémométrie Doppler laser (LDA) et d'anémométrie Doppler phase (PDA) à deux composantes. Dans l'espace de 0,8 m, nous avons identifié les paramètres caractérisant le jet, à savoir la décroissance de la vitesse sur la ligne centrale, les profils de vitesse axiale et radiale, ainsi que l'intensité turbulente. Pour l'étude des gouttelettes, le flux d'air est chargé de gouttelettes monodispersées de 48 µm de solution NaCl-eau. L'analyse de la dynamique des gouttelettes est effectuée en explorant le changement de la taille et de la vitesse des gouttelettes dans l'axe horizontal et les profils verticaux à une distance allant jusqu'à 0,4 m de la source du jet. Dans cette plage, l'effet de l'évaporation des gouttelettes sur la distribution de taille n'a pas été observé.

Table of contents

Table of contents ..... *v*

Table of figures ..... *ix*

Table of tables ..... *xiii*

Introduction *14*

Chapter 1 Literature review *18*

Abstract *20*

1.1 Introduction **21**

1.2 Characterization of the exhaled airflow **22**

1.2.1 Global flow-field measurements 22

1.2.1.1 High Speed Photography 25

1.2.1.2 The schlieren photography 27

1.2.1.3 Particle Image Velocimetry 28

1.2.2 Pointwise measurements 31

1.3 Measurements on the exhaled droplets **36**

1.3.1 Intrusive measurement techniques 40

1.3.1.1 Solid impaction 40

1.3.1.2 Droplet deposition analysis 41

1.3.1.3 Optical Particle Counter 42

1.3.1.4 Aerodynamic Particle Sizer 43

1.3.1.5 Other techniques 44

1.3.2 Nonintrusive measurement techniques 45

1.3.2.1 High-speed photography 45

1.3.2.2 Digital Inline Holography 46
1.3.2.3 Laser measurement techniques based on Mie theory 46
1.4 Comment on disease transmission 48
1.5 Conclusion 48
1.6 References 49
1.7 The turbulent round jet 54
1.7.1 Centerline velocity decay 56
1.7.2 Mean velocity profiles 58
1.7.3 Jet spread angle 60
1.8 Buoyant jet 62
1.9 Droplet dynamics 64
1.10 Summary and conclusions 66
Chapter 2 Experimental study of human-like horizontal jet 68
2.1 Experimental bench 69
2.1.1 Environmental chamber 70
2.1.2 LDA measurement system 76
2.1.3 Seeding particles 78
2.1.4 Jet generation 81
2.2 Definition of the measurement procedure 84
2.2.1 Measurement and data acquisition 84
2.2.2 Data treatment 86
2.2.3 Defining the point of origin (0,0,0) 87
2.2.4 Experimental campaigns 87
2.2.4.1 The Isothermal jet campaign: 87
2.2.4.2 Buoyant jet campaign: 89

2.2.5 Definition of the measurement procedure 90

2.3 Results 96

2.3.1 Isothermal jet 97

2.3.1.1 Centerline velocity decay 97

2.3.1.2 Mean velocity profiles of the isothermal jet 99

2.3.1.3 The spread angle for the isothermal 104

2.3.1.4 Turbulence 104

2.3.2 Buoyant jet 108

2.3.2.1 Buoyant jet centerline 108

2.3.2.2 From isothermal to buoyant jet model 109

2.3.2.3 Centerline velocity decay 114

2.3.2.4 Mean velocity profiles 114

2.3.2.5 Turbulence of the buoyant jet 118

2.4 Summary and conclusions 119

Chapter 3 Experimental study on the dynamics of droplets in a human-like horizontal jet 121

3.1 Experimental Bench 123

3.1.1 Laser Doppler Anemometry and Phase Doppler Anemometry 124

3.1.2 Aerodynamic Particle Sizer (APS) 124

3.2 The oropharyngeal emission simulator (OES) 124

3.2.1 The conventional use of the Vibrating Orifice Aerosol Generator 125

3.2.2 The second version of the oropharyngeal emission simulator (OES V.2) 128

3.3 Procedure 132

3.3.1 VOAG operation 132

3.3.2 The stability of the jet initial conditions 133

3.3.3 The temperature and humidity along the jet horizontal axis 137

3.3.4 Measurements of droplets size and velocity in a humid jet 138

3.4 Results on dynamics of the NaCl-water solution droplets 140

3.4.1 The velocity of the droplets 140

3.4.2 The evolution of the droplets size along the centerline 142

3.4.3 Measurements of the droplets on the vertical profiles 150

3.5 Results on the dry residue of the NaCl-water solution droplets 157

3.6 Conclusion 159

Chapter 4 161

General conclusion and perspectives 161

Nomenclature 167

References 171

Annexes 176

Annex A: The count distribution of the droplet at the nozzle exit 177

Annex B: The APS measurements of the dry residues of the NaCl-water solution droplets 180

Table of figures

Figure 0.1 : The transmission routes of airborne diseases [Wei et al. 2016] _____ *15*

Figure 2: The change of exhaled droplets size distribution with distance. _____ *36*

Figure 0.3 : The entrainment of the ambient air inside the turbulent round jet _____ *54*

Figure 0.4 : Subsequent snapshots of a round air jet with Re ≈ 5000 issuing into air at rest, with a time interval of 5 ms. [Orlu, 2009] _____ *55*

Figure 0.5 : The geometry of the turbulent round jet _____ *56*

Figure 0.6 : The evolution of the centerline velocity with distance from the jet source at different Re [Papadopoulos and Pitts, 1999] _____ *58*

Figure 0.7 : The axial velocity component of the turbulent round jet _____ *59*

Figure 0.8 : The radial velocity component of the turbulent round jet _____ *60*

Figure 0.9 : The jet spread angle and the jet half-width _____ *61*

Figure 0.10 : The horizontal buoyant turbulent jet _____ *64*

Figure 0.11 : The evolution of Stokes number with distance from the jet inlet for different droplet sizes. [Ferrand et al, 2003] _____ *66*

Figure 0.1 : Experimental bench _____ *70*

Figure 0.2 : Schematic diagram of experimental setup _____ *71*

Figure 0.3 The velocity field obtained by CFD with initial jet velocity of 10 m.s^{-1} _____ *73*

Figure 0.4 The decay of centerline velocity for three boundary conditions with at an initial velocity of 10 m.s^{-1} _____ *74*

Figure 0.5 The deflection of the jet centerline for jet initial temperature of 34°C, ambient temperature of 20°C, and initial air velocity of 1 m.s-1 _____ *74*

Figure 0.6 The environmental chamber _____ *76*

Figure 0.7 The working principle of the Laser Doppler Anemometry [DANTEC, 2020] _____ *77*

Figure 0.8 The two components Laser Doppler Anemometry system from Dantec _____ *78*

Figure 0.9 The oil mist generator used to seed the jet with DEHS microdroplets. _____ *79*

Figure 0.10 : A Cut view of the Laskin nozzle _____ *79*

Figure 0.11 : Visualization of aerosol formation by Laskin nozzle [Kähler et al. 2002] _____ *80*

Figure 0.12 : The size distribution of the DEHS droplets produced by the generator at the jet exit (0.003, 0, 0) _____ *80*

Figure 0.13 : The axial and radial velocity of the generated DEHS droplet at the center of the nozzle exit (0.003, 0, 0) 81

Figure 0.14: The jet generation and the definition of the jet axis 82

Figure 0.15 The geometry of the jet exit nozzle 83

Figure 0.16 The velocity profile at ≈5mm from the jet exit (0.003, 0 , 0) 84

Figure 0.17 Axial velocity along the jet centerline at 0.05m from the source (0.053, 0, 0) 85

Figure 0.18 Axial velocity distribution on the jet centerline at 0.05m from the source (0.053, 0, 0) 86

Figure 0.19 The measurement points along the jet centerline 88

Figure 0.20 The measurement points for the six velocity profiles 89

Figure 0.21 The axial velocity profiles at 0.05 m, 0.1 m, 0.2 m, 0.4 m, 0.6 m, and 0.8 m from the exit nozzle. 91

Figure 0.22 The vertical profiles at 0.05 m, 0.1 m, 0.2 m, 0.4 m, 0.6 m, and 0.8 m from the exit nozzle. 93

Figure 0.23 change of the average vertical and axial velocity with the number of samples at 0.05m 94

Figure 0.24 change of the average vertical and axial velocity with the number of samples at 0.8m 95

Figure 0.25 change of the average vertical and axial velocity with the number of samples at 0.8m with the improved measurement procedure 96

Figure 0.26 The decay of centerline velocity at an initial velocity of 5 m.s^{-1} 98

Figure 0.27 The evolution of the centerline velocity with distance from the jet source 99

Figure 0.28 The axial velocity profiles at 0.05 m, 0.1 m, 0.2 m, 0.4 m, 0.6 m, and 0.8 m from the exit nozzle. 100

Figure 0.29 The normalized axial velocity profiles and comparison with literature studies 101

Figure 0.30 The vertical profiles at 0.05 m, 0.1 m, 0.2 m, 0.4 m, 0.6 m, and 0.8 m from the exit nozzle. 102

Figure 0.31 The normalized vertical profiles compared to Falcone and Cataldo [2003]. 103

Figure 0.32 The turbulence intensity at 0.05 m, 0.1 m, 0.2 m, 0.4 m, 0.6 m, and 0.8 m from the exit nozzle. 105

Figure 0.33 The Axial component of the turbulence kinetic energy. 106

Figure 0.34 The turbulence radial velocity profiles 107

Figure 0.35 : The centerline of the buoyant jet 109

Figure 0.36 The length of the centerline (s) of the buoyant jet 110

Figure 0.37 The rotating the profile baseline from point A to point B 111

Figure 0.38 The translation of the baseline from point B to point C 112

Figure 0.39 The rotation of the velocity vectors in the buoyant jet 113

Figure 0.40-a: Isothermal flow velocity profiles 113

Figure 0.41 The decay of centerline velocity of the buoyant jet ____ *114*

Figure 0.42 The axial velocity component U_x for the buoyant jet ____ *115*

Figure 0.43 The radial velocity component U_z for the buoyant jet ____ *117*

Figure 0.44 The axial component of the turbulence kinetic energy of the buoyant jet ____ *118*

Figure 0.45 The radial component of the turbulence kinetic energy of the buoyant jet ____ *119*

Figure 0.1 The motion and evaporation of a droplet in a humid buoyant turbulent jet ____ *122*

Figure 0.2 The experimental bench for the droplet dynamics study ____ *123*

Figure 0.3: The break-up of liquid jet into uniform droplets [TSI, 2013] ____ *126*

Figure 0.4: The Vibrating Orifice Aerosol Generator from TSI ____ *127*

Figure 0.5: The second version of the oropharyngeal emission simulator ____ *128*

Figure 0.6: The size distribution of the droplet with dry dispersion airflow at nozzle exit (x=0.003 m, y=0, z=0) of 30 minutes count ____ *129*

Figure 0.7: The size distribution of droplets larger than 10 µm with dry dispersion airflow at nozzle exit (x=0.003 m, y=0, z=0) of 30 minutes count ____ *130*

Figure 0.8: The size distribution of the droplet without dispersion airflow at (x=0.003 m, y=0, z=0) of 30 minutes count ____ *131*

Figure 0.9: A photograph taken at the nozzle entry shows condensation on the nozzle's inner surface. *131*

Figure 0.10: VOAG deflection test [Zambrelli, 2014] ____ *133*

Figure 0.11: The initial exit temperature of the humid air and the environmental chamber temperature monitored for two hours experiment ____ *134*

Figure 0.12: The mean axial and radial velocity for the droplets of different sizes at nozzle exit (x=0.003 m, y=0, z=0) for 100 minutes count ____ *135*

Figure 0.13 The mean axial velocity of the droplet less than and more than 7 µm, at the nozzle exit (x=0.003 m, y=0, z=0) for 100 minutes count ____ *136*

Figure 0.14 The temperature along the jet horizontal axis (0.003, 0, 0) to (0.4, 0, 0) ____ *137*

Figure 0.15 The humidity along the jet horizontal axis (0.003, 0, 0) to (0.4, 0, 0) ____ *138*

Figure 0.16 The location of the measurement points using PDA/LDA ____ *139*

Figure 0.17 The mean axial velocity of the droplets over 0.05 m along the jet centerline ____ *141*

Figure 0.18 The mean axial velocity of the droplets over 0.4 m along the jet centerline ____ *142*

Figure 0.19 The change of count distribution of the droplets <10µm along 0.05 m of the jet centerline. (E1, measurement time at each point: 15 mins) ____ *144*

Figure 0.20 Comparison between the droplet count of the droplets <10µm along 0.05 m of the jet centerline. (measurement time at each point: 15 mins) ____ *145*

Figure 0.21 change of count distribution of the droplets 35 µm – 70 µm along 0.05 m of the jet centerline. (E1, measurement time at each point: 15 mins) ____ *146*

Figure 0.22 The change of count distribution of the droplets <10µm along 0.4 m of the jet centerline. (E2, measurement time at each point: 15 mins) _____ *148*

Figure 0.23 The change of count distribution of the droplets 35 µm – 70 µm along 0.1 m of the jet centerline. (E2, Measurement time at each point: 15 mins) _____ *149*

Figure 0.24 The number of the droplets along the vertical profile at x= (0.05m + 0.003m) from the exit (Measurement time at each point: 15 mins) _____ *150*

Figure 0.25 The size distribution along the vertical profile at x= (0.05m + 0.003m) from the exit at η=-0.8, -0.4, 0, 0.4, 0.8 (E3, measurement time at each point: 15 mins) _____ *152*

Figure 0.26 The number of the droplets along the vertical profile at x= (0.1m + 0.003m) from the exit (Measurement time at each point: 15 mins) _____ *153*

Figure 0.27 The number of the droplets along the vertical profile at x= (0.15m + 0.003m)from the exit (Measurement time at each point: 15 mins) _____ *153*

Figure 0.28 The count distribution along the vertical profile at x= (0.1m + 0.003m) from the exit at η=-0.8, -0.4, 0, 0.4, 0.8 (E4, measurement time at each point: 15 mins) _____ *154*

Figure 0.29 The count distribution along the vertical profile at x= (0.15m + 0.003m) from the exit at η=-0.8, -0.4, 0, 0.4, 0.8 (E5, measurement time at each point: 15 mins) _____ *155*

Figure 0.30 The number of the droplets along the vertical profile at x= (0.2m + 0.003m)from the exit (Measurement time at each point: 15 mins) _____ *156*

Figure 0.31: The concentration of the particles inside the environmental chamber before starting the VOAG generation (background) and during the experiment. (Measurement duration:15 mins) _____ *157*

Figure 0.32: Prediction of the initial NaCl-water solution droplets from the size of the dry residues __ *158*

Table of tables

Table 01 The main measured parameters of the experimental studies on the characterization of human exhaled airflow. _____ *23*

Table 2: The direction and the spread angle of the exhalation jet from the literature _____ *26*

Table 3: The characteristics of the artificially produced jets and the measured parameters _____ *34*

Table 4: The techniques used for the characterization of the respiratory droplets _____ *38*

Table 0:1 The boundary conditions of three simulations performed to investigate the effect of chamber length on jet propagation. _____ *72*

Table 0:2 : The MAPD values for the mean axial velocity profiles at 0.05 m, 0.1 m, 0.2 m, 0.4 m, 0.6 m, and 0.8 m from the exit nozzle. _____ *92*

Table 0:3 : The initial conditions of the isothermal jet. _____ *97*

Table 0:4: characteristic coefficients and parameters of the buoyant jet _____ *108*

Table 0:5: The effect of the change of the jet and ambient temperature in the vertical position of the jet centerline at x=0.8m _____ *116*

Table 0:1 The jet initial conditions and the set parameters _____ *136*

Table 0:2 The conducted experimental campaigns _____ *140*

Table 0:1 The APS measurements of the dry residues of the NaCl-water solution droplets for E1,E2, E3, E4, E5, and E6. _____ *183*

Introduction

The exhalation activities involve breathing, speaking, coughing, and sneezing, in addition, singing, and playing wind instruments can also be considered as exhalation activities. During each of these activities, air passes through the respiratory tract at a certain velocity that depends on the type of activity and on the person's physiology. This passage of air exerts shear forces on the surface of the respiratory tract, which results in fluid breakage. Hence, the air exhaled from the different exhalation activities is laden with droplets of different sizes originated from different parts of the respiratory tract.

In the case of infected person, these droplets encapsulate the pathogens that exist in the respiratory tract and then they are emitted with the exhaled air. The factors affecting the transmission of these pathogens from the infected host to the inhalation zone of a new host are:

First, the emission parameters, which involves.

1. The biological, chemical, and physical characteristics of the emitted droplets.
2. The initial conditions of the airflow namely, velocity, temperature, and humidity in addition to direction.

Second, the airflow field, which results from the interaction of the exhaled airflow and the ambient environment.
Third, the droplet dynamics and its interaction with the airflow.

Depending on the above-mentioned factors, the transmission routes from host to host are classically classified into three main categories: surface transmission, aerosol transmission, and droplet transmission. Figure 0.1 illustrates these three transmission routes of the pathogens-laden droplets.

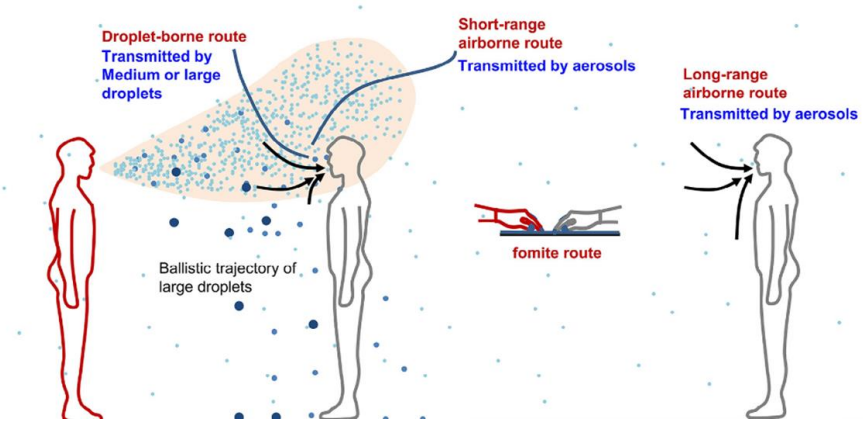

Figure 0.1 : The transmission routes of airborne diseases [Wei et al. 2016]

Depending on the droplet's dynamics and dispersion, droplet can settle on the surrounding surfaces and when the infection is transmitted by contacting the contaminated surface this is referred to as a surface contact route. Droplet transmission is considered when the droplets travel directly from the respiratory tract of the infectious individual to the susceptible mucosal surfaces of the recipient. While aerosol transmission corresponds to long-distance travel of the droplet which involves evaporation and the likelihood of forming dry residues that transmit droplets from an infectious host to a new host over long distance, classically defined as more than 2 m. Well [1934] suggested a cutoff diameter of 5µm between the droplet and aerosols transmission routes. This cutoff size is based on the fact that droplets of less than 5µm tend to follow the air flow closely.

In the last two years, the Covid19 pandemic resulted in more than 180 million infection cases, and 3.9 million unfortunate deaths. The Covid19 as the other respiratory infections can be transmitted via these three routes. When the pandemic started, the role of aerosol transmission was unclear, and public health policies relied on controlling the droplet transmission route. However, as the infection rates continued to rise, the gaps in our understanding of airborne pathogens transmission were revealed. The droplet dynamics in a flow field such as the one resulting from the interaction of human exhalation and ambient environment are not yet comprehensively studied.

Experimental as well as numerical studies have been conducted to characterize this flow field as well as to track the physical history of these droplets. The first part of this Ph.D. project reviewed the experimental techniques that have been used to study both the flow field and the exhaled droplets. The aim of this review is to analyze the available experimental data and to critically compare the measured parameters each of these techniques can provide. This literature review is published [1], and a preprint version is presented in the Chapter 1. This review concluded that more experimental studies are required to bridge the existing research gaps as well as providing experimental data for validation of numerical studies. This leads us to the major research question this research aims to answer:

How do droplets behave in a flow field with the same velocity, temperature, and humidity as the humid exhaled jet?

To answer this question, a steady turbulent round air jet of 5 $m.s^{-1}$ initial velocity corresponding to the initial velocity of the air exhaled during speaking is injected inside a room, referred to as

[1] Mahjoub Mohammed Merghani K, Sagot B, Gehin E, Da G, Motzkus C. A review on the applied techniques of exhaled airflow and droplets characterization. Indoor air. 2021 Jan;31(1):7-25. DOI: 10.1111/ina.12770.

an environmental chamber in this thesis. The air is injected through a nozzle of 1 cm diameter at a temperature of 34°C and humidity of more than 95%. The airflow is laden with 48 µm monodispersed droplets of NaCl-water solution droplets. These droplets were generated using an oropharyngeal emission simulator ORS V.2. This generator is an upgrade of the ORS V.1 that was developed in the frame of the Primequal program entitled "Study of the environmental determinants of viral exposure: application to the monitoring and management of respiratory viruses in classrooms". The simulator has been designed to primarily allow the generation of droplets in moisture-saturated air at different centerline emission velocities of the jet. Laser doppler anemometry and phase Doppler anemometry were used to characterize both the airflow field and the size and the velocity of the droplet at different locations from the source nozzle. In addition to the air velocity evolution, we are also looking for notions of evaporation in the near field.

Thesis structure

Chapter 1 is a literature review with three sections. The first section provides a review of experimental studies on the characterization of human exhalation. The second section gives a physical description of the turbulent round jet. Finally, the third section describes the dynamics of droplets in a turbulent flow.

Chapter 2 provides a description of the built experimental setup and explains its conception and design. Following this experimental setup presentation, an explanation of the measurement procedure adopted to characterize airflow is given. Measurements of an isothermal jet were first conducted to be compared to the existing models. Then measurements of the turbulent round buoyant jet configuration are presented in the second phase of the experiment. The characterization of the jet in terms of mean axial velocity, mean horizontal velocity, and turbulence is discussed in the result section.

Chapter 3 aims at analyzing the dynamics of the exhaled droplets. First, it presents the oropharyngeal emission simulator that is developed to produce the monodispersed NaCl-water solution droplets. Then it details the implemented experimental procedure using the LDA /PDA system to measure the droplet's velocity and diameter. Finally, in the results section, the change in droplets' size and velocity with distance from the source is analyzed.

Chapter 1
Literature review

The study of the dynamics of human exhalation is of particular interest in the comprehension of airborne disease transmission. The complexity of the dispersion of the human exhaled droplets has two sides; the first is the intermittence of the jet which is not yet comprehensively investigated. The second problem is the behavior of the droplets in fluid flow with the same turbulence levels and temperature and humidity fields. The focus of this study is on the second problem, where we are trying to investigate the motion and evaporation of droplets in a constant jet with the same exit humidity and temperature as the human exhalation.

The first section of this chapter focuses on human exhalation and the experimental techniques applied to characterize it. The second section is dedicated to providing a physical description of the turbulent round jet and particle dynamics.

A review on the applied techniques of exhaled airflow and droplets characterization

Khansa MAHJOUB MOHAMMED MERGHANI[1], Benoit SAGOT[2], Evelyne GEHIN[1], Guillaume DA[1] and Charles MOTZKUS[3]

[1]Univ Paris Est Creteil, CERTES, F-94010 Creteil, France

[2]ESTACA, 12 Avenue Paul Delouvrier, 78180 Montigny-le-Bretonneux, France

[3]CSTB, 84 Avenue Jean Jaurès, Champs-sur-Marne, 77447 Marne-la-Vallée Cedex 2, France

Abstract

In the last two decades, multidisciplinary research teams worked on developing a comprehensive understanding of the transmission mechanisms of airborne diseases. This article reviews the experimental studies on the characterization of the exhaled airflow and the droplets, comparing the measured parameters, the advantages, and the limitations of each technique. To characterize the airflow field, the global flow field techniques -High-speed photography, schlieren photography and PIV- are applied to visualize the shape and propagation of the exhaled airflow and its interaction with the ambient air, while the pointwise measurements provide quantitative measurements of the velocity, flow rate, humidity and temperature at a single point in the flow field. For the exhaled droplets, intrusive techniques are used to characterize the size distribution and concentration of the droplets' dry residues while non-intrusive techniques can measure the droplet size and velocity at different locations in the flow field. The evolution of droplets' size and velocity away from the source has not yet been thoroughly experimentally investigated. Besides, there is a lack of information about the temperature and humidity fields composed by the interaction of the exhaled airflow and the ambient air.

Practical implications:

This literature review discusses the applied experimental techniques and how these techniques are relevant to the characterization of the exhaled airflow and droplets. It is required to conduct future experimental research regarding the interaction of exhaled droplets with the surrounding airflow as well as droplet evaporation. It would help to have a more comprehensive understanding of the host-to-host infection transmission, and ultimately assess the different transmission routes.

Keywords: exhaled airflow, respiratory droplets, experimental techniques, dry residues, flow field characterization, particle-laden flows

1.1 Introduction

Morawska and Milton[1] recently published a commentary to the international community titled "It Is Time to Address Airborne Transmission of COVID-19". This statement which was supported by 239 scientists confirms that breathing, speaking, and coughing generate sufficient amount of small droplets to travel further than 2 m from the source. Likewise, in a systematic literature review by Bahl et al.[2] eight analyzed articles (out of ten) concluded that the exhaled droplets could travel horizontally for more than 2m from the source. In addition to that, a retrospective analysis on infection transmission between three families in a Chinese restaurant confirmed the hypothesis of long-distance transmission of COVID-19 [3]. The epidemiological data of this analysis showed that 10 subjects seated in three neighboring tables were infected, although the video record showed no close contact or fomite contact. Another analysis [4] of a superspreading event of COVID-19 in a choral rehearsal confirms the likability of this airborne transmission mode. In this event, 53 members out of 61 confirmed or strongly suspected to have contracted COVID-19. Moreover, cases of COVID19 spread in family clusters[5–7] and among healthcare staff[8] in close contact with patients are associated with droplet transmission. Ong et al.[9] detected the presence of COVID 19 virus in a patient's room, and all the tested samples were contaminated with the virus. According to Doremalen et al.[10], the virus remains viable for 4-72 h on surfaces. The relative contribution of these transmission modes to the spread of the epidemy is still a controversial issue.

Special attention has been paid to the transmission mechanisms of the airborne pathogens after the emergence of novel airborne diseases, such as SARS in 2003 and H1N1 influenza in 2009. Thus, researchers in the fields of aerosol science, indoor air quality and public health conducted experimental, numerical, and theoretical studies to analyze the transport of the exhaled droplets responsible for the transmission of such diseases. The exhaled droplets are formed by the shear force caused by the passage of the airflow in the respiratory tracts while coughing, sneezing, breathing and speaking [11]. These droplets vary in size and in composition which depend on their origin in the respiratory tracts [11]. In the case of a respiratory tract infection, the droplets carry the infectious pathogens from the tract of the infected subject and possibly transmit those to healthy individuals. Therefore, transmission can occur through three different modes of transmission. The first mode occurs via direct contact with the surface-deposited respiratory secretions of the infected person. In the second mode, the infection transmission occurs when respiratory droplets carrying infectious pathogens " travel directly from the respiratory tract of the infectious individual to susceptible mucosal surfaces of the recipient" [12]. The third mode corresponds to long distance travel of the dry

residues which results from the evaporation of the droplets. Such dry residues can transmit the infection between two individuals" who have not had face-to-face contact or been in the same room" [12]. The relative importance of each of these modes depends on the motion and evaporation of the exhaled droplets. Therefore, the prediction of their motion and evaporation in an air jet, which requires a relevant/good coupling with humidity, temperature, and velocity fields, remains a challenging issue. The structure of humidity, temperature, and velocity fields depend on the complex interaction between the human environment (namely exhaled and inhalation airflows, human body plume) and the room surrounding environment [13]. Considering this complex interaction, experimental studies from the literature can be classified into two main categories which depend on the scope of the study. The first category corresponds to studies focusing on the movement and evaporation of the exhaled droplets in the human microenvironment. While the second category includes the numerical and experimental studies that consider the ventilation systems at the room scale and investigating its influence on the droplet dispersion. This review focuses on the first category and analyzes the experimental techniques applied for the characterization of exhaled airflows and droplets. The first part of this review is dedicated to the measurement systems involved in the exploration of the gaseous exhaled flow, while the second part concerns the techniques applied to respiratory droplets.

1.2 Characterization of the exhaled airflow

This section reviews the published papers concerning the applied measurement techniques used to characterize exhalation flows while breathing, sneezing, coughing, and speaking. Here, we have identified the most relevant articles and separated them, technical-wise, into two main categories as follows: global flow-field measurements and pointwise measurements. *Table 1* shows the corresponding articles and the main parameters measured. It is important to note that such parameters strongly depend on the adopted technique, and ultimately results are difficult to compare. In the following subsections, we provide an analysis of these applied techniques and discuss their pros and cons.

1.2.1 Global flow-field measurements

The global flow-field measurements techniques provide information regarding the flow properties over the whole flow field. The global flow-field techniques and the pointwise techniques are often complementary. Global flow field measurements provide a global information on the propagation of the exhaled jet and its interaction with the indoor air flow. As for the characterization of the exhaled flow, three global flow-field techniques are used in the literature: high-speed photography, schlieren photography, and Particle Image Velocimetry (PIV). The first two techniques which visualize the flow, provide information about the flow shape, its direction and its propagation. The propagation of

the flow in the surrounding environment is usually describe by two parameters, namely the propagation distance and the propagation velocity. The propagation distance is defined as the distance between the mouth/nose of the subject and the tip of the exhaled jet as shown *Figure 1*. The propagation velocity corresponds to the speed at which the jet tip travels.

Table 11 The main measured parameters of the experimental studies on the characterization of human exhaled airflow.

Measurement techniques		**Article**	**Main findings**				**No. of subjects**
			Measured parameters	**Breathing**	**Coughing**	**Sneezing**	**Speaking**	
Global flow-field	**High-speed visualization**	Bourouiba *et al.*[20]	Duration (ms)		300	200		1
			Re		10000	40000		
			Entrainment coef. (jet phase)		0.24±0.02	0.13±0.02		
			Entrainment coef. (puff phase)		0.132±0.06	0.055±0.01		
		Gupta *et al.*[9]	Nose opening area (cm²)	F*: 1.16 ± 0.67 M**: 1.20 ± 0.52				5
			Mouth opening area (cm²)	F: 0.56 ± 0.10 M: 0.71 ± 0.23			F: 1.80 ± 0.03 M: 1.80 ± 0.03	
		Gupta *et al.*[14]	Mouth opening area (cm²)		F: 3.37 ± 1.40 M: 4.00 ± 0.95			5
	Schlieren photography	Xu *et al.*[16]	Propagation velocity (m.s^{-1})	mouth : M: 0.2-0.6 F: 0.3-0.8				
		Tang *et al.* [23]	Propagation distance (m)	Nose: 0.60 Mouth: 0.80	0.7	0.6		20
			Propagation velocity (m.s^{-1})	Nose: 1.40 Mouth 1.30	5	4.5		
			Propagation area (m^2)	Nose: 0.11 Mouth: 0.18	0.2	0.2		
			Area expansion rate (m^2.s^{-1})	Nose only: 0.16 Mouth only: 0.17	1.5	2		
		Tang *et al.*[12]	Propagation distance (m)		F: 0.16-0.55 M: 0.31-0.64			20
			Propagation velocity (m.s^{-1})		F: 2.20-5.00 M: 3.20-14.00			
			Propagation area (m^2)		F: 0.01-0.11 M: 0.04-0.14			
			Area expansion rate (m^2.s^{-1})		F: 0.15-0.55 M: 0.25-1.40			

Schlieren PIV' velocimetry	Tang *et al.*[12]	Maximum air speed ($m.s^{-1}$)		8.00		16
	Savory *et al.*[28]	Average of the spatially averaged maximum velocity after 1 m from mouth ($m.s^{-1}$)		0.41		12
	Kwon *et al.*[19]	Average initial velocity ($m.s^{-1}$)		M: 15.30 F: 10.60	M: 4.07 F: 2.31	26
Particle image velocimetry	VanSciver *et al.*[25]	Maximum velocity range ($m.s^{-1}$)		1.15-28.8		29
		Average max. velocity ($m.s^{-1}$)		10.2±6.7		
		location of max. velocity (mm)		67.8±78		
		Median velocity ($m.s^{-1}$)		8.1		
		Jet width at 50 mm from mouth (mm)		35.8±27.9		
	Chao *et al* [27]	Maximum air velocity ($m.s^{-1}$)		M: 13.2 F: 10.2	M: 4.6 F: 3.6	11
		Average initial air velocity ($m.s^{-1}$)		10.2	3.9	
	Zhu *et al.*[26]	Initial velocity ($m.s^{-1}$)		11.2		3
Pointwise measurement	Xu *et al.* [16]	Thermal plume ($m.s^{-1}$)	0.23			18
		Velocity at 3mm from nose in standing position ($m.s^{-1}$)	F: 1.63 M: 1.08			
		Velocity at 3mm from nose in Lying position ($m.s^{-1}$)	F: 1.52 M: 1.82			
		Centerline velocity ($m.s^{-1}$)	decay of centerline see equation 1			
		Exhaled air temperature (°C)	36-32			
	Xu *et al* [35]	Relative Humidity	80%			22
		Mean peak velocity at 3mm from mouth ($m.s^{-1}$)	F: 1.03 ± 0.51 M: 0.81 ± 0.4			
		propagation distance (m)	0.3			
		Turbulence intensity at 3mm from mouth	41 ± 5%			
	Gupta *et al.* [9]	Change of air flowrate over time ($L.s^{-1}$)	sine function		1.6	25
	Gupta *et al.* [14]	Change of air flowrate over time ($L.s^{-1}$)		combination of gamma-probability-distribution functions		25

1.2.1.1 High Speed Photography

The high-speed photography is used for flow visualization and provides information regarding the flow shape and its propagation such as the flow direction, spread angle and propagation velocity. To visualize the airflow, a high-speed camera is used to capture the motion of tracer particles like cigarette smoke or theatrical fog. The used tracer particles are fine enough to closely follow the airflow.

This technique was applied by Gupta *et al.* to identify the boundary conditions of the airflow exhaled during coughing [14] breathing and speaking [15] . In this study, cigarette smoke was used as a tracer assuming that the 0.2 µm smoke particles closely follow the airflow [14] . In order to visualize the airflow, five smoking subjects were photographed using a black background and a light source beneath the subject's face. This technique provides images with visible smoke particle concentration gradient which allows a rough estimation of both airflow direction and spread angle. As shown in Figure 1, the flow direction is defined as the angle between the flow center and the horizontal. Such angles can be determined by analyzing the side view photography. Table 2 compares the angle values obtained by Gupta [14,9] with other studies from literature [16,17,18,19].

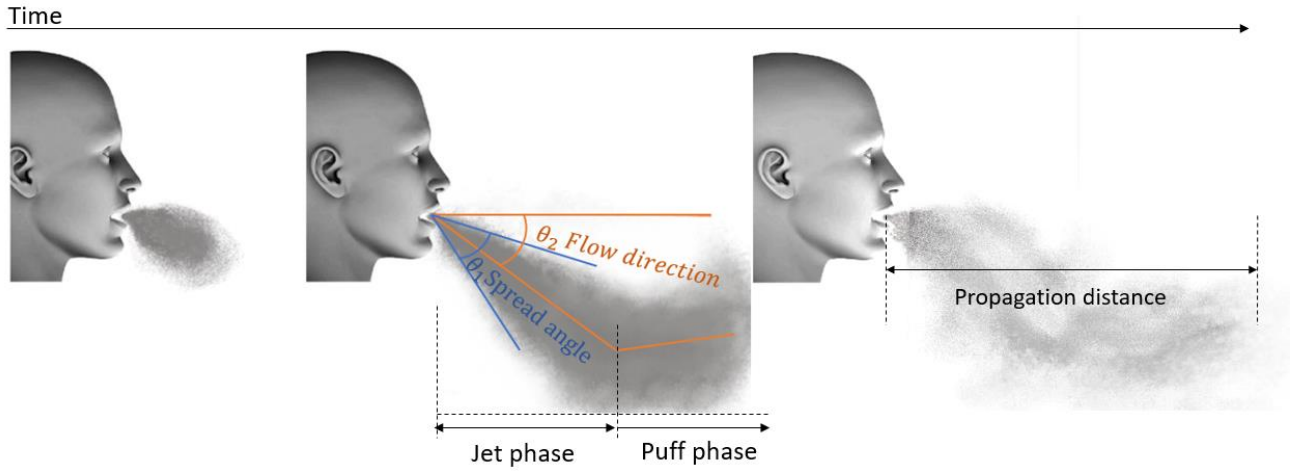

Figure 1 The flow direction and flow spread angle

Likewise, front view photography of the subjects was used to determine the mouth and nose opening areas. The latter information is important to provide boundary condition for flow modeling. Gupta et al. photographed the subject's nose and mouth during coughing [14] speaking [9] and breathing [9]. The values of these areas are shown in *Table 2*. Though a noticeable difference in nose and mouth opening area has been found between subjects.

Bourouiba *et al.* [20] used the high-speed imaging technique to analyze sneezing and coughing. The authors used exhaled droplets of small diameters as a tracer. Whenever the concentration of droplets was too low, the visualizations was enhanced with a smoke generator. The visualizations showed that the cough lasts 300 ms while the sneeze duration is shorter (200 ms). Both coughing and sneezing exhaled jets were considered as turbulent since the Reynolds number for coughing and sneezing were 10 000 and 40 000 respectively. Bourouiba *et al.* analyzed the flow shape in the first 70 cm from the mouth and they noticed a change in the flow direction at the middle of this distance. As illustrated in *Figure 1*, the first part of the flow near the mouth (prior to the change of flow direction) was referred as the jet phase by Bourouiba *et al.*, while, the subsequent phase was referred as the puff phase. The authors defined the entrainment coefficient α as the slope of the linear relation between the jet radius and the travel distance from the mouth. With this definition, the relation between α and the spread angle θ_1 is $\alpha = \tan(\theta_1/2)$. As for coughing, Bourouiba *et al.* reported an entrainment coefficient of 0.24 in the jet phase which corresponds to a spread angle of 27°. This value matches well with those obtained by Tang *et al.* [12] and Gupta *et al.* [14] as shown in Table 2 . Thanks to the high-speed photography technique, the authors identified the value of the puff phase entrainment coefficient, which is almost half of the jet phase one, corresponding to a spread angle of 15°. Likewise, a similar decomposition of the flow into a jet phase and a puff phase was also made for the sneezing activity. The entrainment coefficients values were 0.13 and 0.055 for the jet and puff phases respectively, which corresponds to spread angles of 14.8° and 6.3°.

Table 2: The direction and the spread angle of the exhalation jet from the literature

Exhalation mode	Source	Flow direction		Spread angle	
		mouth	nose	mouth	nose
Breathing	Xu et al. [16]	14◦± 14◦	57◦± 6◦	36◦± 6◦	32◦± 3◦
	Tang et al. [11]	Horizontal	45◦− 30◦	-	-
	Gupta et al. [9]	Horizontal	60◦± 6◦	30◦	23◦± 14◦
Coughing	Bourouiba et al. [20]	-	-	27°	-
	Kwon et al.	-	-	36◦	-
	Tang et al. [12]	-	-	23.9◦± 3.4◦	-
	Gupta et al. [14]	27.5◦± 5.9◦	-	25◦± 6.4◦	-
Speaking	Kwon et al. [19]	-	-	59◦	-
	Gupta et al. [9]	-	-	30◦	-
Sneezing	Bourouiba et al. [20]	-	-	14.8°	-

The high-speed photography technique was not only applied on human subjects. Liu and Novoselac [21] built a cough box or cough generator with a volume of 15.6 L. Air was injected inside this box with a square wave temporal profile, and with a time step of 1s. The airflow was visualized by using a fog machine that generates particles with diameters lower than 2.5 µm in size. The analysis of the flow shape revealed that the jet propagates more than 0.2 m in 0.1s. The observation of the flow boundaries allowed the determination of the spread rate, which is defined as the ratio between the radial expansion of the jet and the horizontal propagation. The captured images showed the creation of a circular vortex, also known as the leading tip, in the front of the jet during the first 0.15 s.

1.2.1.2 The schlieren photography

The schlieren photography technique is based on the variation of the air refractive index with the density. In the case of human exhalation flows, a density gradient is induced by the temperature difference between the ambient air and the exhaled air. Although the exhaled air temperature varies with the climatic conditions, it is usually higher than the ambient air. In laboratory conditions with 50% relative humidity and 20°C, the air is exhaled from the nose at a temperature value close to 34°C [22]. The schlieren technique can be used to study the flow shape and analyze its propagation in the surrounding environment. Tang *et al.* implemented this technique to observe the breathing [11], sneezing [11] and coughing [23] of 20 healthy volunteers (10 females and 10 males). They used a high-speed camera to capture images of exhalation that were later automatically processed. The automation of the image processing allowed the authors to analyze a large number of images and to extract data about the visible projected area and the propagation distance at a high frequency. Tang *et al.* [23] reported that the average horizontal propagation distance of coughing was in the range of 0.16 m to 0.64 m however, when they reprocessed the images in another study [11] considering the propagation on the main flow direction they found that the maximum distance is 0.7 m and the maximum derived velocity is 5 $m.s^{-1}$. Pepper sneeze stimulus was used to help six volunteers to sneeze and the sneeze puff traveled 0.6m with a propagation velocity of 4.5 $m.s^{-1}$ [11]. By analyzing the schlieren imaging for nasal and mouth breathing, they found that the air travels 0.6m with a velocity of 1.4 $m.s^{-1}$ in the case of nasal breathing, while it propagates more slowly at a velocity of 1.3 $m.s^{-1}$ over longer distance -0.8m- in the case of mouth breathing [11]. When analyzing these data, it is important to keep in mind that these distances are characterized by the temperature/density gradient and not the local airflow velocity. Further results of the breathing flow shape and direction obtained by [11] are presented in Table 2.

Another study by Xu *et al.*[16] used schlieren photography technique to visualize the breathing airflow in standing and lying positions of 18 healthy subjects at 23°C room temperature. They noticed that

the flow shape, direction and propagation seem to vary from one person to another. However, they were able to determine average values of the jet direction and spread angle for mouth only and nose only breathing which are reported in Table 2. Images recorded by the high-speed camera demonstrated that the ring vortices flow structures at the jet boundary of built by successive breathing cycles are connected, having similar characteristics to these observed in a steady turbulent jet. In addition to this qualitative result, the schlieren analysis allows to investigate the interaction between the body thermal plumes and the exhalation flow. With this technique, two main effects of this interaction were noticed: in the standing position the raising body thermal plume interacts with the exhaled air drifting it upwards while for the laying position the direction of the thermal plume is the same as the exhaled flow therefore enhancing the upward air movement.

1.2.1.3 Particle Image Velocimetry

The Particle Image Velocimetry (PIV) technique has been widely used in the field of indoor air because it provides essential detailed quantitative information on the flow fields[24]. In this PIV technique, a pulsed laser light sheet illuminates the tracer particles in a measurement plane, and a synchronized CCD camera acquires two single exposed images taken shortly after one another. By comparing these two pictures, the traveled distance of individual particles can be determined, and it corresponds to the displacement field of tracer particles. The velocity field is then calculated by dividing the displacement field by the time step of a few microseconds order. The PIV has been used to characterize the airflow field formed by coughing [25,19, 26, 27] and speaking[19,27]. In these studies, the subjects were asked to cough into a chamber which was filled with submicronic particles of titanium dioxide[28], olive oil [19], saline fog[27], or glycols solutions[25]. The motion of the tracer particles is recorded a few microseconds after the beginning of the exhalation event[29] with a typical time step of 100 µs. Thus, the PIV can provide a quantitative measurement of the velocity flow field for highly unsteady flows like coughing and speaking. However, there are two main limitations for this technique. First, the health hazards arise from using the tracer particles and the laser when conducting the experiments on human subjects impose technical constrains. Second, the exploration area is limited, a typical optical configuration of the PIV as in Savory *et al.*[28] forms a measurement area of 400 cm^2.

VanSciver *et al.*[25] asked 10 males and 19 females to cough into a 120 cm × 76 cm × 67 cm chamber to analyze the airflow field and the maximum coughing velocity. They recorded a wide range for this maximum velocity; from 1.15 $m.s^{-1}$ to 28.8 $m.s^{-1}$ while the average maximum velocity was 10.2 $m.s^{-1}$. The authors found that the maximum velocity of the airflow usually happens at a distance of 3.9 mm to 309 mm from the mouth because of the vena contracta phenomenon. The vena contracta phenomenon happens with the sudden change of the cross-sectional area of the flow geometrical boundaries. As the exhaled flow direction cannot be quickly adjusted to the sudden increase of the

flow area after the mouth, it continues to contract, and the minimum flow area corresponding to the maximum air speed occurs after the mouth as illustrated in *Figure 2*.

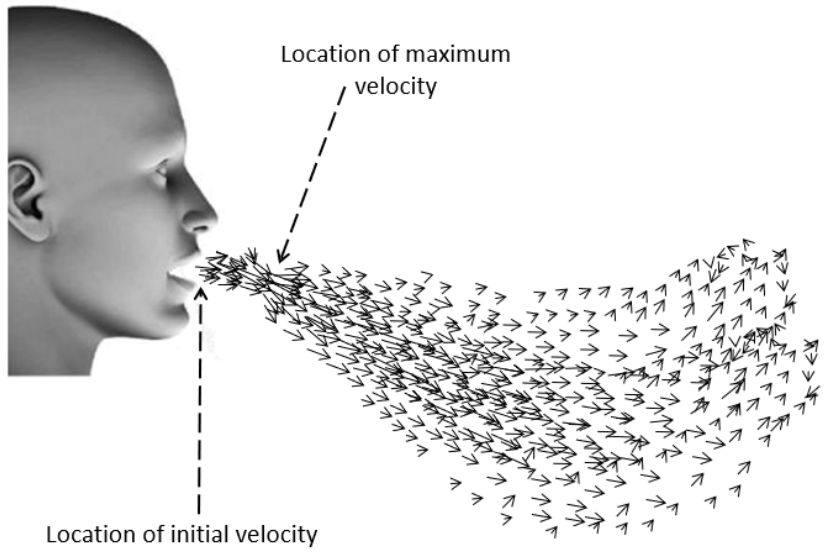

Figure 2: Schematic figure for the velocity flow field during exhalation

This maximum velocity is reached 20 µs after the beginning of the cough. Then it decreases by 74 % after 0.67 s. Through the postprocessing of the velocity field obtained by PIV technique, it is possible to build velocity profiles at different locations in the jet to analyze its expansion. VanSciver *et al.* defined the width of the jet by considering the upper and lower locations where the velocity is half of the maximum profile velocity. They reported a linear jet expansion over the first 200 mm from the mouth. The Reynolds number for coughing exhaled jet was in the range of 2,300 to 57,600 and the average Reynolds number was 20,400, which is in accordance with the value of 10 000 obtained by [20] for a single subject.

Considering these values of the velocity and the size of the box the authors suspected that the results could be affected by the confinement effect due to the small size of the box (1.2 m in length). However, in another study [26], three subjects coughed in a chamber of 180 cm × 180 cm × 180 cm and the average maximum velocity was 11.2 $m.s^{-1}$, only 10% higher than the value reported by VanSciver *et al.* This slight difference could be attributed to the individual differences between subjects and it does not confirm the effect of the confinement. In the study of Zhu *et al.* [26] the range of the maximum velocity was between 6 $m.s^{-1}$ and 22 $m.s^{-1}$. However, values greater than 18 $m.s^{-1}$ were very rarely observed. Savory *et al.*[28] used PIV to investigate the velocity at 1-meter distance from the mouth for 12 healthy individuals. They assumed that studying the far field velocity would be of particular

interest for disease transmission studies. This study reveals that at 1-meter distance the cough affects the air velocity field and the measured average velocity value is 0.41 $m.s^{-1}$.

Kwon *et al.*[19] and Chao *et al.*[27] used the PIV technique to analyze the velocity field near the mouth produced by coughing and speaking. They defined the *initial velocity* as the highest velocity measured during the coughing process. The initial velocity distribution diagram built from measurements with a 26 volunteers group by Kwon *et al.* showed that this initial velocity of the cough lies within a 6 to 13 $m.s^{-1}$ range, with an average initial coughing velocity of 15.3 $m.s^{-1}$ for males and 10.6 $m.s^{-1}$ for females. The results of Chao *et al.* were in accordance with the other studies discussed in this section: the authors reported an average coughing velocity of 11.7 $m.s^{-1}$. Although it is challenging to characterize air flows produced during speaking activity (because of its dependence on the pronounced sounds), Kwon *et al.* and Chao *et al.* obtained comparable results. The protocol for Kwon *et al.* experiment consisted in counting from one to three in Korean while it was counting from 1 to 100 ten times in Chao *et al.* study. The average maximum measured speaking velocity by Kwon *et al.* was 4.07 $m.s^{-1}$ for males and 2.31 $m.s^{-1}$ for females, and for Chao *et al.* it was 3.9 $m.s^{-1}$. Chao *et al.* also mentioned that the propagation distance for coughing was higher than for speaking and that the entrainment of the ambient air was noticeable in both cases. Further vector analysis was conducted by Kwon *et al.* to identify the jet spread angles and the values obtained are compared with the other values in the literature [14, 9, 12] in Table 2.

As discussed above, health hazards arise when using the PIV technique on human subjects, it requires to apply safety procedures, in particular those to make sure that the tracer particles are confined in the measurement chamber. This makes the study of the airflow near the subject's body difficult. Moreover, it eliminates the effect of the body thermal plume on the exhaled airflow. To overcome these constrains, researchers developed thermal breathing manikins to simulate the human exhalation activities and enhance the study of the airflow in the human microenvironment. Feng *et al.*[30] used a thermal breathing manikin together with a two-dimensional time-resolved particle image velocimetry system, to obtain detailed data on averaged flow fields, vorticity and turbulence intensity, for further comparison with CFD simulations. The manikin was breathing in horizontal direction through a mouth opening of 12 mm diameter. The airflow rate was 0.45 L per exhalation following a sinusoidal pattern with a frequency of 15 breaths per minute. In order to study the thermal plume, the exhaled air temperature was kept in the range of 32 °C - 36 °C, and the body of the manikin was heated using a 75 W heater. Feng *et al.* applied the phase-averaged method to analyze the results of the PIV. They divided the breathing process into 40 phases, 20 for exhalation and 20 for inhalation, and the velocity values were averaged over each phase. This study showed that during the middle phases, the flow shape and the linear spread of the airflow were similar to those of the free jet. The use of the PIV permitted to identify the formation of two large vortices on the two sides of the jet in the initial stage.

These vortices evolve and are more noticeable during the middle phases when higher turbulence intensity is measured. The use of the thermal breathing manikin and the phase average approach produced statistically acceptable data to study the flow turbulence. The maximum turbulence intensities were measured near the centerline of the flow where the exhaled flow interacts with the thermal plume that drifts the jet flow upward.

With the same manikin as Feng *et al.*, Jiang *et al.*[31] studied the characteristics of the exhaled air parameters during breathing. The effect of the thermal plume was analyzed by building the contour map for the normal velocity. Jiang *et al.* used the proper orthogonal decomposing to divide the flow into four different parts: main-flow part, coherent part, transient, and turbulent part. The main flow contains most of the flow energy and the fluctuations are divided between the other three parts. The authors noticed that during the late phases of exhalation the thermal plume contributed in enlarging the coherent part of the flow which means that the thermal plume enhances the flow turbulence.

Another study by Berlanga *et al.*[32] used PIV and the phase average approach to study and analyze the velocity field of the human exhalation of an average male (test M) and an average female (test F), using a life-sized thermal manikin. They used CO_2 as a tracer and with the help of a high-resolution camera they studied the flow direction and propagation. The manikin was in lying position and so the flow had a vertical direction and the exhalation had sinusoidal pattern with a flow rate of 9.45 $L.min^{-1}$ for (test M) and 7.52 $L.min^{-1}$ (test F). The comparison of results for the (test M) and (test F) showed that although the flow shape is almost the same, the propagation distance for the (test M) was higher than (test F) and the diffusion angle was wider, 20.5° for (test M) and 22.7° for (test F).

1.2.2 Pointwise measurements

Here, pointwise measurements refers to quantitative measurements performed by using probes at a given point in the flow field. This includes measurements for velocity, temperature, humidity, and air flowrate. The pointwise measurements provide accurate quantitative information. However, those measurements require a lot of time and effort to obtain a full picture of the flow. To overcome this difficulty, the pointwise measurements techniques are often preceded by one kind of global flow-field techniques.

As shown on *Table 1*, coughing is by far the most studied exhalation mode because of its important impact on disease transmission. Preliminary studies[33,34] aimed to examine the coughing flow rate, which is usually characterized by three following parameters; Cough Peak Flow Rate (CPFR), Cough Expired Volume (CEV) which is the total volume expired during the cough, and Peak Velocity Time (PVT) which is the time between the beginning of the cough and the time at which the maximum velocity occur. Using regression analysis, relationships between these parameters and the height,

weight, gender and age of the person were proposed by Mahajan *et al.*[33] and Singh *et al.*[34]. Gupta *et al.* [14] measured the airflow rate of 25 healthy subjects for coughing, breathing and speaking using a spirometer. They found that the cough airflow rate can be described using a combination of gamma probability distribution functions while the normal breathing airflow rate follows a sine function over time and this function depends on the subject height and weight [9]. The value obtained for the duration of a single cough was in the range of 0.26-0.78 s, which is in accordance with the value obtained by means of high-speed photography of 0.3 s by Bourouiba *et al.* [20]. The airflow rate during speaking might be the most difficult to measure as it depends on the pronounced sounds. To characterize the airflow rate for speaking, Gupta *et al.* [9] used a spirometer to measure the exhaled airflow during three exercises: counting from 1 to ten, pronouncing six letters and reading a passage. Pronouncing T letter resulted in 2 $L.s^{-1}$ flowrate and it was the highest expelled flowrate. Consequently, pronouncing number two and ten produced more airflow. The peak flow rate measured during passage reading was 1.6 $L.s^{-1}$.

In addition to the airflow measurements, Xu *et al.*[16] conducted velocity pointwise measurements for the breathing airflow. For optimized experimental planning, these measurements were preceded by schlieren photography in order to estimate the centerline of the airflow. Using a hot sphere anemometer, pointwise measurements for velocity were taken along the flow centerline at different distances from the mouth/nose. The average *initial breathing velocity* was measured at 0.03 m from nose. In the standing position, the measured initial velocity was respectively 1.08 $m.s^{-1}$ and 1.63 $m.s^{-1}$ for male and female. According to Xu *et al.* the decay of the centerline velocity could be expressed by the following power function:

$$U_m = ax^b \quad (1)$$

Where U_m is the centerline velocity and x is the distance from the mouth/nose. a and b are constants which depend on gender and mode of breathing (mouth or nose).

As discussed above, manikins can be used to overcome technical constrains but there are differences between human and manikin exhalation. To evaluate these differences, Xu *et al.*[35] compared the characteristics of breathing from a human subject and a thermal breathing manikin using hot sphere anemometer. The manikin had two 12mm-diameter circular openings (nose openings) and a semi-elliptical mouth of 120 mm^2. Sinusoidal breathing was modeled with a frequency of 15.5 breaths per min and a respiratory minute volume of 8.8 $L.min^{-1}$. This respiratory minute volume is the amount of air exhaled or inhaled during one minute. The measured temperature of the exhaled air was 34 °C while the room temperature was kept at 20 °C. Xu *et al.* noticed that the sinusoidal breathing of the manikin produces the same velocity profile as the human subject but with different respiratory frequency and magnitude. These differences result in a significant underestimation of the turbulence

levels as the turbulence intensity on the center line was (41 ± 5) % for the subject and 1.3% for the manikin. The velocity profile was obtained by measuring the velocity of the air in different vertical planes at given distances from the source. The airflow from the manikin was similar to the turbulent circular jet and the propagation distance was around 0.3 m for the subject and 0.4 m for the manikin. The authors compared those results with the results of the previous studies [11,23] obtained by applying the schlieren photography technique and they suggested that using the schlieren technique might overestimate the propagation distance of the flow. This overestimation might be attributed to temperature diffusion rather than the travel of the gas.

Another study by Xu *et al.*[36] also used pointwise measurements to investigate the effect of the ventilation and the metabolic rate on the dispersion of exhaled droplets. The metabolic rate corresponds to the amount of consumed energy by the body per unit of time. The metabolic equivalent of task (met) corresponds to a reference metabolic rate of 1.163 W/kg, which is roughly equivalent to the amount of energy expended at a sitting position. To study the effect of body activity, the thermal breathing had two metabolic rates, 1.2 met and 2 met. The measurements were conducted in a room with two ventilation methods, room mixing ventilation and displacement ventilation, to compare between them. Xu et al.36 reported that the velocity profiles of the sinusoidal exhaled airflow were similar to those of the steady jet. Based on results obtained by the high-speed photography technique, Liu and Novoselac 21 conducted quantitative measurements of the jet flow centerline velocity using a hot wire anemometer and a hot sphere anemometer at 76 positions. Table 3 summarizes the characteristics of the manikins used in the previous studies and measured parameter.

Table 3: The characteristics of the artificially produced jets and the measured parameters

Measurement technique	Article	Exhalation Mode	Manikin properties			Generated Jet				Main studied parameters
			Opening Area	Thermal Load	Body Thermal Temperature (°C)	Continuity or Frequency	Flowrate or Velocity	Flow Shape	Temperature °C	
Visualization										• Propagation distance • Spreading rate
	Liu and Novoselac [21]	Coughing	circular tube of 2.4 cm inner diameter	45 W		1 times.s^{-1}	*initial velocity= 6.08 m.s^{-1}	Square wave		Comparison between steady jet and cough jet in terms of • Centerline velocity • Velocity profile
Pointwise anemometry	Xu *et al.*[36]	Breathing	Mouth: 120 mm^2 (semi ellipsoid) Nose: 2 tubes, 12 mm diameter	70 W.m^2		15.5 times.min^{-1}	8.8 L.min^{-1}		34	Effect of body metabolic rate and ventilation on • velocity profile • Centerline velocity
	Xu *et* al.[35]	Breathing	Mouth: 120 mm^2 (semi ellipsoid) Nose: 2 tubes, 12 mm diameter	70 W.m^2		15.5 times.min^{-1}	8.8 L.min^{-1}		34	Comparison between human and manikin breathing in terms of: • velocity profile • Centerline velocity
PIV	Feng *et al.*[30]	Breathing	12 mm diameter circular	75 W	32-36	15 time.min^{-1}	0.45 L/exhalation time		34	• Velocity field • Flow shape • Vorticity • Centerline Velocity • Turbulence intensity

Berlanga *et al.*[32]	Breathing	Mouth:122 mm^2 (circular)	128 W	34	16.43 & 13.7 $times.min^{-1}$	9.46 $L.min^{-1}$ & 7.52 $L.min^{-1}$		34	• Velocity field • Flow shape • Jet spread angle • vorticity • Centerline Velocity
Jiang *et al.*[31]	Breathing	Nose: 12 mm diameter	75 W		15 $times.min^{-1}$	0.45 L/ time	sinusoidal	34	• Velocity field • Spatial distribution of the turbulence intensity • Effect of the body thermal plume.

1.3 Measurements on the exhaled droplets

As discussed in the introduction, the exhaled air jet carries droplets with a polydispersed size distribution. Studies on the characterization of the exhaled droplets mainly focus on determining the size of the initial droplets as it is the main parameter governing their fate; either they deposit on a surface or remain suspended and carried by the airflow[37] . The size of the droplets is also associated with their composition and the likelihood of bearing pathogens. A study by Milton et al.[38] examined particles exhaled from 37 seasonal-influenza infected patients. The study showed that fine particles -smaller than 5 µm- contain 8.8 fold more viral copies than coarse particles -bigger than 5µm-. Similarly, Lindsey et al.[39] found that 42% of influenza RNA is detected in particles smaller than 1 µm, while 23% is in particles of 1 to 4 µm, and 35% in coarse particles bigger than 4µm. Fabian et al.[40] conducted another observational study on 12 laboratory-confirmed influenza patients. In this study, they observed that during tidal breathing, 87% of the particles sampled from patients' exhalations were less than 1 µm. After detecting the presence of RNA in part of these fine particles, Fabian et al. concluded that submicronic aerosols could have an important contribution to the influenza transmission process. These different results can be linked to the relation between the droplet size and its origin in the respiratory tract. Morawska et al.[11] analyzed the modes of particles produced by different exhalation activities. They found that normal breathing produces particles of 0.85µm mode, the vocal cord vibration mode is 3 µm, and oral or saliva mode is 10 µm.

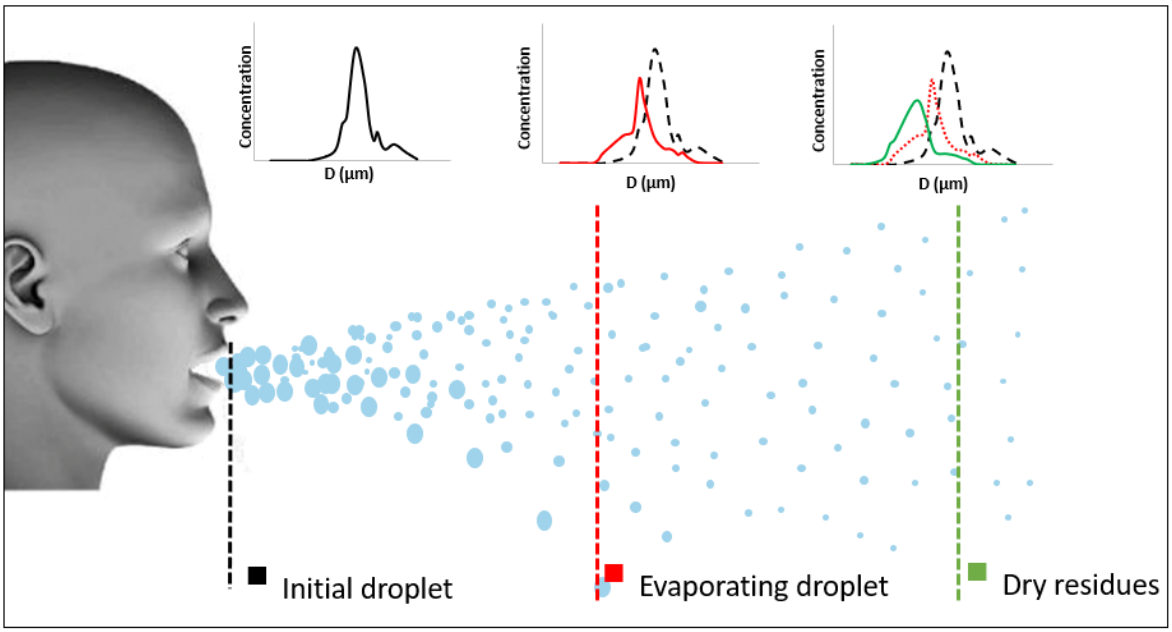

Figure 2: The change of exhaled droplets size distribution with distance.

After their release, the droplets go through a very rapid evaporation process and transform to dry residues which are mainly composed of NaCl and organic component[41]. Figure 2 illustrates both the change of the size distribution of the exhaled droplets at different distances from the mouth and the settling drift of large diameter droplets due to gravity. When choosing a measurement technique, it is critical to look at the place of the measured droplets with respect to this evaporation process. Some measurement techniques involve sampling and travel of the droplets from the sampling point to the measurement location. During this travel, evaporation might occur which induces a change in the measured droplet size. So, these techniques are well adapted to measure the size of dry residues after the complete evaporation of the droplets, but they can be also used to predict the initial droplet size distribution by applying some calibration process or evaporation model. In our review, all the techniques involving the extraction/collection of a sampled airflow with particles are named *intrusive* techniques. *Nonintrusive* measurements are directly conducted in the flow stream without sampling.

Gralton *et al.*[42] reviewed the measured size of the exhaled particles in literature, including both droplets and dry residues, and they concluded that the exhaled particles have a size range between 0.01µm and 500µm. This size range can hardly be covered by a single measurement technique, which justifies the use of two kinds of techniques in most of the reviewed studies. Table 4 classifies the studies aimed at characterizing the respiratory droplets according to the adopted measurements technique. The term *equivalent diameter* which appears in Table 4 is an important point when considering any aerosol size measurement technique. As each measurement technique is based on a specific physical property, the equivalent diameter is "*the diameter of a sphere having the same value of a specific physical property*"[43]. For example, the Aerodynamic Particle Sizer (APS) measures the particle aerodynamic equivalent diameter which is defined as the diameter of a sphere having a density of 1000 $kg.m^{-3}$ and the same gravitational settling velocity as the measured particle. The optical diameter corresponds to the diameter of the spherical particle scattering the same light amount as the analyzed particle. Baron et al.[43] define the mobility equivalent diameter as "*the diameter of a sphere with the same mobility as the particle in question*". Meanwhile, the geometric diameter is the diameter of the spherical particle which is usually obtained through direct measurement of the particle using a microscope or through a geometric analysis of the particle's image. Thus, the equivalent diameter should be considered when applying different measurement techniques or comparing their results.

Table 4: The techniques used for the characterization of the respiratory droplets

	Technique	Measured parameters	Size range	Equivalent diameter	Articles
Intrusive	Solid impaction	▪ Size distribution of dry residues and initial droplet ▪ concentration of pathogens in the exhaled air	-	Aerodynamic diameter	Duguid[44], Milton et al.[38], Fennelly et al.[45]
	Droplet deposition analysis	▪ Size distribution of initial droplet ▪ Concentration of initial droplet	-	Geometric diameter	Duguid[44], Loudon and Roberts[46], Li et al. [47], Xie et al.[48] Morawska et al.[58]
	Optical particle counter	▪ Size distribution of dry residues and initial droplet ▪ Concentration	0.3 µm –20 µm	Optical diameter	Fabian et al.[40] Fabian et al.[50] Edwards et al.[51], Holmgren[51], Almstrand et al.[53], Papineni and Rosenthal[54] Li et al.[47] Xie et al.[48], Wurie et. al[55], Wurie et. al.[56]
	Aerodynamic particle sizer	▪ Size distribution of dry residues or evaporating droplets ▪ concentration	0.5 µm -20 µm	Aerodynamic diameter	Yang et al.[64] Morawska et al.[58] Liu Novoselac [21] Fang et al.[59] and Asadi et al.[60]
	The electrical low-pressure impactor	▪ Size distribution of dry residues	0.007µm to 10 µm	Aerodynamic diameter	Hersen et al.[63]
	The Scanning Mobility Particle Sizer	▪ Size distribution of dry residues ▪ concentration	0.02 µm to 0.6 µm	Mobility diameter	Yang et al.[64]

	Filter collection	▪ Size distribution of dry residues ▪		Geometric diameter	Loudon and Roberts[46]
Nonintrusive	High-speed photography	▪ Particle dynamics and propagation ▪	It depends on the laser and optical configuration of the system	-	Zhu et al.[26], Nishimura et al.[65], Bourouiba et al. [20]
	Laser particle size analyzer	▪ Size of evaporating droplet ▪ concentration	0.1 µm -1000 µm	Optical diameter	Han et al.[68], Zayas et al.[69]
	Interferometric Mie Imaging	▪ Size distribution of droplet ▪ Concentration	>2 µm	Optical diameter	Chao et al.[27], Chao and Wan[67]

1.3.1 Intrusive measurement techniques

Solid impaction, droplet deposition, optical particle counter and aerodynamic particle sizer are widely used intrusive measurements techniques. Solid impaction and droplet deposition were the techniques applied by the early studies and then optical particle counter and aerodynamic particle sizer were later used. Other techniques like Liquid impingers, Scanning Mobility Particle Sizer (SMPS), Electrical Low-Pressure Impactor (ELPI) and Condensation Particle Counter (CPC) are less cited in the existing literature and they are also discussed in the last subsection.

1.3.1.1 Solid impaction

Early studies used solid impaction technique to quantify the size distribution of the droplets expelled during coughing, sneezing, breathing and speaking. In addition to the size information, collected droplets can be used for further biological tests. Duguid[44] studied the size distribution of the initial droplets produced during speaking, sneezing and coughing using impaction plates placed in front of the subjects' mouth, at respectively 3 and 6 inches in the cases of speaking and coughing/sneezing. For a better visualization of the droplets, Duguid applied dye on the surfaces of the mouth and fauces. To calculate the diameter of the initial droplets, a calibration procedure was applied to find the relationship between the size of the stain marks remained on the celluloid-surface of the impaction plate and diameter of the initial droplets. The size of the initial droplets was in the range of 5 µm to 2000 µm, and it is assumed that droplets with a diameter lower than 5 µm might evaporate quickly or be driven by the deflected flow around the impaction plate. Duguid also used another solid impaction device which is the slit sampler also known as slit impactor to collect the suspended dry residues from the air on a rotating agar plate. On this plate, pathogens contained in the dry residues multiply in the agar culture medium and form visible colonies that can be counted. By measuring the air volume extracted during sampling, Duguid determined the number concentration of the viable dry residues. The slit impactor was also used by Milton *et al.*[38] to collect and analyze the influenza virus carried by droplets in the breath of infected individuals. They designed a conical hood into which the subject breathes to gather the exhaled air. Then, the captured air passes through a conventional 5µm cut-off diameter slit sampler to collect large droplets. A water vapor condensation process on the fine particles, less than 5µm, was then used to grow the size of these particles so that they could be collected with a 1 µm cut-off diameter slit sampler. This procedure permits the biological analysis of the fine fraction of exhaled droplets. A six stages Andersen cascade impactor which is another solid impaction device was used by Fennelly *et al.*[45] to study the concentration and size distribution of infectious aerosols exhaled by patients with tuberculosis. The Andersen impactor used by Fennelly and the slit impactor provide information about the number concentration of the viable pathogens but not the size of the droplets or the dry residues. Although, the particles are classified into six size classes in the case of the Andersen impactor, the obtained size distribution cannot

directly represent neither the size distribution of the initial droplets nor the dry residues because the evaporation process between the collection point close to the patient mouth and the impactor is not evaluated.

1.3.1.2 Droplet deposition analysis

Droplet Deposition Analysis (DDA) is one of the techniques that has been used to determine the size distribution of the initial exhaled droplets. It requires building a correlation between the diameter of a droplet deposited on a surface forming a stain mark and the initial diameter of the droplet. Two types of droplets deposition experimental set ups have been developed. The first set up was designed by Loudon and Roberts[46], it consists in a closed box with about 57 L capacity and the walls were covered by high grade white boned papers. One of the wall sides contains an inlet opening through which the subject exhales breaths into the box. In the experiment, the mouth of each subject was colored with a dye. After a given number of exhalations, the size and number of the stain marks on the floor, opposite, right and left side of the box produced by the droplets' deposition were determined by microscopic observation. Li *et al.*[47] designed a box with the same characteristics of the one of Loudon and Roberts. Water sensitive paper was used instead of the white boned paper. This paper type has a yellow coating that turns into blue color with water contact. This particular property of the paper makes it possible to analyze the droplet size and number without using dye. Xie *et al.*[48] used the box designed by Li *et al.* to measure the droplets size distribution produced during coughing and speaking. They evaluated the impact of using the dye on the measured droplet size distributions. The water sensitive paper used in Li *et al.* experiment were replaced by glass slides in this experiment. The subjects exhaled in the box with and without using the dye and the size distribution of the droplets deposited on the glass slides was measured using a microscope. They concluded that the use of dye increases the production of droplets during human exhalation activities.

The second type of experimental set-up is the one designed by Morawska *et al.* [11], which consists in a wind tunnel where the head of the subject can be inserted. The air circulating inside the tunnel is filtered with a High Efficiency Particulate Air (HEPA) filter which ensures that the only source of particles inside the tunnel is the subject itself. Glass slides were placed in several locations downstream of the subject head, on the floor of the tunnel, to collect deposited particles. Using the same experimental set up, Johnson *et al.*[49] studied the modes of exhaled droplets size distribution with the objective of linking these modes to their sites of origin in the respiratory tract. The droplet of diameter less than 20 µm were most likely remain airborne, so 20 µm was consider as the lower detection limit of this system. The exhaled airflow rate was also estimated to obtain the droplet number concentration.

1.3.1.3 Optical Particle Counter

Optical Particle Counters (OPC) provide a determination of the optical equivalent diameter of the particle as a function of the light scattered by the particle when it crosses a light beam emitted by a white light or laser source. The air is extracted from the breathing zone of the subject through a mouthpiece which is a collection device that delivers the exhaled breath from the mouth of the subject to the inlet of the OPC. The OPCs are used to measure size and number concentration of the particles in the size range 0.3 µm –20 µm divided into 4[40,50], 6[51], or 15 size intervals[52]. One of the advantages of this extractive technique is that it permits conducting parallel measurements using other techniques such as impactors[53] or filters[50].

Papineni and Rosenthal[54] compared Droplet Deposition Analysis (DDA) to Optical Particle Counter (OPC) direct measurements. They reported that the OPC is more practical and less time consuming when compared to the tedious process of measuring and counting the droplet by the microscope for DDA. However, they estimated 23 milliseconds traveling time of the particles from the sampling point to the measurement point. To evaluate the impact of this transfer on the droplet diameter, Papineni and Rosenthal carried out two experiments to evaluate the condensation and the evaporation. The experiments demonstrated that there is no formation of new droplets inside the OPC due to condensation, and that evaporation was not observed. A predominance of the particles of less than 1 µm in diameter was noticed in the measurements obtained by the OPC while the particle concentration was more heavily weighted towards larger particles in the case of the DDA, even though dry residues were measured. The authors attributed this discrepancy to the instrumentation deficiencies in both techniques. On one hand, the low concentration of the small particles detected by the DDA system could be due to the large cutpoint caused by the small collection surface of the impactor used, or the limited resolution of the microscope. On the other hand, large droplets might be undetected by the OPC systems due to the sampling losses in the mouthpiece and the delivery lines. In another study[40], the exhaled breath of 10 influenza infected patients was analyzed using OPC. The size and number concentration were measured, and the results were similar to those of Papineni and Rosenthal, as 87% of the detected particles have a diameter less than 1 µm. The number concentration of the droplets in the size range of 0.3 µm - 0.5 µm was 61-3848 Particle.L^{-1} and for the size range of 0.5µm - 1µm was 5-2756 Particle.L^{-1}. The predominance of the submicronic particles for both healthy and rhinovirus (HRV)-infected subjects was noticed in a third study[50].

Wurie et al.[55] used the OPC to characterize the size distribution and concentration of droplets produced during tidal mouth breathing. The human droplet emissions were directly conveyed to the OPC using a disposable mouthpiece, while a nose clip was used to prevent nasal breathing. One-way valve and High Efficiency Particulate Air (HEPA) filter were used to insure no ambient or exhaled particles were re-inhaled. The same experimental set up was used by Wurie et al.[56] to characterize the emission of exhaled droplets from 188 tuberculosis infected patients. With this large number of subjects and by using the OPC technique, Wurie et al. were able to show that

intrathoracic tuberculosis infected patients produce significantly more bioaerosol than healthy subjects, in a particle size range that could transport Mycobacterium tuberculosis.

1.3.1.4 Aerodynamic Particle Sizer

The Aerodynamic Particle Sizer (APS) evaluates the particle droplet aerodynamic diameter through the measure of the time of flight of a particle being accelerated in a jet flow. The time of flight is "*the time between two pulses of light scattered by the particle as it passes through two beams of light"*[43] and depends on the capacity of the particle to accelerate, which permits to estimate the aerodynamic diameter of the particle. The typical size range of the APSs (TSI) used for the characterization of the particles is 0.5 µm - 20 µm. The total air flowrate pumped through the APS is 5 $L.min^{-1}$ divided into 1 $L.min^{-1}$ of sampling airflow and 4 $L.min^{-1}$ of sheath flow[57]. The sheath flow is filtered and then rejoin the sampling flow rate. The total flow then passes through an accelerating nozzle, which induce a pressure loss and temperature drop of the gas surrounding the particle surface. The accelerated particle is thus submitted to a temperature difference with a high convective heat transfer coefficient, which usually produces evaporation of volatile particles. Therefore, the APS is considered as suitable for the analysis of solid particles and nonvolatile droplets[57].Morawska *et al.*[11] designed a bench for the characterization of the exhaled droplets as discussed in section 3.1.2 together with the droplets deposition analysis system, an APS was used for the droplets in the size range 0.5 µm -20 µm. The authors measured the diameter of the droplets at three different distances from the subject: 0 mm, 100mm, and 300 mm. They found that the count median diameter inversely proportional to the distance from the subject, because of the equilibrium diameter changes with humidity. The same bench was used for another experimental study[58] where both size distribution and humidity were measured at the above-mentioned distances. They were able to distinguish different size distribution modes; droplets below 0.8 µm were produced during all the exhalation activities at an average concentration of 0.75 $part.cm^{-3}$, a second mode at 1.8 µm was also observed for all the activities at a concentration of 0.14 $part.cm^{-3}$ [58]. Speaking produces two more modes, 3.5 µm and 5 µm with a concentration of 0.04 $part.cm^{-3}$ and 0.16 $part.cm^{-3}$, respectively. They investigated the droplets evaporation through measuring the size distribution of droplets at different ages. As it was not technically possible to follow a single particle and measure the change of diameter due to evaporation, they assumed that measuring the droplet size distribution at different distances would be equivalent to measuring the size distribution of droplet at different ages. They used an APS at two different distances from the subject. The drying time for the droplets in the detectable size range of the APS was comparable to the drying time of pure water droplets, they evaporate in 0.8 s at 97% relative humidity, which made it technically difficult to detect the non-equilibrium evaporation.

Using an alternative technique, Yang et al. measured the size distribution of the initial droplets using an APS. The exhaled breath was collected in a sample bag and to avoid droplet evaporation, the humidity inside the sample bag was maintained at 95%. They found that the average size

distribution of cough droplets was in the range of 0.62µm to 15.9µm. The APS has fine size intervals and a high sampling frequency [21,43], which make it suitable for quantifying particles dispersion. Fang et al.[59] used the APS to examine the decay of the size and concentration of the droplets along the main dispersion axis, and they found that this decay is exponential. Liu and Novoselac, [21] also used the APS to measures the dry residues concentration in the breathing zone of a receiver manikin. A recent study by Asadi et al.[60] used the APS to analyze the effect of the voice loudness and the spoken language on the amount and size distribution of droplets emitted during speaking. The subjects were seated inside a hood with laminar ventilation and a fennel was placed near the subject face to collect the emitted droplets. A distance between the subject face and the fennel was kept allowing a free flow of air into the fennel. In this study, the estimated evaporation time of the droplets was much less than the travelling time between the subject mouth and the measurement point in the APS. In this experiment, the subjects spoke the four world most spoken languages, and the APS was used to compare the concentration of sampled air. The authors found a positive correlation between the particle emission and the loudness of vocalization, regardless of the language spoken. Asadi et al.[61] used the same experimental setup to analyze the effect of voice articulation on the particle emission rate. They were able to identify phones with higher droplets generation as well as observing that the number of emitted particles is proportional to the vowel content of the sentences.

He et al.[62] conducted a detailed study on the droplet emissions from wind instruments using APS measurements. Based on a comparison of the aerosol production from a wide range of wind instruments with that of normal breathing and speaking, they classified the instruments into three risk categories: low (e.g. tuba), intermediate (e.g. clarinet), and high risk (e.g. trumpet).

1.3.1.5 Other techniques

In addition to the techniques mentioned above, there are a few less frequently used techniques. Loudon and Roberts[46] tried to directly observe with a microscope the dry residues collected on a filter at the outlet of the box described in section 3.1.2 to collect the dry residues suspended in the air, inside the box. Authors observed that dry residues under 1 µm were not detectable although the lower detection limit of the microscope was 0.5 µm.

The Electrical Low-Pressure Impactor (ELPI, Dekati LTD) was used by Hersen *et al* [63] for the characterization of the size distribution of the cough dry residues produced by volunteers infected by influenza virus. The ELPI provides a real time determination of the droplets aerodynamic diameter in the size range of 0.007µm to 10 µm, classified into 12 size intervals. Hersen *et al.* collected the exhaled breath through a ventilated hood where the head of volunteers was placed. It is important to notice that when using such kind of hoods, the droplets interacts with the ventilation flow rate depending on their size. Therefore, the ventilation flow rate and the sampling point should be well studied. ELPI enables realtime measurements of the size distribution which

helps in studying the exhaled breath of a great number of volunteers, 78 individuals in Hersen *et al.*[63].

The Scanning Mobility Particle Sizer (SMPS) was another measurement technique that was used by[64] to measure the fine dry residues of the droplets generated by coughing. The particle size range of the SMPS is 0.02 µm to 0.6 µm. In this study Yang *et al.* SMPS has used in addition to APS to cover a wider size range, but almost no particles were observed in the size range of the SMPS.

1.3.2 Nonintrusive measurement techniques

Nonintrusive measurement techniques have been developed during the course of the last two decades. Most of these techniques are used to determine the size distribution of the exhaled droplets. Using a nonintrusive technique eliminates the bias due to physical phenomena such as evaporation and condensation during the sampling process. This makes these nonintrusive techniques particularly suitable for measuring the initial droplets size distribution and for studying the evaporation process. Moreover, some nonintrusive techniques are used to measure the velocity and size of the droplets at different positions in the exhaled jet.

1.3.2.1 High-speed photography

High-speed photography technique was previously discussed in section 1.2.1.1 for the characterization of the exhaled jet gas phase, through capturing images of tracer particles. This technique is also used to characterize the exhaled droplets dispersion. Zhu et al.[26] studied the transport of droplets produced by coughing. To visualize the transport of the saliva droplets, the subjects' mouths were covered with flour and then the dispersion of the saliva droplets with flour particles was analyzed. The study showed that the droplets travel with high velocity during the first 30 cm. Then the droplets velocity decreases and the maximum observed travel distance in this study was 2m. Despite the role of the flour in visualizing the saliva droplets, the presence of this flour might affect the evaporation of the droplets and hence their dispersion. Nishimura *et al.*[65] claimed to be the first to study the dynamics of the droplets expelled during coughing and sneezing. They developed a digital high-vision, high-speed video system to capture the movement of the droplets. A PIV image processing software was employed to track the brightness signal of the captured images and the obtained data is represented in a form of velocity vectors. Using this technique, they found that the initial average velocity of cough droplets of two subjects was $5 m.s^{-1}$, and after 84 cm these droplets lost their momentum. When considering sneezing, they determined corresponding values of $6 m.s^{-1}$ and 30 cm, only. This measurement technique does not provide information about the droplet size. Bourouiba *et al.*[20] also used this measurement technique based on high-speed photography of exhaled droplets. Through streak imaging technique, they were able to produce a picture of the droplets' trajectory, showing that large droplets follow a ballistic path depending on their size while small droplets followed the turbulent

airflow. The minimum detectable droplet size depends on the performance of the optical setup and the digital camera.

1.3.2.2 Digital Inline Holography

In contrary to normal photography that affords only an image of intensity variations, holography records light phase which results in the production of 3D pictures. In conventional holography, a beam from a coherent light source or laser is split into two beams; one illuminating the object itself and the other providing a reference. The object-illuminating beam is recombined, after being reflected by the body, with the reference beam which creates a phase interference that is registered onto the hologram plate. To retrieve the object, the plate is lit by a coherent light beam identical to the reference beam used at the recording of the hologram. It permits 3D viewing of the original object exactly as registered with all its optical information retrieved, but topographical or vertical measurements are yet possible.

In Digital Inline Holography (DIH), recently developed, the same phase interference concept is used to register holographic images using a digital camera. The camera then feeds the information into a computer program that numerically reconstructs the images. The numerical reconstruction process permits immediate quantitative access to the intensity and phases of topographic measurements accurate down to the nanometric scale. However, there is always a compromise between the measurement scale and measurement volume.

Shao et al.[66] used the DIH to measure the shape, size, and concentration of the droplet generated during breathing. The DIH used system detects particles and droplets in the range of 0.5µm - 50 µm. The particle concentration was 170 part.L^{-1}, and the average size was 1.7 µm at 1.5 cm from the subject's mouth. Shao et al. observed irregular particle shapes in addition to well-rounded droplets. By defining a roundness threshold, the authors estimated that 33% of the particles emitted at a distance of 1.5 cm are not droplets.

1.3.2.3 Laser measurement techniques based on Mie theory

The laser measurement techniques relying on Mie theory are nonintrusive techniques that are based on the measurement of the amount of light scattered by the droplets. For the characterization of the exhaled droplets, Chao *et al.*[27] developed a device using this technique named Interferometric Mie Imaging (IMI) to measure the size distribution and the concentration of the droplets produced during coughing and speaking. IMI produced de-focused images of the droplets using a combination of a high-speed camera and laser sheet. The droplet diameter is obtained from the spatial frequency of the fringes in the image using geometrical analysis. The measurements were conducted at a distance of 10mm and 60 mm from the mouth and the data were analyzed to consider the evaporation. Chao *et al.* found that the geometric mean diameter for coughing and speaking are respectively 13.5 µm and 16.0 µm. The results obtained with the

IMI showed good agreement with previous studies from Duguid[44] and Loudon & Roberts[46]. However, the measurement volume of the IMI system is about 60 mm^3, which is much smaller than the total exhaled air volume. Thus, these results are insufficient to provide information about the total droplet number or droplet concentration. To overcome this limitation, Chao et al. used two estimation methods. The first estimation method was to divide the total volume of droplets by the size distribution obtained by IMI. The disadvantage of this method is the lack of information about the total droplet volume, as only two studies characterized the size of the droplets using collection instead of sampling techniques[44,46]. The second method was to obtain the droplet concentration by dividing the number of the sampled droplets over the IMI measurement volume. Calculating the droplet concentration using this second method assumes a uniform droplet concentration over the whole expelled air volume. This assumption could be confirmed by conducting IMI measurements at different locations covering a larger flow crossectional area.

This technique was also used to study the droplet dispersion in different environments. Chao and Wan[67] used this technique to validate a numerical model that compares the effect of two ventilation systems on the droplet dispersion, unidirectional downward and ceiling-return ventilation. The measurements were conducted in a Class 100 cleanroom where the supply air is vented through the roof toward a perforated-tiles floor to maintain the room at 21°C and 55% RH. A PIV system was used to capture the flow patterns and turbulence intensity inside the room while the size measurement of the cough-like droplets was performed by using Interferometric Mie Imaging (IMI) technique. The study demonstrated that the droplet of $\leq 45\mu m$ diameter dried out before deposition or extraction by ventilation system while the large droplet, $\geq 87.5\mu m$, settle down before complete evaporation.

Laser particle size analyzer is another device that is based on the Mie theory. In this technique, a laser beam is used to illuminate a control volume that can contain multiple droplets, and the angular variation in the intensity of scattered light is directly related to the droplet diameter. The distribution of the sneezing droplets was studied by Han *et al.*[68] using a laser particle size analyzer with a wide size range 0.1 µm -1000 µm. Han *et al.* found that the geometrical mean of the unimodal distribution is 360.1 µm (SD=1.5) and 74.4 µm for bimodal distribution (SD=1.7). Another study by Zayas *et al.*[69] also used the laser particle analyzer to measure the size distribution and concentration of the coughing droplets from 54 healthy subjects. The size range of the analyzer was 0.1-900 µm divided into 60 size intervals. Despite the size range difference when compared to the OPC, Zayas *et al.* concluded that 97% of measured particles have diameters lower than 1 micron, which is in accordance with values obtained by OPC. Although this technique is capable of measuring the large droplets diameter, in this experiment the distance between the mouth subject and the center of the measurement volume was 17 cm. Given the normal room conditions, evaporation effect cannot be ignored over this distance, which might explain the predominance of submicronic particles.

1.4 Comment on disease transmission

This paper is divided into two-part, namely airflow and droplets characterization. However, when considering airborne disease transmission, the interaction of the droplets with the airflow is a crucial issue. Table 1 lists all the experimental measured parameters for human breathing, coughing, speaking and sneezing. These parameters contain boundary and initial flow conditions such as temperature, humidity, initial velocity, mouth/nose area which are essential for modeling. Other measured parameters characterize the propagation of the flow which is of particular interest when analyzing the host-to-host transmission route. However, the relation between airflow propagation and airborne disease transmission is not direct as the viability of the pathogens depends not only on the flow characteristics but also on the type of the pathogen. Moreover, a recent study by Bourouiba et al.[70] using high-speed photography, shows that the average flow parameters are not sufficient to study the droplet -flow interaction. Instead, the flow structure contains vortices that entrain droplet clusters in warm and moist gas clouds. Bourouiba et al. report that the effect of this gas cloud can extend the lifetime of the droplets expelled during coughing up to 1000 times and the droplets travel up to 7-8 m from the source. This distance varies significantly from air propagation distance shown in Table 1, which highlights the necessity for more quantitative measurement on the exhaled droplets motion and evaporation.

1.5 Conclusion

In our review, we classified the exhaled airflow measurements techniques into two categories: global flow-field measurements, and pointwise measurements. Three global flow-field measurement techniques were identified, namely the high-speed photography, schlieren photography and Particle Image Velocimetry (PIV). These techniques provide information on the whole flow-field, and helps understanding the interactions between the exhaled flow, the thermal plume and the room airflow. The high-speed photography and the schlieren photography were applied to study the flow shape and its propagation into the space while the PIV was applied where detailed quantitative data of the velocity field was required. The pointwise measurements were used to measure the initial temperature, initial humidity and velocity. To identify the points at which pointwise measurements should be conducted, one of the global flow field measurement technique often precedes pointwise measurements. In the experiments where PIV measurements were applied to characterize the velocity field from human sources, the confinement effect due to the dimension of the box containing the tracer particles should be considered. The interpretation of measurement results should consider the applied measurement technique: this was clear for the propagation distance values found in literature, as values obtained by the schlieren photography were higher than those determined by the pointwise measurements.

The second part of the article summarizes the techniques applied for the characterization of the exhaled droplets and dry residues. These techniques can be used to determine three important

parameters: droplet or dry residues sizes distribution, droplet velocity distribution, and traveled distance. Apart for three articles, all the reviewed articles in this section measured the size distribution of the droplets and/or the dry residues. Solid impaction, droplet deposition analysis, optical particle counter, aerodynamic particle sizer, electrical low-pressure impactor scanning Mobility Particle Sizer, Liquid impingers and filtration are the techniques used to measure the size distribution of the dry residues. Depending on the measurement principle, some correlation between the initial droplet diameter and the dry residues diameter could be applied to estimate the initial size of the droplets.

The evolution of the droplet size is important to study the transmission of the airborne diseases. It controls the droplet dynamics and determines the physical history of the living microorganisms transported in droplets. Limited experimental data is available to validate the evaporation models used in the analysis of the deposition and dispersion of the exhaled droplets. The used evaporation models[71,72,73] are validated versus experimental data obtained from a freefall evaporating droplet[74] or a stagnant droplet[75]. Despite the capability of IMI technique and Laser particle size analyzer in tracking the size evolution and velocity of the droplets over distance, only one single study applied IMI to trace droplets size and velocity over distance[67]. In addition, the Phase Doppler Anemometry technique, which is used in other applications to track the size and velocity of droplets over distance[76], could also be used to track the droplets inside human exhaled jet.

1.6 References

1. Morawska L, Milton DK. It is Time to Address Airborne Transmission of COVID-19. *Clin Infect Dis*. July 2020. July 6, 2020. https://academic.oup.com/cid/advance-article/doi/10.1093/cid/ciaa939/5867798. Accessed July 16, 2020.
2. Bahl P, Doolan C, de Silva C, Chughtai AA, Bourouiba L, MacIntyre CR. Airborne or Droplet Precautions for Health Workers Treating Coronavirus Disease 2019? *J Infect Dis*. April 2020. April 16, 2020. https://academic.oup.com/jid/advance-article/doi/10.1093/infdis/jiaa189/5820886. Accessed July 17, 2020.
3. Li Y, Qian H, Hang J, et al. *Evidence for Probable Aerosol Transmission of SARS-CoV-2 in a Poorly Ventilated Restaurant*. Infectious Diseases (except HIV/AIDS); 2020. April 22, 2020. http://medrxiv.org/lookup/doi/10.1101/2020.04.16.20067728. Accessed July 16, 2020.
4. Miller SL, Nazaroff WW, Jimenez JL, et al. *Transmission of SARS-CoV-2 by Inhalation of Respiratory Aerosol in the Skagit Valley Chorale Superspreading Event*. Infectious Diseases (except HIV/AIDS); 2020. June 17, 2020. http://medrxiv.org/lookup/doi/10.1101/2020.06.15.20132027. Accessed July 16, 2020.
5. Chan JF-W, Yuan S, Kok K-H, et al. A familial cluster of pneumonia associated with the 2019 novel coronavirus indicating person-to-person transmission: a study of a family cluster. *The Lancet*. 2020;395:514–523.
6. Zhang J, Tian S, Lou J, Chen Y. Familial cluster of COVID-19 infection from an asymptomatic. *Crit Care*. 2020;24. December 2020. https://ccforum.biomedcentral.com/articles/10.1186/s13054-020-2817-7. Accessed September 17, 2020.

7. Sun Y, Tian L, Du X, Wang H, Li Y, Wu R. Epidemiological and clinical characteristics of a familial cluster of COVID-19. *Epidemiol Infect*. 2020;148. 2020. https://www.cambridge.org/core/product/identifier/S0950268820001521/type/journal_article. Accessed September 17, 2020.
8. Li Y, Peng S, Li L, et al. Clinical and Transmission Characteristics of Covid-19 — A Retrospective Study of 25 Cases from a Single Thoracic Surgery Department. *Curr Med Sci*. 2020;40:295–300.
9. Ong SWX, Tan YK, Chia PY, et al. Air, Surface Environmental, and Personal Protective Equipment Contamination by Severe Acute Respiratory Syndrome Coronavirus 2 (SARS-CoV-2) From a Symptomatic Patient. *JAMA*. 2020;323:1610.
10. Van Doremalen N, Bushmaker T, Morris DH, et al. Aerosol and Surface Stability of SARS-CoV-2 as Compared with SARS-CoV-1. *N Engl J Med*. 2020;382:1564–1567.
11. Morawska L, Johnson G, Ristovski Z, et al. Droplets expelled during human expiratory activities and their origin. :8.
12. Siegel JD, Rhinehart E, Jackson M, Chiarello L. 2007 Guideline for Isolation Precautions: Preventing Transmission of Infectious Agents in Health Care Settings. *Am J Infect Control*. 2007;35:S65–S164.
13. Melikov AK. Human body micro-environment: The benefits of controlling airflow interaction. *Build Environ*. 2015;91:70–77.
14. Gupta JK, Lin C-H, Chen Q. Flow dynamics and characterization of a cough: Flow dynamics and characterization of a cough. *Indoor Air*. 2009;19:517–525.
15. Gupta JK, Lin C-H, Chen Q. Characterizing exhaled airflow from breathing and talking. *Indoor Air*. 2010;20:31–39.
16. Xu C, Nielsen PV, Liu L, Jensen RL, Gong G. Human exhalation characterization with the aid of schlieren imaging technique. *Build Environ*. 2017;112:190–199.
17. Tang JW, Nicolle AD, Klettner CA, et al. Airflow Dynamics of Human Jets: Sneezing and Breathing - Potential Sources of Infectious Aerosols. Subbiah E, ed. *PLoS ONE*. 2013;8:e59970.
18. Tang JW, Liebner TJ, Craven BA, Settles GS. A schlieren optical study of the human cough with and without wearing masks for aerosol infection control. *J R Soc Interface*. 2009;6:S727–S736.
19. Kwon S-B, Park J, Jang J, et al. Study on the initial velocity distribution of exhaled air from coughing and speaking. *Chemosphere*. 2012;87:1260–1264.
20. Bourouiba L, Dehandschoewercker E, Bush JWM. Violent expiratory events: on coughing and sneezing. *J Fluid Mech*. 2014;745:537–563.
21. Liu S, Novoselac A. Transport of Airborne Particles from an Unobstructed Cough Jet. *Aerosol Sci Technol*. 2014;48:1183–1194.
22. Höppe P. Temperatures of expired air under varying climatic conditions. *Int J Biometeorol*. 1981;25:127–132.
23. Tang JW, Nicolle A, Pantelic J, et al. Airflow Dynamics of Coughing in Healthy Human Volunteers by Shadowgraph Imaging: An Aid to Aerosol Infection Control. Vijaykrishna D, ed. *PLoS ONE*. 2012;7:e34818.
24. Cao X, Liu J, Jiang N, Chen Q. Particle image velocimetry measurement of indoor airflow field: A review of the technologies and applications. *Energy Build*. 2014;69:367–380.
25. VanSciver M, Miller S, Hertzberg J. Particle Image Velocimetry of Human Cough. *Aerosol Sci Technol*. 2011;45:415–422.
26. Zhu S, Kato S, Yang J-H. Study on transport characteristics of saliva droplets produced by coughing in a calm indoor environment. *Build Environ*. 2006;41:1691–1702.

27. Chao CYH, Wan MP, Morawska L, et al. Characterization of expiration air jets and droplet size distributions immediately at the mouth opening. *J Aerosol Sci*. 2009;40:122–133.
28. Savory E, Lin WE, Blackman K, et al. Western Cold and Flu (WeCoF) aerosol study – preliminary results. *BMC Res Notes*. 2014;7:563.
29. Risti S, Isakovi J, Ili B, Ocokolji G. Review of methods for flow velocity measurement in wind tunnels. 2004:12.
30. Feng L, Yao S, Sun H, Jiang N, Liu J. TR-PIV measurement of exhaled flow using a breathing thermal manikin. *Build Environ*. 2015;94:683–693.
31. Jiang N, Yao S, Feng L, Sun H, Liu J. Experimental study on flow behavior of breathing activity produced by a thermal manikin. *Build Environ*. 2017;123:200–210.
32. Berlanga FA, Olmedo I, Ruiz de Adana M. Experimental analysis of the air velocity and contaminant dispersion of human exhalation flows. *Indoor Air*. 2017;27:803–815.
33. Mahajan RP, Singh P, Murty GE, Aitkenhead AR. Relationship between expired lung volume, peak flow rate and peak velocity time during a voluntary cough manoeuvre. *Br J Anaesth*. 1994;72:298–301.
34. Singh P, Mahajan RP, Murty GE, Aitkenhead AR. Relationship of peak flow rate and peak velocity time during voluntarv couzhinc. *BJA Br J Anaesth*. 1995;74:714–716.
35. Xu C, Nielsen PV, Gong G, Liu L, Jensen RL. Measuring the exhaled breath of a manikin and human subjects. *Indoor Air*. 2015;25:188–197.
36. Xu C, Nielsen PV, Gong G, Jensen RL, Liu L. Influence of air stability and metabolic rate on exhaled flow. *Indoor Air*. 2015;25:198–209.
37. Wells W. On Air-Borne Infection: Study Ii. Droplets and Droplet Nuclei. *American Journal of Epidemiology*. 1934;20:611–618.
38. Milton DK, Fabian MP, Cowling BJ, Grantham ML, McDevitt JJ. Influenza Virus Aerosols in Human Exhaled Breath: Particle Size, Culturability, and Effect of Surgical Masks. *PLOS Pathog*. 2013;9:7.
39. Lindsley WG, Blachere FM, Thewlis RE, et al. Measurements of Airborne Influenza Virus in Aerosol Particles from Human Coughs. Pekosz A, ed. *PLoS ONE*. 2010;5:e15100.
40. Fabian P, McDevitt JJ, DeHaan WH, et al. Influenza Virus in Human Exhaled Breath: An Observational Study. Fouchier RAM, ed. *PLoS ONE*. 2008;3:e2691.
41. Xie X, Li Y, Chwang ATY, Ho PL, Seto WH. How far droplets can move in indoor environments – revisiting the Wells evaporation–falling curve. *Indoor Air*. 2007;17:211–225.
42. Gralton J, Tovey E, McLaws M-L, Rawlinson WD. The role of particle size in aerosolised pathogen transmission: A review. *J Infect*. 2011;62:1–13.
43. Baron PA, Kulkarni P, Willeke K, eds. *Aerosol Measurement: Principles, Techniques, and Applications*. 3rd ed. Hoboken, N.J: Wiley; 2011.
44. Duguid JP. The size and the duration of air-carriage of respiratory droplets and droplet-nuclei. *J Hyg (Lond)*. 1946;44:471–479.
45. Fennelly KP, Martyny JW, Fulton KE, Orme IM, Cave DM, Heifets LB. Cough-generated Aerosols of *Mycobacterium tuberculosis*: A New Method to Study Infectiousness. *Am J Respir Crit Care Med*. 2004;169:604–609.
46. Loudon RG, Roberts RM. Droplet Expulsion from the Respiratory TRACT. 1967:8.
47. LI Y, Chwang ATY, Ho PL, Seto WH, Yuen PL. Understanding droplets produced by nebulisers and respiratory activities. *Hong Kong Medical Journal*. 2008;14:29–32.

48. Xie X, Li Y, Sun H, Liu L. Exhaled droplets due to talking and coughing. *J R Soc Interface*. 2009;6:S703–S714.
49. Johnson GR, Morawska L, Ristovski ZD, et al. Modality of human expired aerosol size distributions. *J Aerosol Sci*. 2011;42:839–851.
50. Fabian P, Brain J, Houseman EA, Gern J, Milton DK. Origin of Exhaled Breath Particles from Healthy and Human Rhinovirus-Infected Subjects. *J Aerosol Med Pulm Drug Deliv*. 2011;24:137–147.
51. Edwards DA, Man JC, Brand P, et al. Inhaling to mitigate exhaled bioaerosols. *Proc Natl Acad Sci*. 2004;101:17383–17388.
52. Holmgren H. *On the Formation and Physical Behaviour of Exhaled Particles*. Göteborg: Chalmers Univ. of Technology; 2011.
53. Almstrand A-C, Bake B, Ljungström E, et al. Effect of airway opening on production of exhaled particles. *J Appl Physiol*. 2010;108:584–588.
54. Papineni RS, Rosenthal FS. The Size Distribution of Droplets in the Exhaled Breath of Healthy Human Subjects. *J Aerosol Med*. 1997;10:105–116.
55. Wurie F, Le Polain de Waroux O, Brande M, et al. Characteristics of exhaled particle production in healthy volunteers: possible implications for infectious disease transmission. *F1000Research*. 2013;2:14.
56. Wurie FB, Lawn SD, Booth H, Sonnenberg P, Hayward AC. Bioaerosol production by patients with tuberculosis during normal tidal breathing: implications for transmission risk. *Thorax*. 2016;71:549–554.
57. TSI. *Model 3321 Aerodynamic Particle Sizer Spectrometer Instruction Manual*.; :109.
58. Morawska L, Johnson GR, Ristovski ZD, et al. Size distribution and sites of origin of droplets expelled from the human respiratory tract during expiratory activities. *J Aerosol Sci*. 2009;40:256–269.
59. Fang L, Lau A, Chan C, Hung C, Lee T. Aerodynamic properties of biohazardous aerosols in hospitals. *Hong Kong Medical Journal*. 2008;14:26–28.
60. Asadi S, Wexler AS, Cappa CD, Barreda S, Bouvier NM, Ristenpart WD. Aerosol emission and superemission during human speech increase with voice loudness. *Sci Rep*. 2019;9. December 2019. http://www.nature.com/articles/s41598-019-38808-z. Accessed February 18, 2020.
61. Asadi S, Wexler AS, Cappa CD, Barreda S, Bouvier NM, Ristenpart WD. Effect of voicing and articulation manner on aerosol particle emission during human speech. Yen H-L, ed. *PLOS ONE*. 2020;15:e0227699.
62. He R, Gao L, Trifonov M, Hong J. Aerosol generation from different wind instruments. *J Aerosol Sci*. 2021;151:105669.
63. Hersen G, Moularat S, Robine E, et al. Impact of Health on Particle Size of Exhaled Respiratory Aerosols: Case-control Study. *CLEAN - Soil Air Water*. 2008;36:572–577.
64. Yang S, Lee GWM, Chen C-M, Wu C-C, Yu K-P. The Size and Concentration of Droplets Generated by Coughing in Human Subjects. *J Aerosol Med*. 2007;20:484–494.
65. Nishimura H, Sakata S, Kaga A. A New Methodology for Studying Dynamics of Aerosol Particles in Sneeze and Cough Using a Digital High-Vision, High-Speed Video System and Vector Analyses. Harrod K, ed. *PLoS ONE*. 2013;8:e80244.
66. Shao S, Zhou D, He R, et al. Risk assessment of airborne transmission of COVID-19 by asymptomatic individuals under different practical settings. *J Aerosol Sci*. 2021;151:105661.
67. Chao CYH, Wan MP. A study of the dispersion of expiratory aerosols in unidirectional downward and ceiling-return type airflows using a multiphase approach. *Indoor Air*. 2006;16:296–312.

68. Han ZY, Weng WG, Huang QY. Characterizations of particle size distribution of the droplets exhaled by sneeze. *J R Soc Interface*. 2013;10:20130560–20130560.
69. Zayas G, Chiang MC, Wong E, et al. Cough aerosol in healthy participants: fundamental knowledge to optimize droplet-spread infectious respiratory disease management. *BMC Pulm Med*. 2012;12. December 2012. https://bmcpulmmed.biomedcentral.com/articles/10.1186/1471-2466-12-11. Accessed March 3, 2019.
70. Bourouiba L. Turbulent Gas Clouds and Respiratory Pathogen Emissions: Potential Implications for Reducing Transmission of COVID-19. *JAMA*. March 2020. March 26, 2020. https://jamanetwork.com/journals/jama/fullarticle/2763852. Accessed July 19, 2020.
71. Chen C, Zhao B. Some questions on dispersion of human exhaled droplets in ventilation room: answers from numerical investigation. *Indoor Air*. 2010;20:95–111.
72. Gao N, Niu J, He Q, Zhu T, Wu J. Using RANS turbulence models and Lagrangian approach to predict particle deposition in turbulent channel flows. *Build Environ*. 2012;48:206–214.
73. Wei J, Li Y. Airborne spread of infectious agents in the indoor environment. *Am J Infect Control*. 2016;44:S102–S108.
74. Kukkonen J, Vesala T, Kulmala M. The interdependence of evaporation and settling for airborne freely falling droplets. *J Aerosol Sci*. 1989;20:749–763.
75. Liu L, Wei J, Li Y, Ooi A. Evaporation and dispersion of respiratory droplets from coughing. *Indoor Air*. 2017;27:179–190.
76. Castanet G, Lebouché M, Lemoine F. Heat and mass transfer of combusting monodisperse droplets in a linear stream. *Int J Heat Mass Transf*. 2005;48:3261–3275.

1.7 The turbulent round jet

The problem of the turbulent jet was a subject of a study for scientists and engineers since the 1930s [Zhivov et al., 2020], because of its significance in several engineering and environmental areas. The jet is a fluid flow induced by a pressure drop through an orifice. By the free round turbulent stationary jet, we mean a fluid that emerges, unobstructed, from a circular nozzle of diameter D with a uniform initial velocity U_0. As the flow propagates into the surrounding environment, it entrains ambient air, and its diameter enlarges. Morton et al. [1956] developed the entrainment hypothesis, which states that the speed of the ambient entrained fluid is proportional to the average jet speed. As a result, the jet radius increases in this model linearly with the distance from the source.

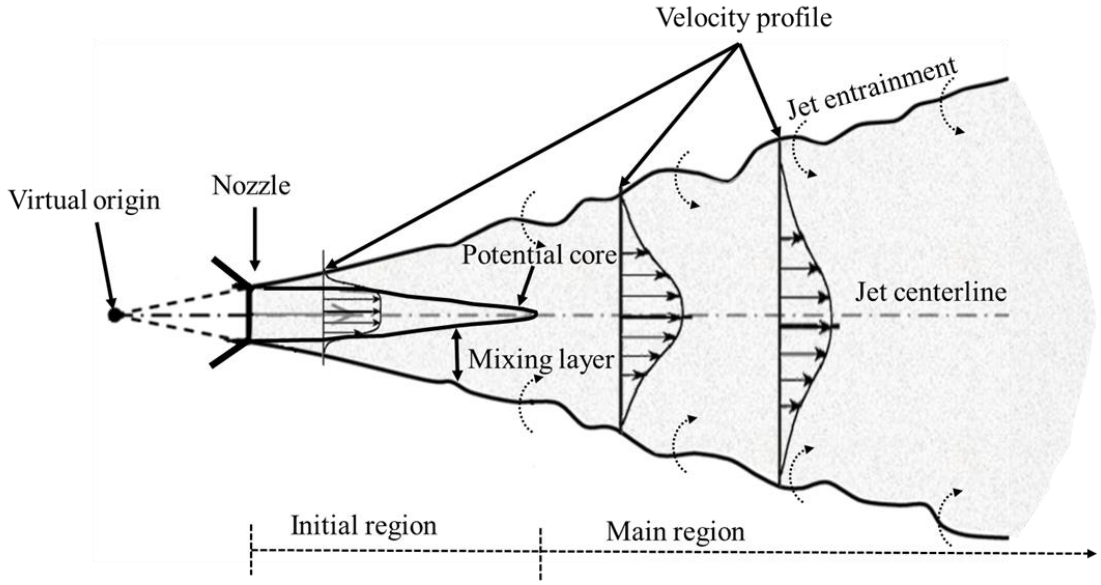

Figure 1.3 : The entrainment of the ambient air inside the turbulent round jet

Figure 1.3 illustrates the classical description of the jet structure, which is mainly composed of two regions. The flow development region and the established flow region also known as the initial region and main region, respectively. The development region or initial region contains two parts: the jet core and the mixing layer. The jet core has a conic shape where the centerline streamwise velocity of the jet remains almost constant. Around the jet core, near the jet borders, the ambient air is accelerated by the shear forces which induces momentum transfer between the jet and the surrounding air. The region where this momentum exchange occurs is called the mixing layer. The instability of the shear layer at the flow borders forms vortices that entrain the ambient air into the jet. Figure 1.4 presents a high-speed visualization of a turbulent round jet

with Reynolds number around 5000. The subsequent images, taken with 5 ms time interval, show the structure of the jet vortices and their evolution. As the flow proceeds the mixing layer grows and reaches the jet center, this is where the established flow region or the main flow region begins. In this region, established flow region, the flow is fully developed and the centerline velocity of the jet decreases with the distance from the source.

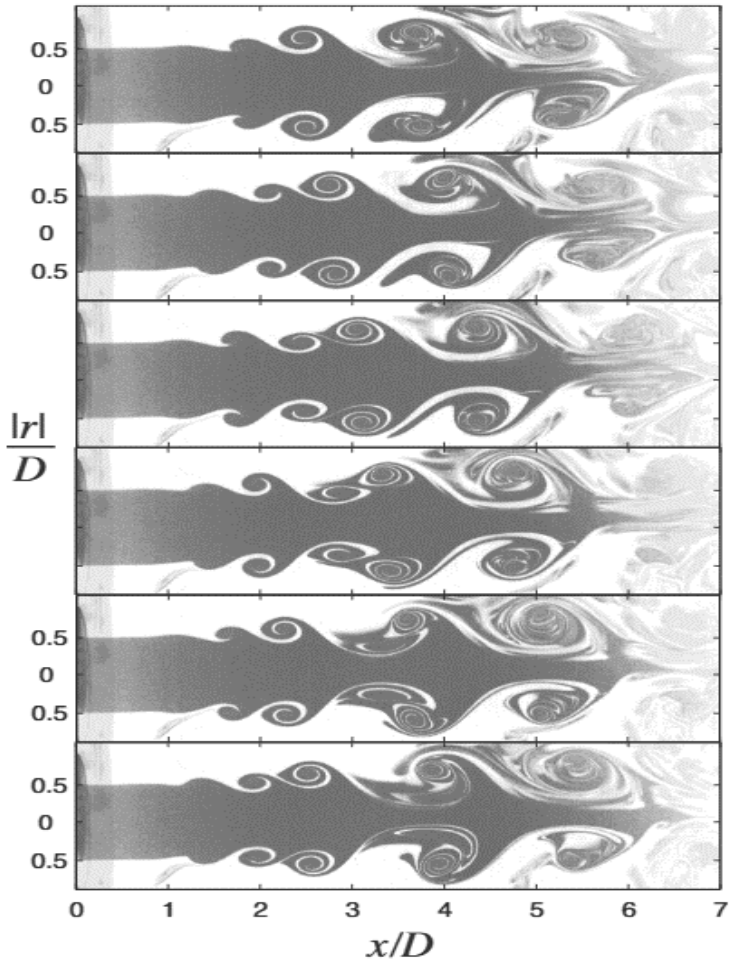

Figure 1.4 : Subsequent snapshots of a round air jet with Re ≈ 5000 issuing into air at rest, with a time interval of 5 ms. [Orlu, 2009]

In the following sections, we will describe a model for the mean velocity field. Although most of the presented equations are valid for both vertical and horizontal round jet configurations, we will be concentrating on the latter.

1.7.1 Centerline velocity decay

For this horizontal jet, the jet central axis is assumed to be on the x-axis, and the velocity profiles presented in Figure 1.1 are on the (x,z) plane. The centerline jet velocity is the velocity along the central axis of the jet, where the maximum of the velocity profile at distance x from the source occurs. In the potential core region of the jet, only a slight change in this centerline velocity is observed. However, as the momentum of the flow is constant and since the mass increases with more air entrained in the mixing layer, the centerline velocity decays over distance. The determination of the centerline velocity decay is the first step in the characterization of the jet flow field. Wygnanski and Fiedler [1969] proposed a relation between the centerline velocity and the distance from the jet opening that is shown in equ. 1.

$$U_c = C\, U_o \left(\frac{(x + x_o)}{D}\right)^{-1} \qquad \textit{equ. 1}$$

Where U_c is the centerline velocity, U_o is the initial velocity at the nozzle exit, and C is the jet entrainment coefficient.

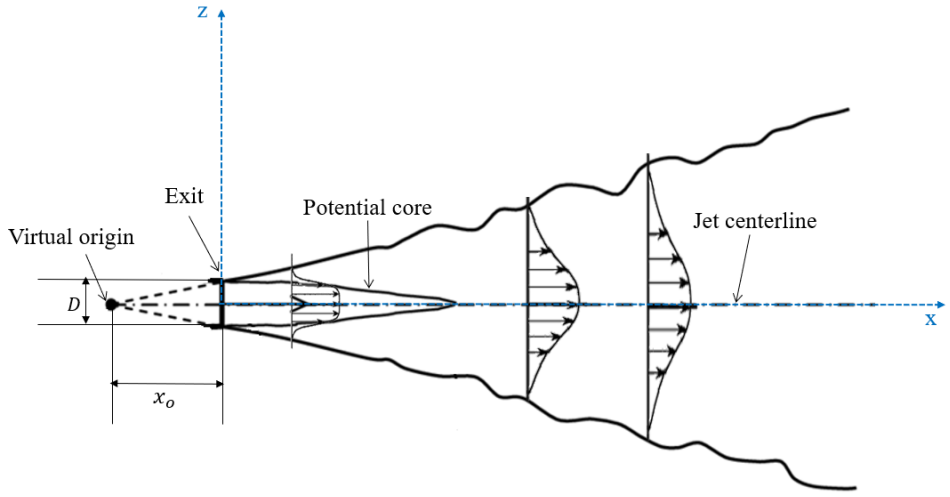

Figure 1.5 : The geometry of the turbulent round jet

In Figure 1.5 the jet geometry is illustrated as well as the adopted coordinates system. D is the initial diameter, corresponding to the nozzle diameter located at x=0, that is not represented in this figure. x_o is the distance between the virtual origin of the jet and the nozzle exit (x=0), which is the point from which the jet begins, if it begins from a precise point. Abdel-Rahman et al. [1997] distinguished two virtual points of origin, geometric and dynamic. The geometric virtual

origin which is the tip of the jet which is obtained by completing the conic shape of the round jet. The dynamic virtual origin is not necessarily equal to the geometric origin, and it depends on the initial conditions of the flow. The dynamic virtual origin can have both positive and negatives values, by negative values it means that it can be outside the jet core downstream to the flow actual origin. Despite the absence of a complete physical meaning of the dynamic virtual origin of the jet, it is found to be important when interpreting the experimental results of the centerline velocity decay.

$$\frac{U_o}{U_c} = \frac{1}{C}\left(\frac{(x + x_o)}{D}\right) \qquad \textit{equ. 2}$$

equ. 2 presents a dimensionless form for the inverse evolution of the mean centerline velocity with distance from the nozzle, which is used in literature to compare flows with different outlet conditions. Papadopoulos and Pitts [1999] explored the decay of the centerline velocity of an air jet produced by a long straight pipe of 6 mm with a sharp-edge exit. The air jet was a fully developed turbulent jet at the pipe exit, and in temperature equilibrium with the ambient flow. The measurements were conducted using a hot-wire anemometer along the jet centerline up to 18 diameters downstream. By controlling the airflow using a mass flowmeter they tested the velocity decay for four Reynolds numbers, 4800, 9000, 13300, and 17500. Figure 4 shows the dimensionless inverse decay for the mean centerline velocity. The horizontal part at the beginning of the curve implies that these measurements were conducted inside the jet core. There was no significant effect of the Reynolds number on the velocity decay up to x/D=5. The effect of the Reynolds numbers appears later downstream with a relatively higher slope $(1/C)$ for larger Re numbers.

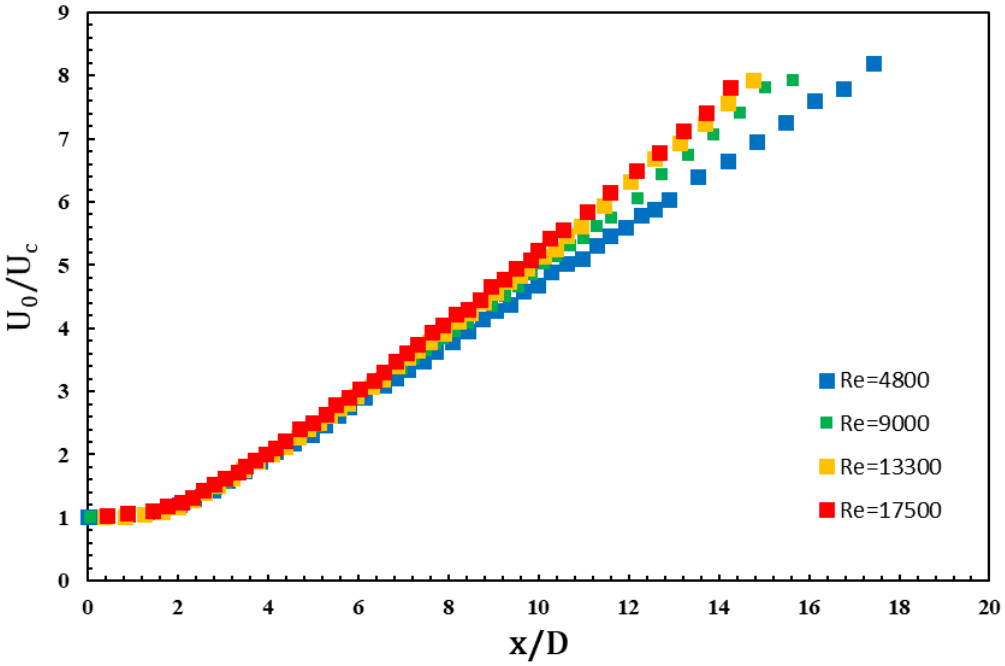

Figure 1.6 : The evolution of the centerline velocity with distance from the jet source at different Re [Papadopoulos and Pitts, 1999]

1.7.2 Mean velocity profiles

The velocity on the main streamwise direction U_x, the horizontal direction in this case, follows a gaussian distribution according to experimental findings [List, 1982] [Lee and Chu 2003]. A theoretical basis to this distribution was provided by Reichardt [1942] [Mih, 1989]. This gaussian profile of the axial velocity is expressed as a function of the centerline velocity U_c, the radial distance *z*, and the axial distance from the source *x*. According to Zhivov et al. [2020], there are two equations proposed by Reichardt [1942], *equ. 3*, and Schlichting [1930], *equ. 4* :

$$\frac{U_x}{U_c} = exp(-\eta^2) \qquad \textit{equ. 3}$$

$$\frac{U_x}{U_c} = \left(1 - \eta^{\frac{3}{2}}\right)^2 \qquad \textit{equ. 4}$$

Where $= \frac{z}{(x+x_o)\beta}$, and β is the spread rate constant of the jet. Based on several experimental studies [Reichardt, 1942] [Abramovich, 1963] [Wygnanski and Fiedler, 1969] [List, 1982] [Zhivov et al., 2020] the value of β ranges from 0.085 to 0.151. In in *Figure 1.7*, the axial velocity $\frac{U_x}{U_c}$ is plotted versus η using *equ. 3*.

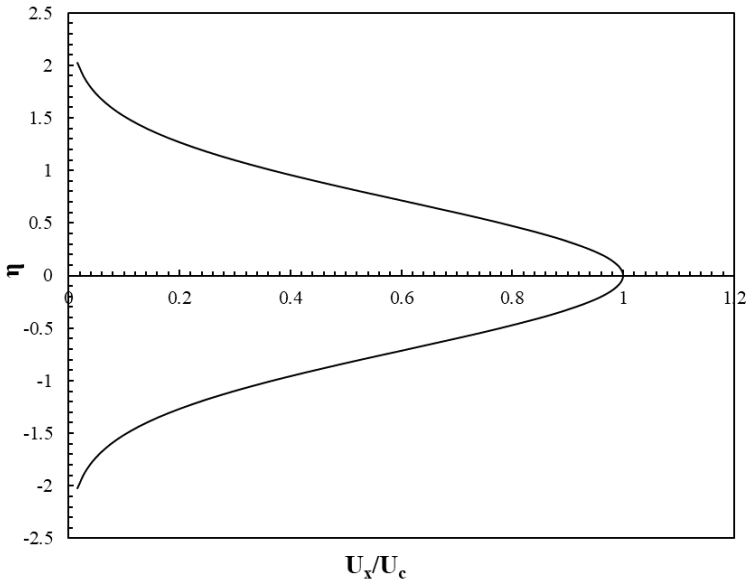

Figure 1.7 : The axial velocity component of the turbulent round jet

By integrating the continuity equation and assuming the gaussian distribution, Mih [1989] expressed the radial velocity component U_z, as a function of and U_c, z, and axial distance x.

$$\frac{U_z}{U_c} = \frac{\beta}{2\eta}\left(-1 + exp(-\eta^2) + 2\eta^2\, exp(-\eta^2)\right) \qquad \textit{equ. 5}$$

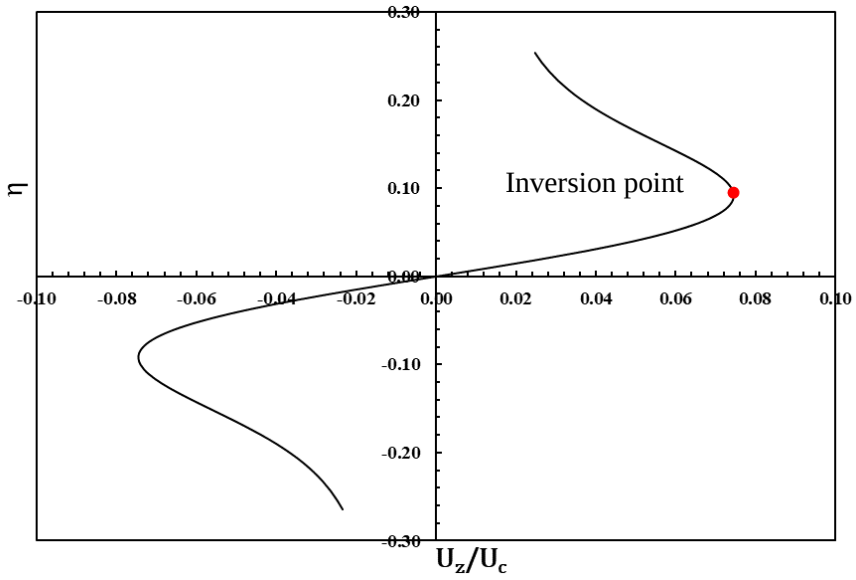

Figure 1.8 : The radial velocity component of the turbulent round jet

Figure 1.8 shows the radial velocity profile at distance x from the source as expressed in *equ. 5*. At the jet centerline the radial velocity is zero while the axial velocity is maximum. On the upper half of the jet, the radial velocity increases in the outward direction of the flow. The radial velocity reaches its maximum value at the inversion point (see *Figure 1.8*). After the inversion point, the value of the radial velocity decreases in the outward direction of the jet.

1.7.3 Jet spread angle

The jet spreading is characterized by the jet half-width φ^{50} which corresponds to the transverse coordinate for which the value of the velocity is half of that on the jet centerline. According to the entrainment hypothesis, the jet width increases linearly with distance.

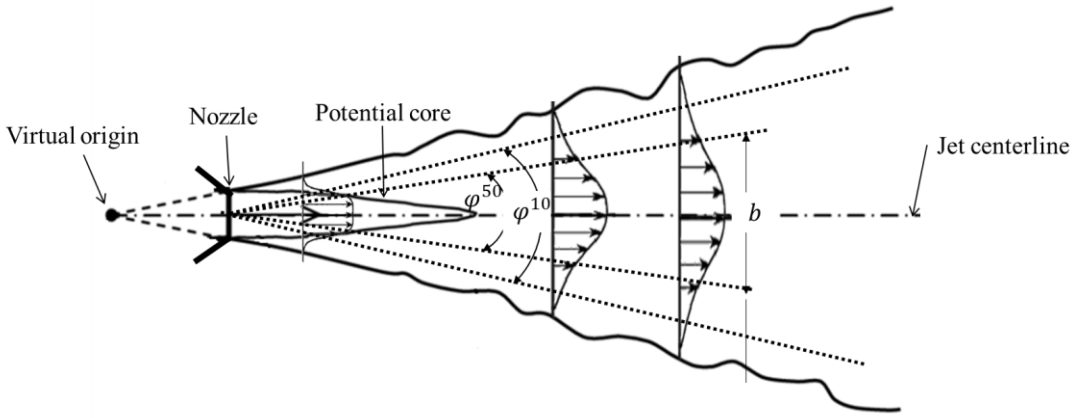

Figure 1.9 : The jet spread angle and the jet half-width

If the full width of the jet is *2b*, then jet half-width *b*, see *Figure 1.9*, could be expressed in the form shown in *equ. 6*:

$$b = \frac{(x + x_o)}{C} \qquad \textit{equ. 6}$$

Where, C is the entrainment coefficient of the jet and x_o is the virtual origin.

In the case of steady jets, the expansion rate remains almost constant, however it changes significantly from one flow configuration to another. The jet expansion could be also expressed in a form of spread angle φ^{50} as shown in *equ. 7*.

$$\varphi^{50} = tan^{-1}\left(\frac{b}{(x + x_o)}\right) = tan^{-1}\left(\frac{1}{C}\right) \qquad \textit{equ. 7}$$

However, the angle defined above is not sufficient to describe the full jet zone. To study the particles dispersion in the jet it is important to define a new angle that covers most of the zone affected by the jet. This angle is φ^{10} and it is defined by b^{10} which correspond to the half-width of the jet for which the value of the velocity one tenth of that on the centerline [Guerra, 2004] (see *equ. 8*).

$$\varphi^{10} = tan^{-1}\left(\frac{1}{C}\sqrt{\frac{ln10}{ln2}}\right) \qquad equ.\ 8$$

1.8 Buoyant jet

The round turbulent jet discussed in the previous section is considered as a non-buoyant jet because the buoyancy effect is negligible. On the contrary, the plumes are the flows where the buoyancy force is completely dominant. The buoyant jets, discussed in the section, are both momentum and buoyancy driven. Near the jet exit, the momentum forces dominate the flow, and the flow field is similar to that of the isothermal jet. As the buoyant jet proceeds, it starts losing its initial momentum and the effect of the buoyancy forces starts to appear until finally, the flow behaves as a plume. There are mainly two flow configurations of the buoyant jets. The positive buoyant jets when both momentum and buoyancy act in the same direction, and negative buoyant jets when the buoyancy forces act in the opposite direction. For example, a hot jet discharged in the upward direction is a positive buoyant jet and when it is expelled downward it is a negatively buoyant jet. Horizontally projected jets behave like vertical buoyant jets in the far-field.

The change from a momentum dominant jet to a buoyancy dominant plume, during the propagation of the buoyant jet, depends on the initial Froude number of the jet.

$$F = \frac{{U_o}^2}{gD}\frac{T_\infty}{(T_o - T_\infty)} \qquad equ.\ 9$$

Where, U_o is the exit velocity, D is the diameter of the exit nozzle, T_∞ is the temperature of the ambient flow and T_o is the exit jet temperature. According to Zhivov et al. [2020], Grimitlyn, [1982] proposed a local Archimedes number to characterize the relationship between the momentum forces and the buoyancy forces at a certain location, x, in the jet. The local Archimedes number Ar_x for the round jet is

$$Ar_x = \frac{K_2}{{K_1}^2} Ar_o \left(\frac{x}{\sqrt{A_o}}\right)^2 \qquad equ.\ 10$$

Where, A_o is the area of the exit, Ar_o is Archimedes number at the exit

$$Ar_0 = \frac{g\sqrt{A_o}}{{U_o}^2}\frac{(T_o - T_\infty)}{T_o} \qquad \textit{equ. 11}$$

$$K_1 = C_1\sqrt{\frac{4}{\pi}} \qquad \textit{equ. 12}$$

$$K_2 = K_1\sqrt{\frac{1+Pr}{2}} \qquad \textit{equ. 13}$$

Prandtl number

$$Pr = \frac{\upsilon}{\alpha} = \frac{\text{momentum diffusivity}}{\text{thermal diffusivity}} \qquad \textit{equ. 14}$$

Where υ is the momentum diffusivity ($m^2.s^{-1}$) and is defined as the ratio of the viscosity to the density of the fluid, and α is the thermal diffusivity ($m^2.s^{-1}$) which equals to the thermal conductivity divided by density and specific heat capacity at constant pressure of the fluid.

Density difference between the jet and the ambient air induces certain changes in the mean velocity profiles, jet entrainment in addition to the centerline velocity decay. Corrsin and Uberoi [1949] and Sarh [1990] found that the centerline velocity decay occurs more rapidly when the jet has lower density than the ambient air. Taking into account the momentum conservation this rapid decrease in the centerline velocity indicates more mixing and entrainment and so the jet width [Hinze, 1975].

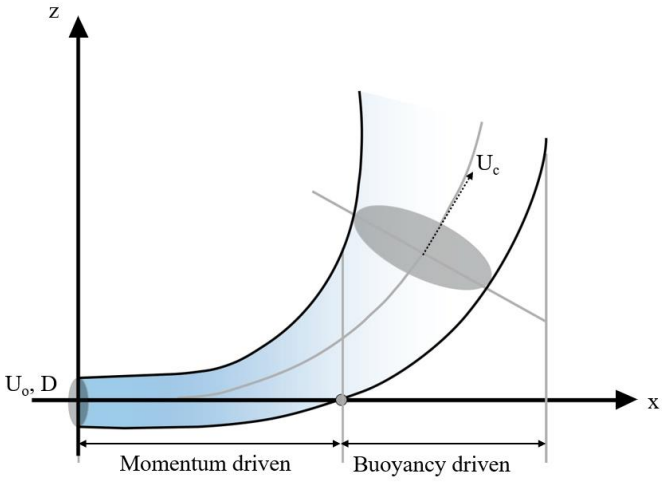

Figure 1.10 : The horizontal buoyant turbulent jet

Horizontal buoyant jet is less frequently studied when compared to vertical jet. In the case of isothermal jet configuration, horizontal jets are similar to vertical jet. However, in the nonisothermal configuration of a hot jet in a cold environment, buoyancy effects drift the horizontal jet upward. Figure 1.*10* shows how a horizontal hot jet propagates into a calm environment. The trajectory of the horizontal buoyant jet depends on the balance between the inertia forces and the buoyancy forces and it is important in the analysis of the jet spreading and the flow field. Based on previous analytical and experimental studies, [Abramovich, 1948], showed that the trajectory of the horizontal buoyant jet can be expressed as [Zhivov et al., 2020]:

$$\frac{z_c(x)}{\sqrt{A_o}} = \psi \frac{K_1}{K_2} Ar_0 \left(\frac{(x + x_o)}{\sqrt{A_o}}\right)^3 \qquad \textit{equ. 15}$$

Where, $z_c(x)$ is the vertical distance of the jet centerline, and ψ varies with the configuration of the jet exit.

1.9 Droplet dynamics

Certain concepts must be defined in order to understand the behavior of particles or droplets released in a turbulent flow, such as human exhalation. The behavior of human exhaled droplets is determined by their size; small droplets (typically less than 5 µm in this field) closely follow

the flow. Meanwhile, large droplets (greater than 100 m) are expected to follow a ballistic trajectory with their inertia acting as the dominant force. The relaxation time can explain how closely a particle follows the surrounding air flow. It is defined as the amount of time it takes a particle to react to changes in fluid flow. The relaxation time for a spherical particle can be expressed as follows

$$\tau_p = \frac{Cu\ \rho_p\ {d_p}^2}{18\ \mu} \qquad \textit{equ. 16}$$

Where ρ_p is the particle density, d_p is the droplet velocity, Cu is the Cunningham factor and μ is the air dynamic viscosity. When τ_p is small, the particle velocity approaches the fluid velocity quickly, causing the particle to respond to the fluid very quickly. On the contrary, when τ_p is large, the particle's velocity changes very slowly. Returning to the exhaled droplets, the particle response time of small droplets is less than that of large droplets. The particle relaxation time, on the other hand, cannot fully explain particle dynamics in fluid flow. A more representative parameter is the particle stokes number which is a dimensionless number given by

$$St = \frac{\tau_p}{\tau_f} \qquad \textit{equ. 17}$$

The numerator of Stoke's number represents the time required by a particle to react to changes in fluid flow, while the denominator represents the time these changes in fluid flow occur. So, if a particle has a stokes number that is significantly lower than one, it means that the particle response time is much smaller than the fluid time scale. As a result, the particle responds almost instantly to any change in the fluid flow velocity. This is the case of smoke particles escaping from a chimney. At the other end of the spectrum, if a particle has a stokes number much greater than one, it does not have time to react to changes in the fluid flow because they occur too quickly. As a result, the particle is not even aware of the fluid's action, and its motion is dominated by inertia and, possibly, mass forces such as gravity. The movement of a cannonball is an example of this situation.

The turbulent fluid flow is well known to have multiple time scales. These time scales span between two extremes, the time scale of the largest eddies, which is the largest possible time scale, is known as the integral time scale. The time scale of the smallest eddies, which is the smallest possible time scale, is known as the Kolmogorov time scale. Each of these time scales could be used to define different stokes numbers corresponding to different physical behaviors. If St is

much greater than one, it means that the particle is only marginally affected by any of the turbulence structures, including the largest ones. Particles with St values less than 1 are strongly influenced by all turbulent structures, including the smallest ones; in practice, they follow the fluid, acting as a passive scalar.

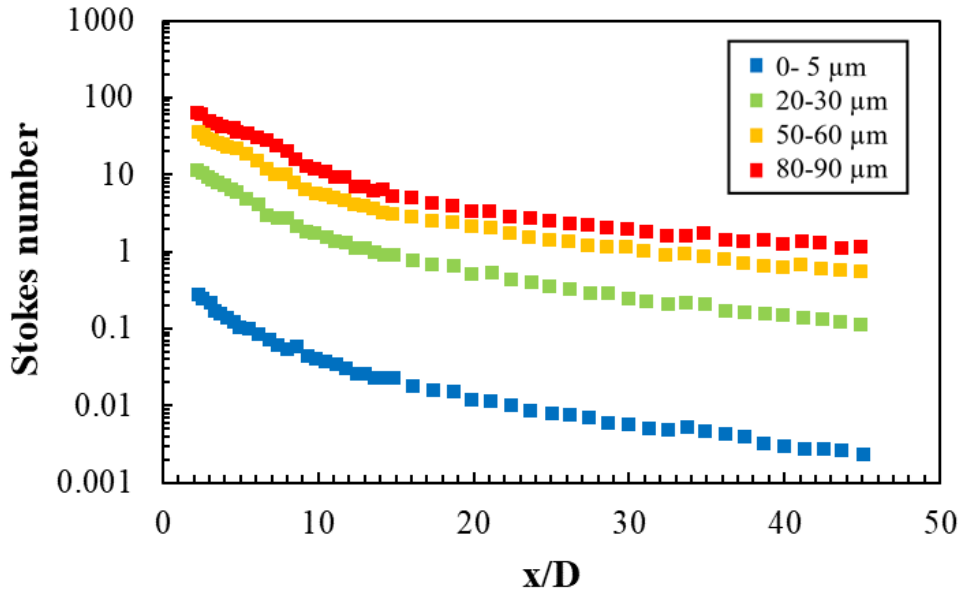

Figure 1.11 : The evolution of Stokes number with distance from the jet inlet for different droplet sizes. [Ferrand et al, 2003]

For different droplet size classes, Ferrand et al. [Ferrand et al, 2003] investigated experimentally, using a Doppler and laser-induced fluorescence technique, the evolution of the Stokes number as a function of distance from the jet orifice. As presented in *Figure 1.11*, for the studied flow configuration, which was vertical and downward jets, the Stokes number decreases along the axis of the jet.

1.10 Summary and conclusions

In this chapter, we presented a literature review on the techniques used to characterize the exhaled droplet and airflow. Some of the measurement techniques used in exhaled droplet measurement involve sampling and transporting droplets from the sampling point to the measurement location. During this transfer, evaporation and/or deposition mechanisms can induce change in the measured droplet size. Thus, these techniques are well suited to measure dry residue size after complete evaporation of the droplets. However, they can also be used to predict the initial droplet

size distribution by applying a calibration process or an evaporation model. On the other hand, non-intrusive techniques allow direct measurement of initial droplet size as well as evaporating droplets at different locations in the jet stream, allowing assessment of evaporation and droplet dispersion.

Our review revealed a lack of quantitative measurements for droplets velocity, in addition to the poverty of the experimental studies on the evaporation of a moving droplet. Phase Doppler anemometry is a technique that is widely used, in other domains, to measure the velocity and diameter of the droplets in a fluid stream. This technique will be applied in this study to characterize both the gas flow field as well as the droplet diameter and size at a different location in the jet stream.

Chapter 2
Experimental study of human-like horizontal jet

This chapter covers the first part of this experimental study which is the characterization of the gas flow. In the first section of this chapter, we justify the main sizing elements used for the design of the experimental bench developed in the context of this study. Then in section 2.2, we describe the experimental procedure using the **L**aser **D**oppler **A**nemometry LDA system to characterize the gas jet velocity field. The characterization of the jet flow field was done in two steps: the study of an isothermal jet flow configuration, followed by the analysis of a buoyant jet configuration. The isothermal jet experiment was used to validate the isothermal turbulent round jet flow model described in section 1.7. Then we developed a transformation procedure for this analytical isothermal model to a buoyant turbulent round jet model that considers the effect of the temperature difference between the air jet and the ambient air. This analytical development is presented in Section 2.3. In this section, we finally present and analyze the results of the experimental campaigns for both isothermal jet and buoyant jet configuration.

2.1 Experimental bench

The experimental bench built for this study is illustrated in *Figure 2.1*. The experimental setup is composed of a jet generation part and an environmental chamber where measurements took place. The jet generation part produces a stable air jet with regulated flowrate and temperature. This air jet enters the environmental chamber through a nozzle fixed on the chamber wall. The measurements were conducted inside the chamber using a two-velocity components Laser Doppler Anemometry and the probes are mounted on 3D motorized axes.

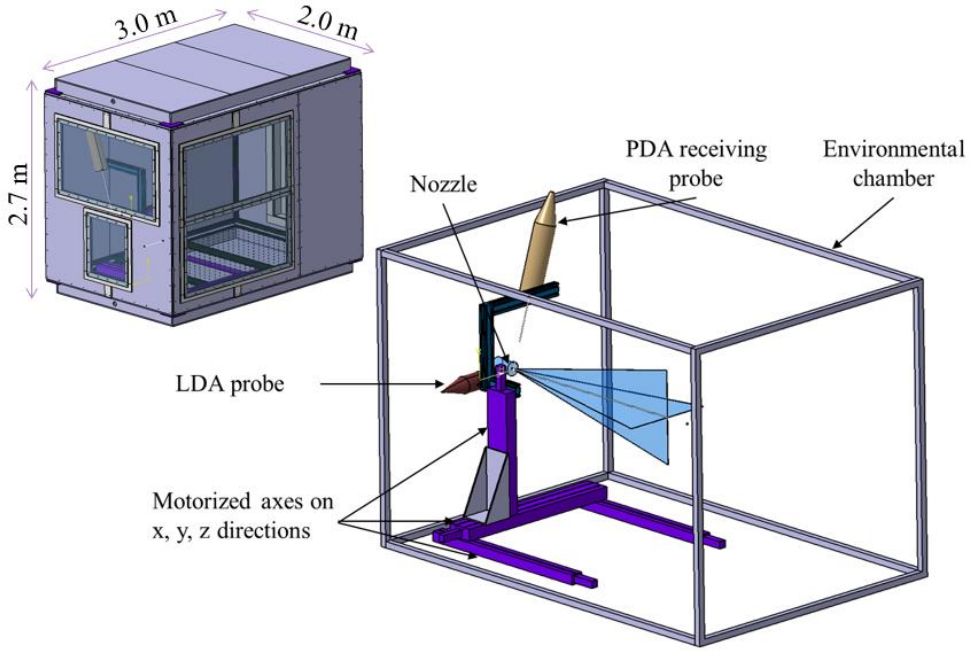

Figure 2.1 : Experimental bench

In this section we will describe the design of the environmental chamber which is based on a numerical investigation for the jet shape and evolution. Then the LDA measurement system is described as well as the seeding particles used as a tracer. Finally, the developed jet generator is presented in section 2.1.4.

2.1.1 Environmental chamber

This study investigates the gas phase and the droplet phase separately, which requires a high stability level in terms of initial conditions and the ambient environment. Therefore, an environmental chamber is designed and built to stabilize the experiment environment. To construct this chamber, we began by selecting dimensions that were appropriate for the lab setting.

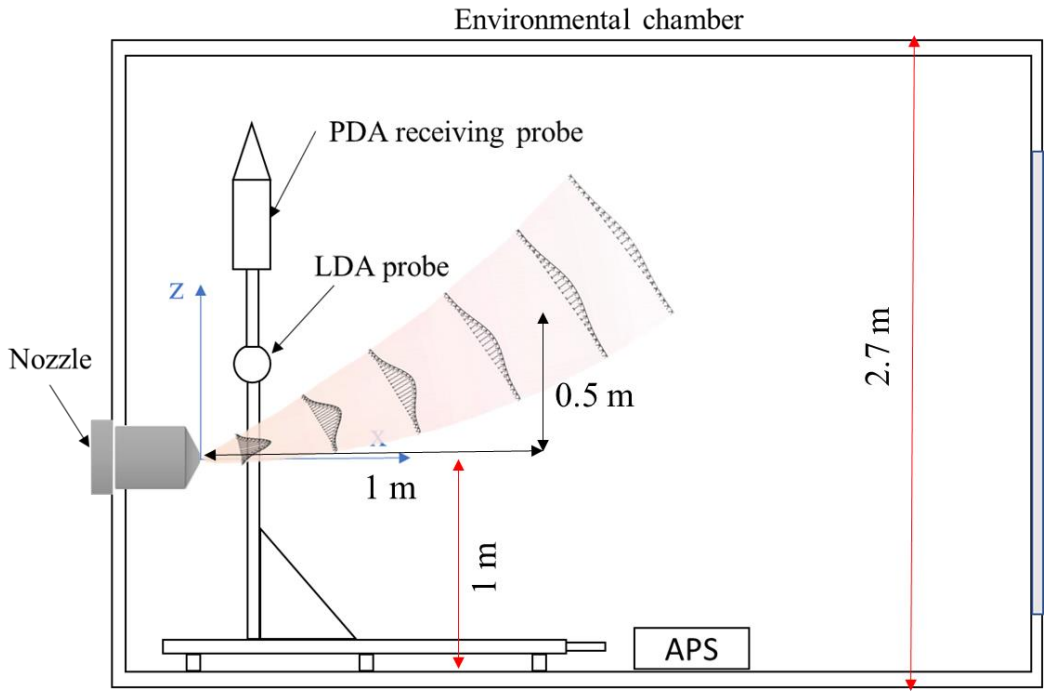

Figure 2.2 : Schematic diagram of experimental setup

The recommended dimensions were 3.0 m in length, 2.0 m in width, and 2.5 m in height. The jet enters the chamber through a nozzle with a 1 cm exit diameter and a 10 cm diameter cylindrical body, as shown in *Figure 2.2*. The point of origin in the following study is specified as the center of the nozzle outlet, which was situated one meter from the chamber floor.

As we are considering a free turbulent round jet in this investigation, the jet confinement effect was a significant aspect of the chamber design. We numerically studied the influence of the chamber dimensions on jet propagation using STAR-CCM+ v2019.2. It is worth mentioning that this experimental bench was built to investigate a jet with initial velocities in the range of 1 $m.s^{-1}$ -breathing velocity- to 10 $m.s^{-1}$, coughing velocity. As a result, we looked into two aspects:

First, the impact of chamber length on the propagation of the jet in the streamwise direction. For this study, we used the jet's highest initial velocity -10 $m.s^{-1}$- because the momentum forces are expected to be more significant in the measurement range, 1 m from the nozzle.

Second, the buoyant jet's shape, taking into account the jet's bending due to buoyancy. As stated in the introduction, the initial temperature of the jet is 34°C, and the chamber temperature is 20 °C, which causes the jet centerline to drift upward. We numerically estimated this drift and tested whether we could measure up to 1 m from the source with the proposed chamber dimensions. For

this investigation, we looked at the lowest initial velocity of 1 $m.s^{-1}$, where buoyancy has the most impact.

We compared three simulations to investigate the effect of chamber length on the jet flow field for the study of confinement in the streamwise direction (x). Table *Table 2:1* shows the boundary conditions applied on the chamber boundaries for the three simulations. The nozzle was fixed to wall A, and the boundary condition at the nozzle outlet was an imposed mass flow (47.1 $L.min^{-1}$) corresponding to the desired average initial velocity (10 $m.s^{-1}$). Because the problem has a symmetry plane in the y-direction, only half of the jet was simulated.

	S-1	S-2	S-3
Chamber dimensions	3.0 m x 2.0 m x 2.5 m	3.0 m x 2.0 m x 2.5 m	5.0 m x 2.0 m x 2.5 m
Boundary A	Wall	Wall	Wall
Boundary B	Constant pressure	Wall	Constant pressure
Boundary C	Wall	Constant pressure	Wall
Boundary D	Wall	Wall	Wall
Boundary E	Wall	Wall	Wall
Boundary F	Wall	Wall	Wall

Table 2:1 The boundary conditions of three simulations performed to investigate the effect of chamber length on jet propagation.

A polyhedral mesh was applied to the domain with a total cell number of more than 1.1×10^5. Reynolds Averaged Navier-Stokes (RANS) equations were used to simulate the airflow field with a k-ω turbulence model for a steady flow.

We present in *Figure 2.3* the velocity magnitude isovalues field in this symmetry plane, for the initial velocity of 10 $m.s^{-1}$. Although in this simulation, the mass flow is calculated to obtain an average axial velocity of 10 $m.s^{-1}$ in the nozzle. Due to the acceleration in the convergent nozzle, a maximum velocity slightly over 12 $m.s^{-1}$ was observed.

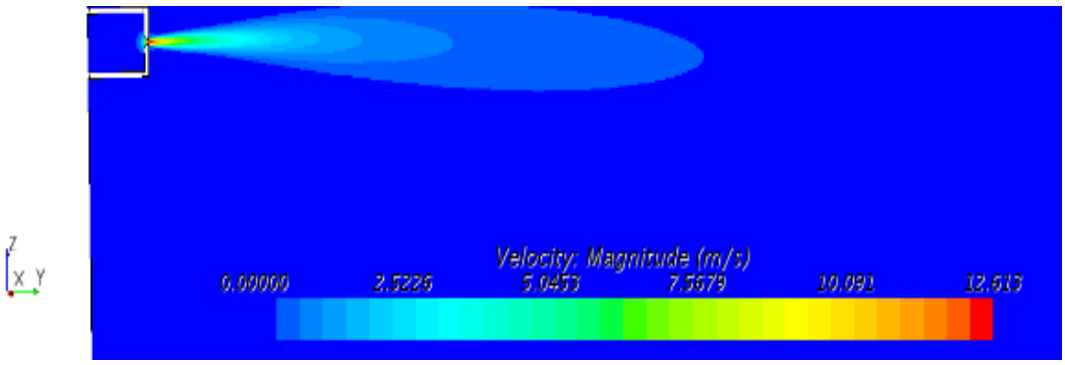

Figure 2.3 The velocity field obtained by CFD with initial jet velocity of 10 m.s^{-1}

To evaluate the effect of the chamber length on jet flow pattern, we plotted the jet axial velocity in the different simulation S-1, S-2, and S-3. These curves are reported in *Figure 2.4* , where the axial velocity on the jet centerline is plotted as a function of the axial position. It should be noted that on these curves, the x=0 position denotes a position inside the accelerating nozzle, where the velocity is 10 m.s^{-1}. As we can see, the axial velocity between 0 m to 2 m from the source remained unaffected by the type of boundary condition applied to the opposite wall. Since this experimental study explores the gas and droplet fields on the first 0.8 m from the source, then the results of the CFD study were satisfactory. These simulation results for the decay of the centerline velocity of the three applied boundary conditions was compared with a physical model presented in chapter 1. This comparison is shown in *Figure 2.4* and we could observe no significant confinement effect on the axial direction.

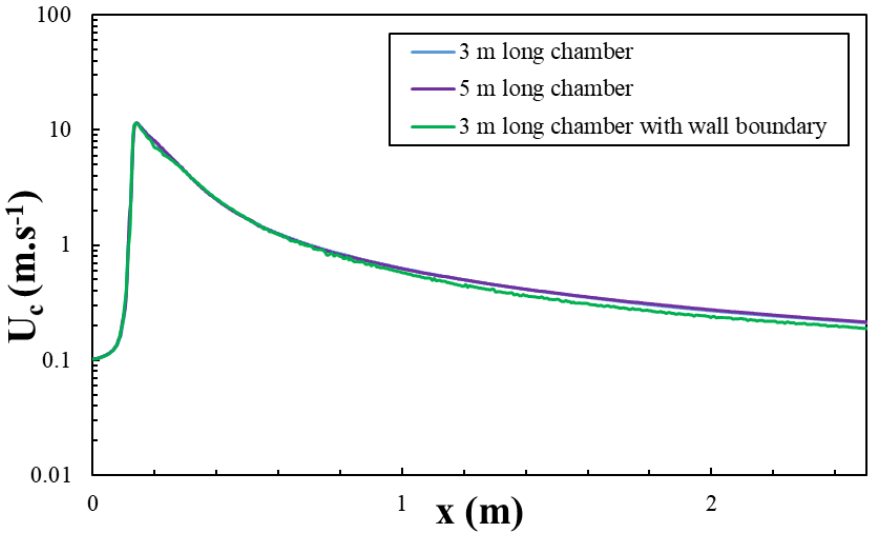

Figure 2.4 The decay of centerline velocity for three boundary conditions with at an initial velocity of 10 m.s^{-1}

In the case of the buoyant jet, the jet shape had to be examined within the studied spatial range. The jet temperature in this simulation is 34 °C, and the ambient temperature is 20 °C. The buoyant jet's diameter expands and its centerline bends upward as it moves into the chamber. Furthermore, studying the evolution of the buoyant jet is critical for positioning the measurement system in relation to the jet exit. We investigated the jet deflection due to the buoyancy effect for an initial velocity of 1 m.s^{-1} considering the above-mentioned temperature difference. Figure 2.4 depicts the simulation result for these flow conditions. At 3 m downstream of the jet opening, the centerline of this jet rises 0.5 m above the jet axis, z=0.5m.

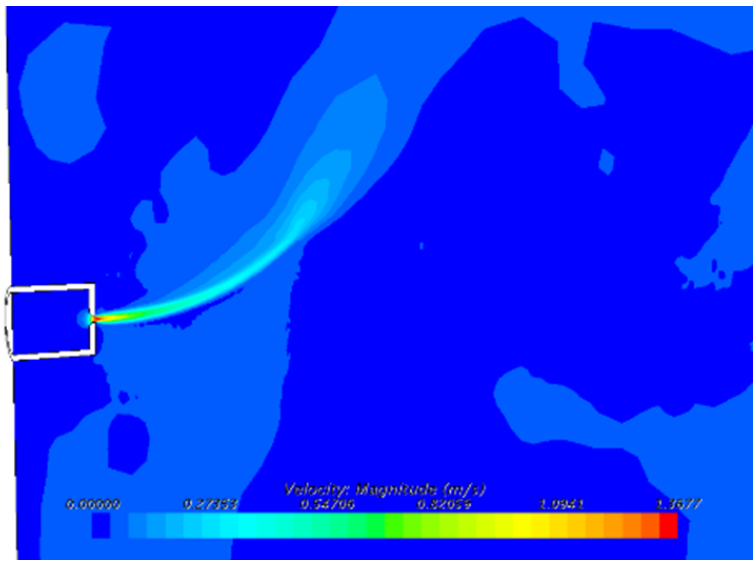

Figure 2.5 The deflection of the jet centerline for jet initial temperature of 34°C, ambient temperature of 20°C, and initial air velocity of 1 m.s-1

Figure 2.6 illustrates the 3m x 2m x 2.7m built chamber based on these findings. After sizing the chamber for the buoyant jet configuration, it was necessary to find a method for controlling the temperature and preventing the chamber temperature from rising during the experiment. The temperature of the chamber was then controlled by a ventilation system.

The ventilation system employed is a classical whole-ceiling whole-floor system designed to fit the above-mentioned chamber dimensions. The supply air is extracted from the lab environment using a suction pump at an average temperature of (20.0 ± 0.2)°C and relative humidity of 40% - 45%. The variable speed suction pump has an air change rate of 3 to 5 times per hour. This air change rate produces a theoretical vertical air velocity of $2.0x10^{-3}$ $m.s^{-1}$ - $3.0x10^{-3}$ $m.s^{-1}$, which is 0.04% - 0.06% of the jet's initial velocity of 5 $m.s^{-1}$. However, when considering the velocity profile at x=0.8m, this value corresponds to 1.2% of the centerline velocity, and slightly more than 12% of the velocity at the jet boundary. As shown in figure 2.5, air is introduced from the lab into the chamber via the ceiling, and it then passes from the floor to the exhaust duct via the vacuum pump.

Despite the theoretical low velocity of the ventilation airflow, the velocity profiles were affected by the ventilation. An exploratory experiment with ventilation showed that the ventilation drifts the jet centerline downward. Moreover, the effect of the ventilation increases as the flow proceeds, and the axial velocity decreases. As a result, no ventilation was applied during the measurements. However, ventilation was only provided between measurements to adjust temperature and evacuate the DEHS droplets. To be more specific, if the chamber temperature exceeds the set point by 0.3 °C, the measurement is halted and the ventilation pump is switched until the chamber temperature is reset.

In addition to temperature regulation, ventilation was required to confine DEHS oil droplets, as DEHS exposure is not recommended. Thus, for safety, the used gas particle tracer (DEHS oil droplets) should be confined inside the environmental chamber, so the chamber walls are sealed, and the chamber is kept at slight negative pressure. The pressure inside the chamber is monitored using a digital differential pressure manometer of 0-30 mbar pressure range.

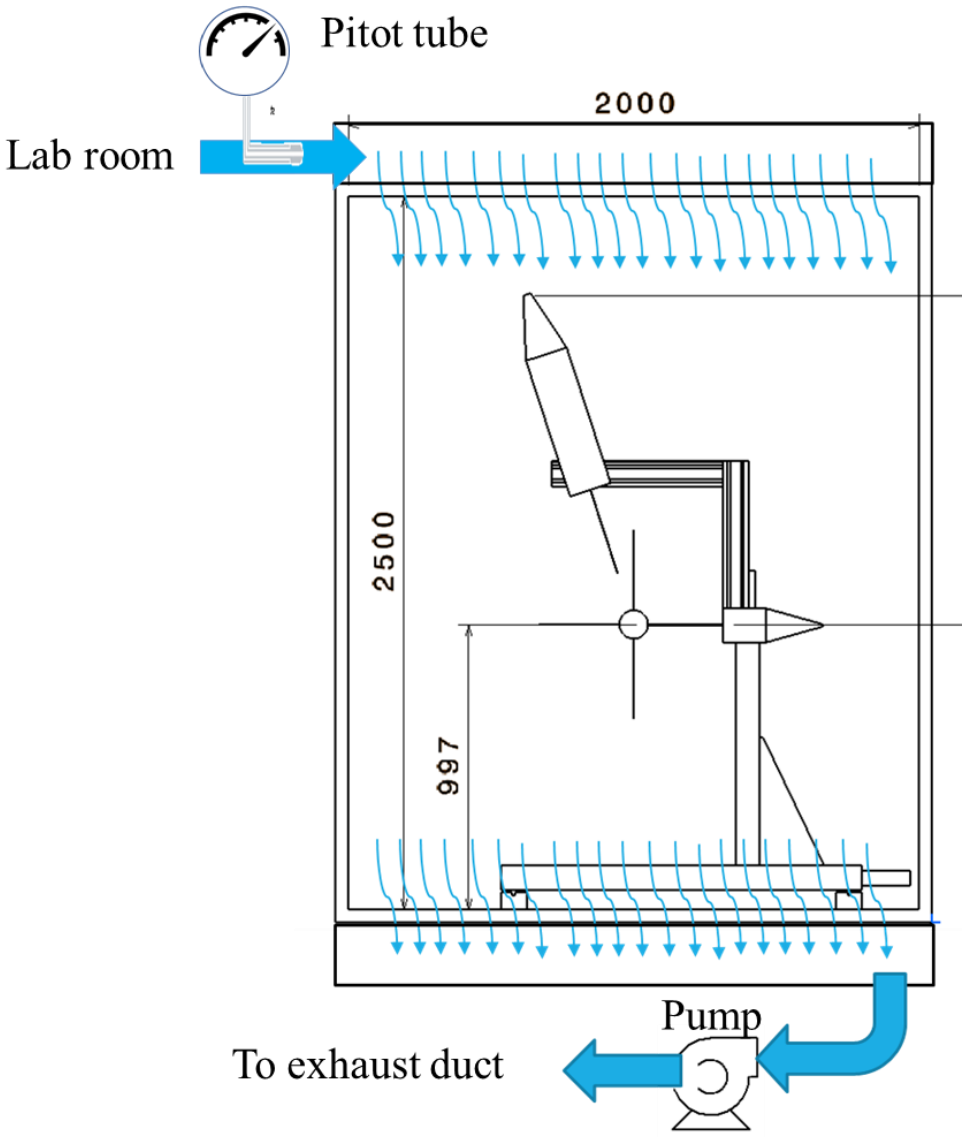

Figure 2.6 The environmental chamber

2.1.2 LDA measurement system

For the measurement of the gas jet axial and radial velocity components, we used a two components LDA (Laser Doppler Anemometry) velocity measurement system. The LDA provides velocity measurement for transparent or semi-transparent particles in fluid flows using blue (with wavelengths of 488 nm) and green (514 nm wavelengths) beams. A 310 mm focus-

length optics - is used for the emitter, forming an LDA measurement volume of 2.9x0.146x0.146 mm^3. A Burst Spectrum Analyzer (BSA) v.4.10, also from Dantec Dynamics, is used to analyze the raw LDA data.

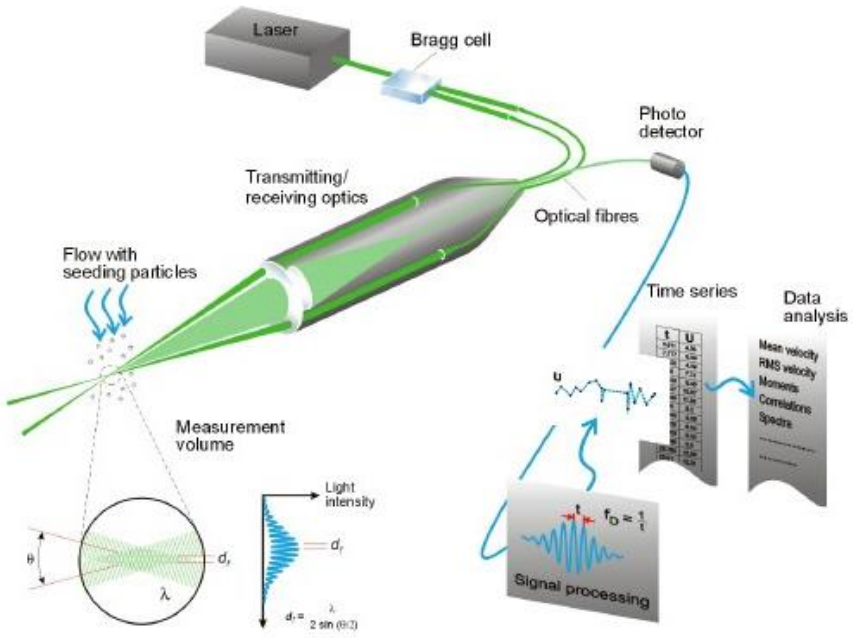

Figure 2.7 The working principle of the Laser Doppler Anemometry [DANTEC, 2020]

The laser source and the receiver are mounted on motorized axes that have a displacement ranges of 1.00 m on x-direction, 0.65 m on y-direction, and 0.61 on z-direction. The control of the motorized axis is remotely conducted by the BSA software from outside the chamber, synchronized with the velocity measurements.

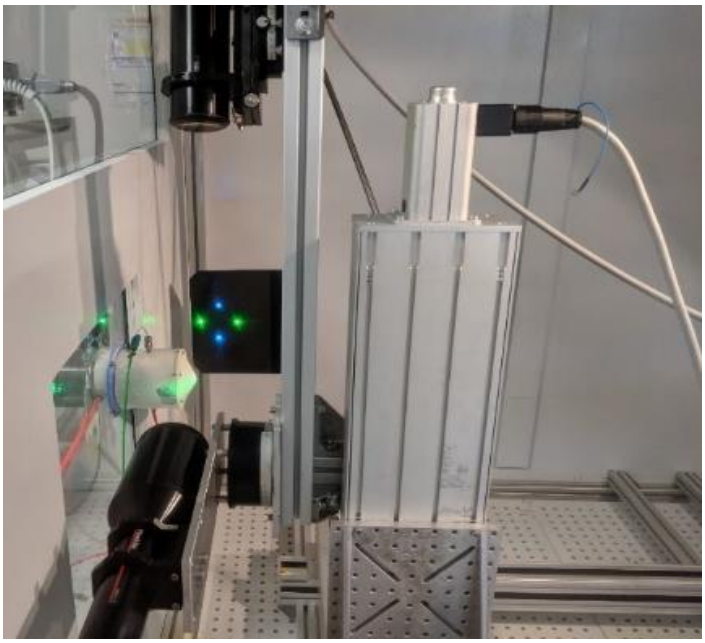

Figure 2.8 The two components Laser Doppler Anemometry system from Dantec

2.1.3 Seeding particles

For the air jet characterization, air is seeded with particles/droplets of a submicronic size. The size of the seeding particles/droplets should be small enough to closely follow the gas, meanwhile, they should be large enough to scatter the laser light and provide good signals. In addition to the particle size, the number of seeding particles is important to produce a good data rate and obtain statistically sound results.

In the generation part, a flow of compressed air passes through a mass flow controller before being injected inside an oil mist generator. In this experiment, Di-Ethyl-Hexyl-Sebacat (DEHS) droplets were used as a gas tracer. The DEHS has a density of 0.9861 g.cm-3 and a Refractive Index of 1.49.

The oil mist generator, shown in *Figure 2.9*, is a vessel composed of two, top and bottom, flanges screwed to a central tube. The vessel is equipped with an electric finned tube radiator fixed on the bottom flange, with an embedded heating cartridge and a thermocouple. The temperature inside the radiator is maintained at a target value using a PI regulator that ensures a stable temperature of the oil in the vessel. The top flange is equipped with feedthrough for a second thermocouple that measures the actual oil temperature close to the Laskin nozzle.

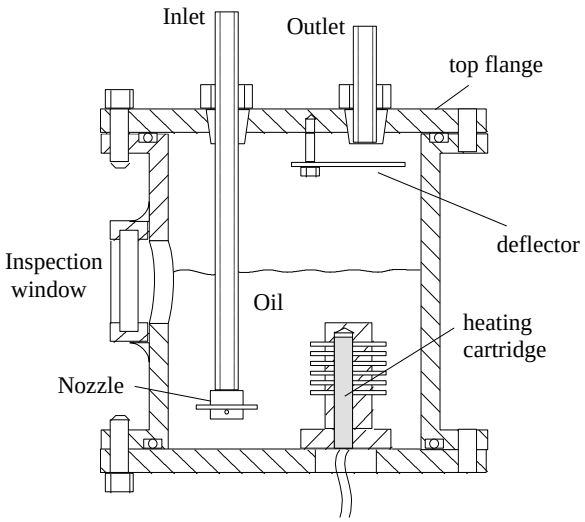

Figure 2.9 The oil mist generator used to seed the jet with DEHS microdroplets.

The air is injected inside the oil vessel through a Laskin nozzle as shown in *Figure 2.10*. The Laskin nozzle produces high-velocity radial air jets. The oil is drawn into the air jets to be atomized by the shear stress induced by the air high velocity. Small oil droplets are trapped into holes air bubbles that raise the surface to burst and release the produced aerosol [Melling, 1997].

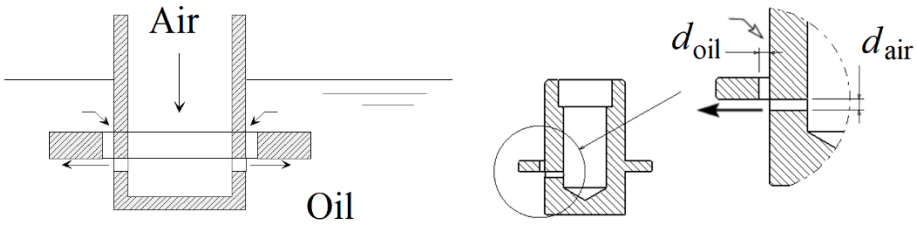

Figure 2.10 : A Cut view of the Laskin nozzle

Figure 2.11 shows Laser-light-sheet visualization taken by Kähler et al. [2002] for the emergence of the air jet from a Laskin nozzle into an DEHS basin and the formation of the fluid cloud.

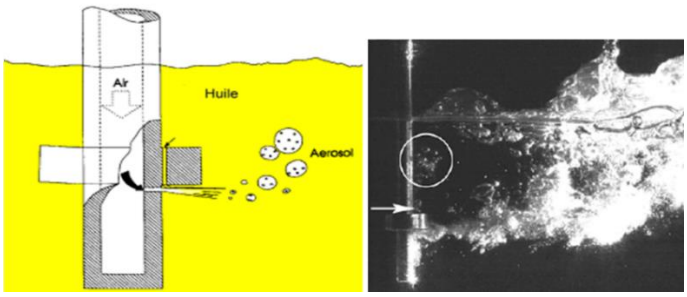

Figure 2.11 : Visualization of aerosol formation by Laskin nozzle [Kähler et al. 2002]

To investigate if the velocity of the DEHS droplets represents the airflow velocity, we analyzed the velocity and the size distribution of 50000 droplets sampled at the center of the nozzle exit. The size distribution of these droplets is shown in *Figure 2.10*. The size of 68.3% of the droplets is <1 µm, and 99.4% of the droplets are ≤ 5 µm.

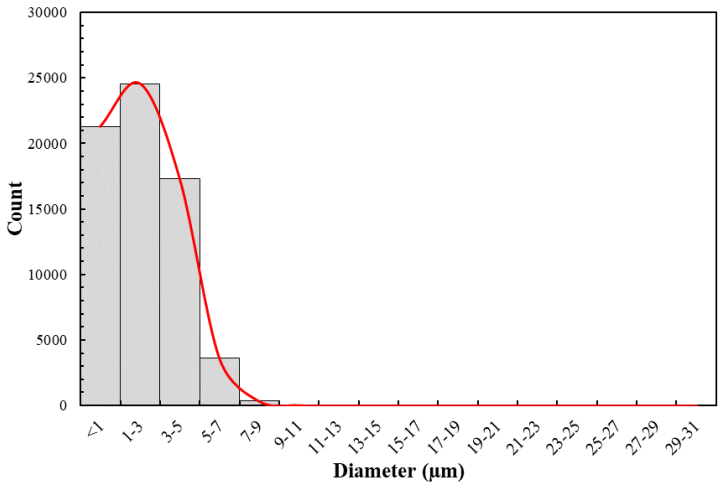

Figure 2.12 : The size distribution of the DEHS droplets produced by the generator at the jet exit (0.003, 0, 0)

The axial and radial velocity of these droplets per their size is illustrated in *Figure 2.11*. The velocity of droplets of less than 7 µm represents 99.99% of the total droplet count. At the jet exit, the mean velocity of the droplets of less than 1µm is only 0.25% more than the mean velocity of

all the droplets measured there. Thus, the droplets generated by the Laskin nozzle are considered to follow the airflow closely.

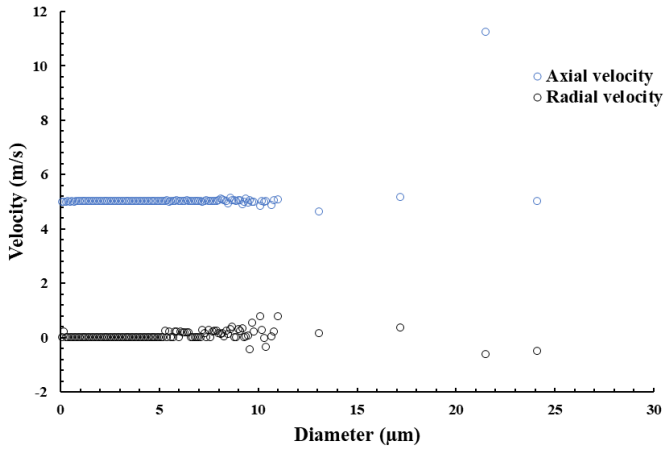

Figure 2.13 : The axial and radial velocity of the generated DEHS droplet at the center of the nozzle exit (0.003, 0, 0)

2.1.4 Jet generation

As shown in *Figure 2.14*, a compressed airflow is regulated using a mass flow controller. After, the flow enters the oil mist generator as explained above where its temperature is adjusted. The DEHS laden air jet passes through the nozzle presented in *Figure 2.15* to enter the environmental chamber.

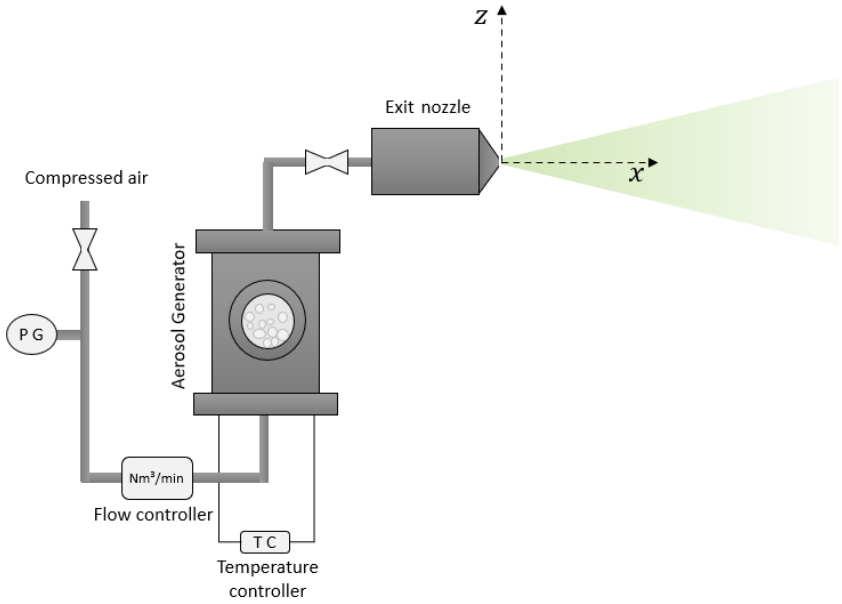

Figure 2.14: The jet generation and the definition of the jet axis

This nozzle is made from a Plexiglas cylinder of 100mm inner diameter screwed to a Teflon conical exit. Because of the angle between the two laser beams constructing the measurement volume, a conical exit was chosen over a straight one. The design of the 120° conical shape nozzle exit plate allows avoiding the intersection between the laser beam and the nozzle body. Hence, this choice of the exit shape allows approaching the nozzle exit as much as possible. In this conical part, a cylindrical exit with 10mm diameter and 10mm length is drilled. The nozzle exit lip was chamfered to minimize a vena contracta phenomenon.

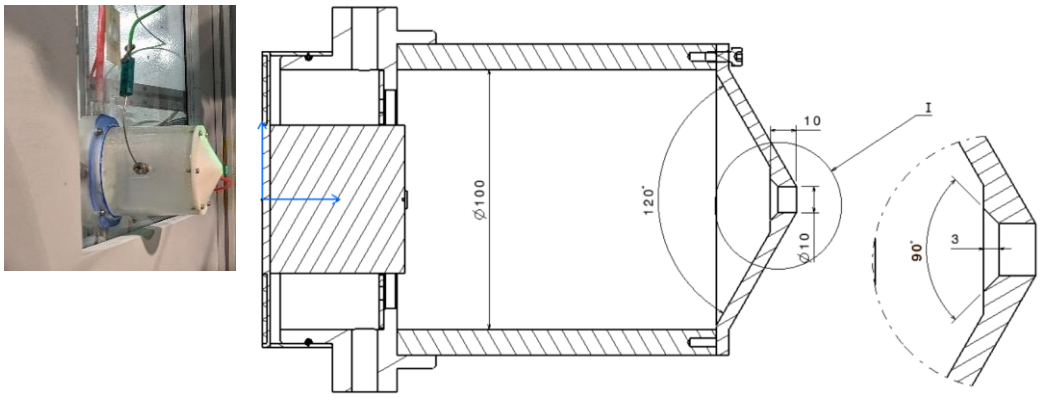

Figure 2.15 The geometry of the jet exit nozzle

The experimental procedure starts with the regulation of the initial jet velocity which depends on the mass flowrate and the temperature of the air. As mentioned before, the regulation of the initial jet velocity was controlled by a mass flow regulator. The setpoint of the mass flow controller is adjusted through direct measurement of the axial velocity at ≈5mm from the jet exit. With the above discussed nozzle configuration, the nearest measurement point to the nozzle exit on the x-axis is about 5mm from the actual exit, as the laser beam would be obstructed by the nozzle geometry.

The flow parameters and nozzle configuration generated a typical "top hat" profile for the mean velocity at the nozzle exit, presented in *Figure 2.16*. The profile is symmetrical around the jet centerline with a diameter of about 12mm, which is 2 mm larger than the nozzle exit since the measurements were done at 5mm from the actual nozzle exit. As the flow generation was stable in this experiment, the maximum of this "top hat" profile was 5 ± 0.05 m.s^{-1} throughout the whole experimental campaign. It is worth mentioning that this velocity corresponds to a jet Reynolds number of 3300.

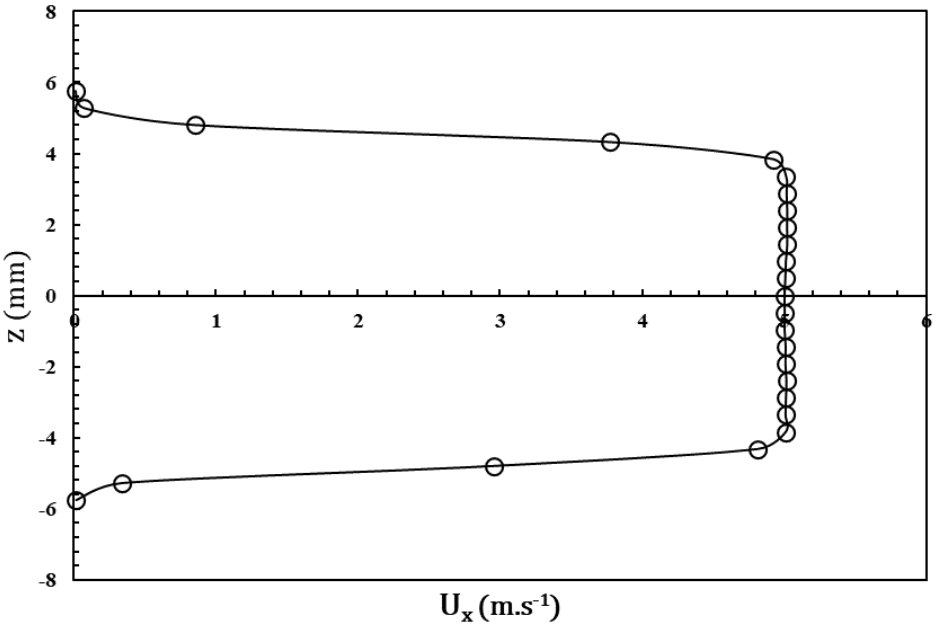

Figure 2.16 The velocity profile at ≈5mm from *the jet exit (0.003, 0 , 0)*

A thermocouple was placed just before the jet exit to measure the jet temperature before entering the environmental chamber. To monitor the temperature inside the chamber, another thermocouple is placed at 2.5 m downstream of the nozzle exit. According to the numerical investigation discussed in section 2.1.1, at this distance from the jet exit, the velocity and the temperature are at the ambient levels.

2.2 Definition of the measurement procedure

In following sections, we will discuss the experimental procedure for the characterization of the jet flow. The used LDA system provides several options for data acquisition, and in section 2.2.1, these options are discussed. In section 2.2.3, the center of the jet is determined with respect to the coordinates of the motorized displacement system. Then the details of the experimental campaigns are provided in section 2.2.4. Finally, in section 2.2, a preliminary experiment is discussed to investigate the appropriate data collection procedure.

2.2.1 Measurement and data acquisition

The LDA system gives instantaneous measurements for two velocity components (U_x, U_z) at a certain measurement point. To measure the velocity at a certain point in a stationary air jet, a sufficient number of the tracer particles should cross the measurement volume to acquire a good

estimation of the averaged velocity and turbulence components at that location. The displacement of the probes and the acquisition process is piloted by Burst Spectrum Analyzer (BSA) software which proposes two kinds of stopping criterion. The stopping criterion means the condition that needs to be satisfied to stop the sampling at the current point and move to the following one. The first stopping criterion is the number of the sampled droplets, which means that after a certain number of samples the system moves to sample at the next programmed measurement point. The second possible criterion is the time duration, in other words, the sampling duration is fixed for the all the measurement points regardless of the number of measured droplets (samples). The number of the sampled droplets at a certain point obtained on a fixed time frame varies depending on the initial data rate and the dilution due to jet expansion. The data rate will decrease when moving on the downstream direction as the concentration of the seeding droplets will decrease with the jet expansion downstream. Similarly, the data rate on the jet center is relatively higher than on the jet borders, near the mixing layer, as the jet expands and ambient air is entrained at the jet borders.

This should be considered when choosing the appropriate number of samples, because near the jet opening the data rate is high and if the number of the sampled droplets is not large enough, the measurement will give instantaneous results meanwhile choosing a very large number of samples will imply longer sampling duration for the points downstream. Thus, a balance should be defined to sample for a sufficient period to have converging measurements near the opening and a reasonable sampling duration downstream.

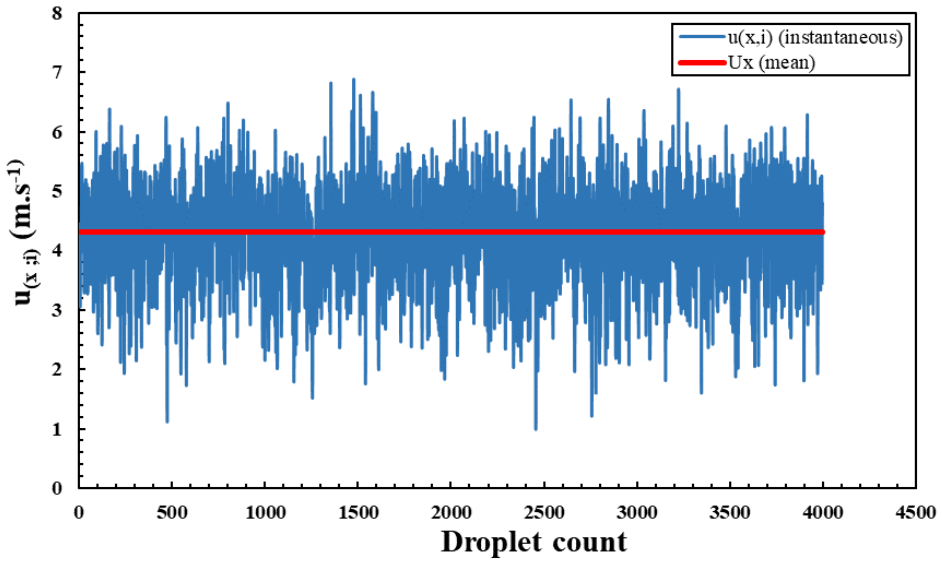

Figure 2.17 Axial velocity along the jet centerline at 0.05m from the source (0.053, 0, 0)

An example of the instantaneous measurement for the axial velocity is shown in *Figure 2.17*. This measurement was on the jet centerline at 0.05 m from the nozzle exit, five times the exit diameter, (50,0,0). The sampling time was 13.5s which was enough to measure the velocity of 4000 droplets. As shown in the figure, the calculated average velocity is 4.3 $m.s^{-1}$ at this point.

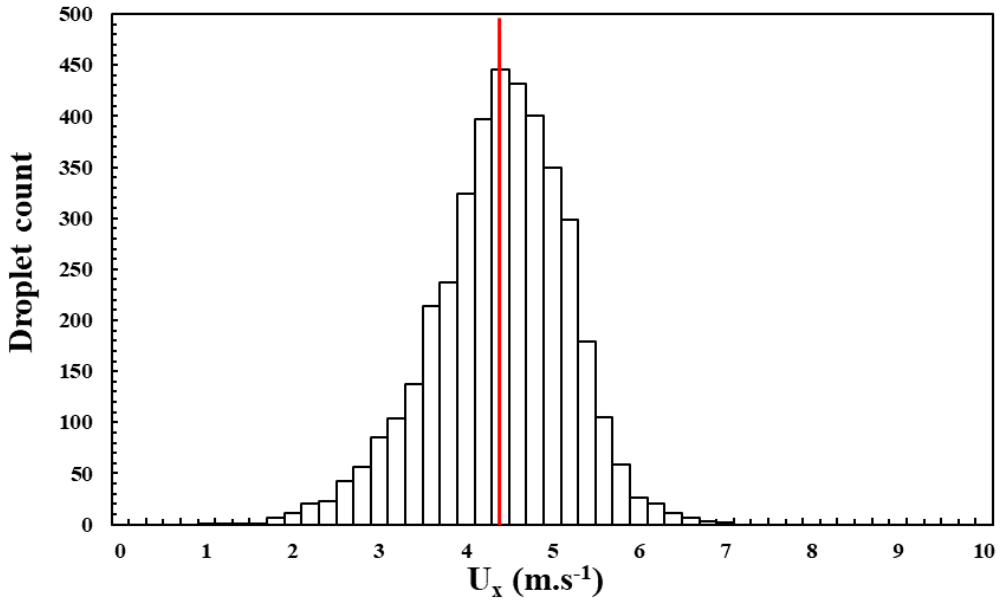

Figure 2.18 Axial velocity distribution on the jet centerline at 0.05m from the source (0.053, 0, 0)

The velocity distribution of the data shown in *Figure 2.17* is presented in *Figure 2.18*. The axial velocity ranges from 1 $m.s^{-1}$ to 6.5 $m.s^{-1}$. However, we can notice from the velocity distribution graph that the distribution is not symmetrical around the average velocity, and this is classical results in jet flow configuration.

2.2.2 Data treatment

The BSA software provides files with information about the instantaneous measurement time, the particle's axial velocity, and radial velocity. These data are exported and then treated using MATLAB to obtain mean values and turbulence intensity.

Taking the example of the measurement presented in *Figure 2.17*. The mean axial velocity is calculated with equ. 18 from the instantaneous LDA data. The mean velocity at a specific location is obtained by finding the average velocity of the droplets passed through the measurement volume during the measurement period.

$$U = \frac{\sum_{i=1}^{N} u_i}{N} \qquad \textit{equ. 18}$$

Where, U is the average velocity, u is *the instantaneous velocity*, N is the total number of the droplets and i is the sample number.

Considering the data shown in *Figure 2.17* and *Figure 2.19*, it is necessary to determine the sufficient number of droplets needed to find the mean velocity at a specific location. Section 2.2.5 is dedicated to answering this question by analyzing the data convergence.

2.2.3 Defining the point of origin (0,0,0)

As discussed before, the jet exits from a fixed nozzle, and its centerline propagates in the x-direction. In this experiment, the measurements were conducted in a vertical x-z plane. To find the symmetry plane around the y-axis, profile measurements were conducted at 10 mm from the nozzle exit. At this distance, the jet is established, and the velocity profiles developed into a parabolic shape (see *Figure 1.7*). With a 0.1 mm displacement-step, the center of the jet, where the maximum velocity occurs, was explored.

2.2.4 Experimental campaigns

In this study, two main experimental campaigns were carried out: one to characterize the isothermal air-jet and another for the buoyant jet. In the following sections, we will detail the parameters of each campaign and the explored region of the flow field. It is important to announce that all the measurements were conducted on the (x, z) plane where y=0.

2.2.4.1 The Isothermal jet campaign:

This campaign involves two experiments: exploration of the centerline velocity decay and velocity profiles measurements. The objective of this experiment is to explore the centerline velocity decay between 0 and 0.8 m from the jet exit. As could be noticed from the previous chapter, the equations of jet velocity profiles proposed by the discussed models are expressed as a function of the centerline velocity.

The nozzle and the locations where the LDA measurements took place are shown in *Figure 2.19*. Close to the nozzle exit, more measurement points are explored to identify the length of the jet core. As discussed before, the transition between the initial jet region and the main jet region is characterized by the decay of the centerline velocity (see section 1.7.1).

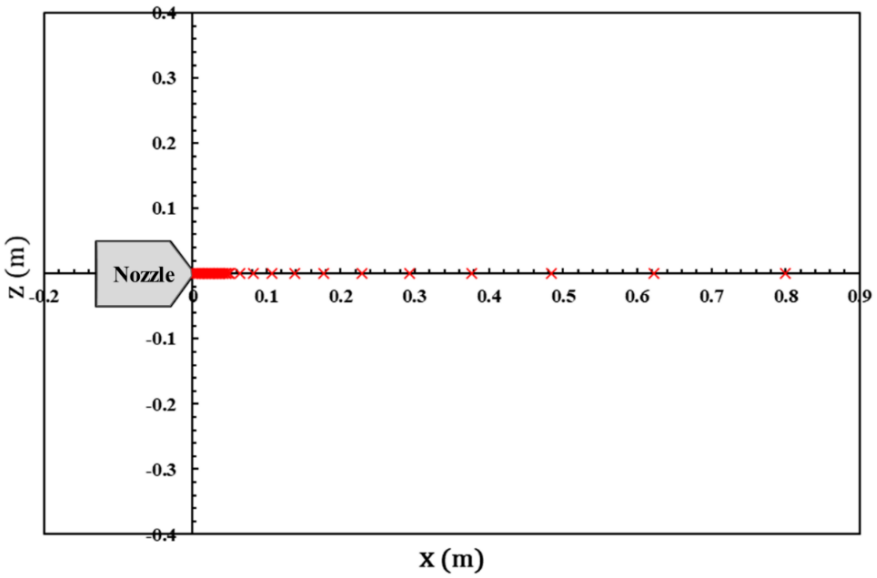

Figure 2.19 The measurement points along the jet centerline

In this experiment of the centerline velocity of the jet, it was chosen to sample 50000 droplets at each point which was sufficient to obtain converged measurement on the two extreme points while optimizing the measurement time.

After exploring the evolution of the centerline velocity decay, the next experiment aims at exploring the mean axial and radial velocity profiles as well as the spread of the jet. Velocity profiles were measured at six distances from the jet opening 0.05 m, 0.1 m, 0.2 m, 0.4 m, 0.6 m, and 0.8 m.

In this experiment, we chose to do measurements near the jet borders, where the velocity is equals the ambient velocity. However, there is a technical constrain, which is the very low data rate near the jet borders. This resulted in prolonged measurement time near the jet borders.

Finally, measurements were conducted within $\varphi = 26°$ which was sufficient to obtain $\frac{U_x}{U_c} < 5\%$ at the jet border. With this angle, 12 points above the centerline and 12 below the centerline were determined to form the measurement grid. In the figure below (*Figure 2.20*), this grid is drawn, and the 25 points forming each of the six-velocity profiles are marked in red.

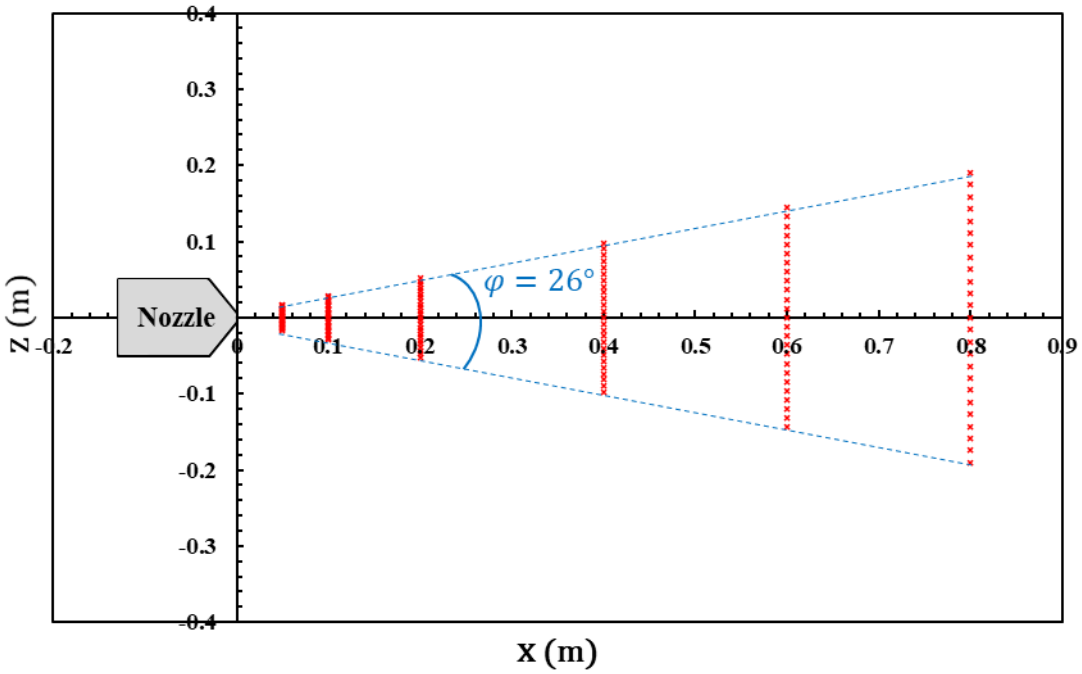

Figure 2.20 The measurement points for the six velocity profiles

2.2.4.2 Buoyant jet campaign:

The temperature of the human exhalation is higher than the ambient temperature in the normal indoor conditions. The temperature of the exhaled air varies with the physical activity and the individual differences between the subjects. However, for people at rest, the exhaled temperature varies also with the ambient conditions. The relationship between the temperature of the exhaled air from the nose and the ambient temperature is studied by Hoppe [Hoppe, 1981]. According to Hoppe, the temperature of the exhaled air is 34°C in ambient conditions of 20 °C, these conditions were used in our experiment to study the buoyancy effect. The density variation due to this temperature difference produces an upward drift of the jet and drives the buoyancy effect.

To determine the upward drift for the jet of this study, 16 profiles were investigated searching for the jet centerline on the measurement range. Due to the large number of measurement points and the longer sampling time near the jet boundaries, only the central part of the profiles is investigated. The explored area covers half of the jet angle, points at 13° degrees around the jet center were measured. The jet centerline was assumed to be located at the maximum mean axial velocity observed in each profile.

After the determination of the jet centerline, six velocity profiles were explored with a similar procedure to the one of the isothermal jet.

2.2.5 Definition of the measurement procedure

When we discussed the data treatment earlier in section 2.2.2, a question appeared about the sufficient number of droplets needed to obtain the mean value of the velocity. In this section, we are trying to answer this question. To answer it, we chose to conduct velocity measurement by sampling 4000 droplets at each measurement point and then study the convergence of the mean axial and radial velocity toward their mean.

The measurement in this convergence study was conducted in the locations shown in *Figure 2.20*. The mean axial velocity values calculated using equ. 18, with N=4000, are presented in *Figure 2.21*. In this figure, the experimental data are marked with hollow circles while the predictions of the model (*equ. 3*) are drawn in solid line.

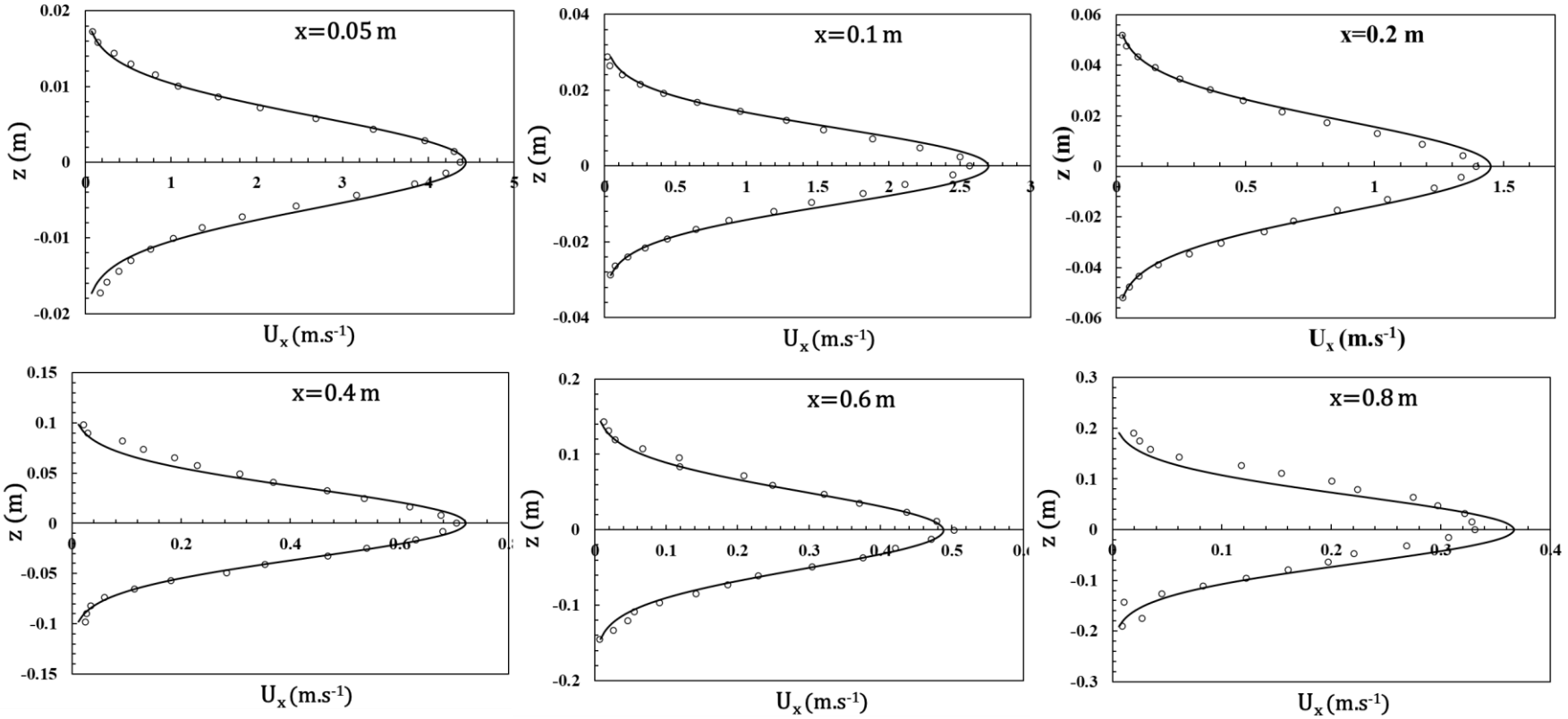

Figure 2.21 The axial velocity profiles at 0.05 m, 0.1 m, 0.2 m, 0.4 m, 0.6 m, and 0.8 m from the exit nozzle.

The centerline velocity decreases from 4.4 m.s^{-1} at 0.05 m from the exit to 0.33 m.s^{-1} at 0.8m. In these figures, the maximum deviation from the model predictions is observed at 0.8m from the source, with a **M**ean **A**bsolute **P**ercentage **D**eviation (MAPD) of 50% which is high compared to the other MAPD values shown in *Table 2:2*. In this table the values of the MAPD for mean axial velocity profiles shown in *Figure 2.21* table are calculated using equ. 19.

Profile distance from the exit (m)	0.05	0.1	0.2	0.4	0.6.	0.8
MAPD (%)	18.8	11.1	7.5	25.1	16.5	50.0

Table 2:2 : *The MAPD values for the mean axial velocity profiles at 0.05 m, 0.1 m, 0.2 m, 0.4 m, 0.6 m, and 0.8 m from the exit nozzle.*

$$MAPD = \frac{1}{n}\sum_{i=1}^{n}\left|\frac{U_{exp} - U_{mod}}{U_{exp}}\right| \qquad \textit{equ. 19}$$

Where n is the number of the measurement points for each profile, U_{exp} is the mean velocity obtained from the experimental measurement and U_{mod} is the mean velocity predicted by the model.

It is noteworthy that the measurement time increases significantly when moving downstream and toward the jet borders. The measurement for the midpoint at 0.05m (0.053, 0, 0) is 13.5s compared to 375.3s at the upper jet border of the 0.8m profile (0.053, 0, 0.017). In the light of this, we can presume that the number of the sampled droplets is not sufficient as the only criterion for data sampling. This is attributable to the fact that the mean velocity value itself at the jet border slightly changes due to some low frequency time oscillations of the jet.

Similarly, the mean radial velocity in the jet is presented in *Figure 2.22*. The experimental measurements are globally similar to the model prediction in their general form; however, a slight underestimation of the maximum vertical velocity can be observed on the first three profiles. This underestimation can be acceptable if we take into consideration the vertical velocity is only 10% of the centerline axial velocity. The other important remark is the increased intensity of discrepancies from the model as we go further downstream. Such discrepancies can be attributed to the fact that the measurement time is longer when compared to changes in the flow structure downstream. The convergence of this data was analyzed to improve the measurement procedure.

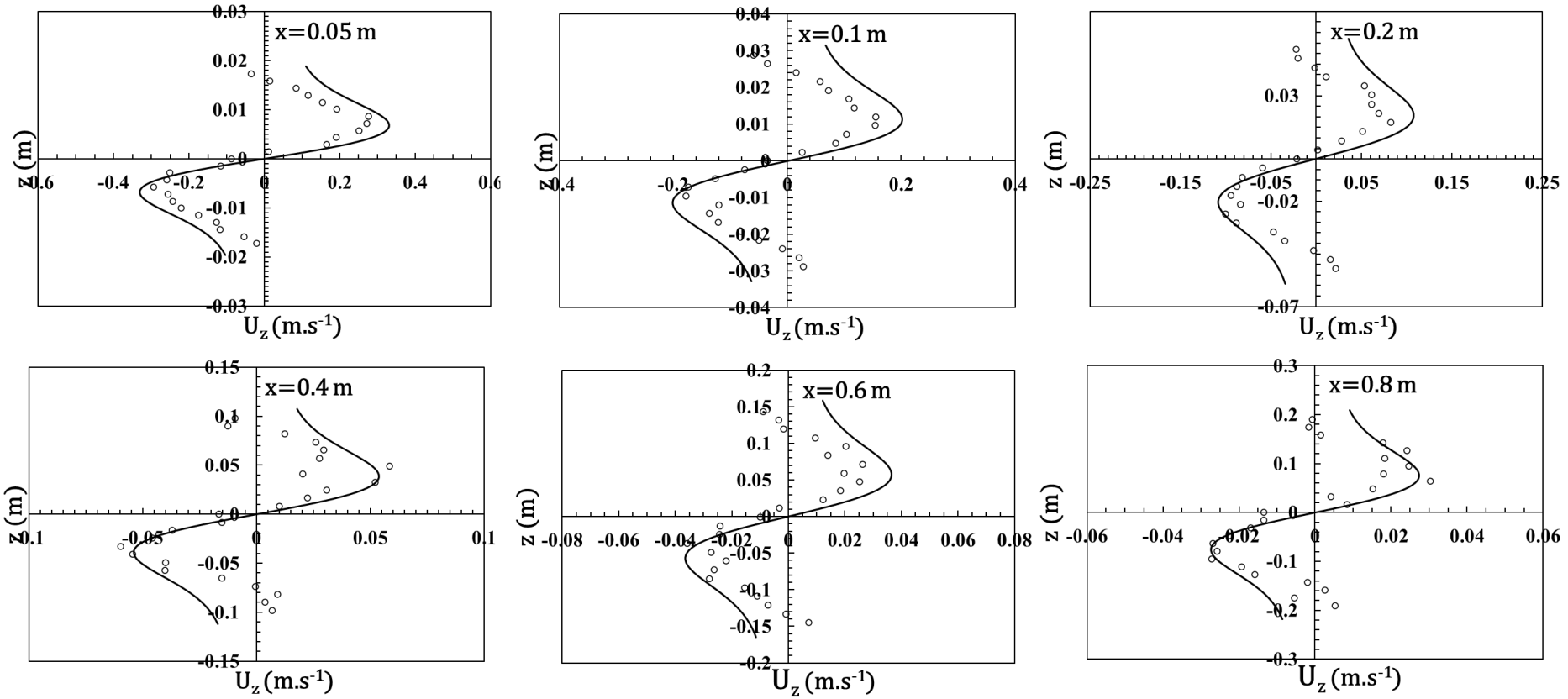

Figure 2.22 The vertical profiles at 0.05 m, 0.1 m, 0.2 m, 0.4 m, 0.6 m, and 0.8 m from the exit nozzle.

The mean axial velocity and radial velocity versus the number of samples used to calculates this mean are shown in *Figure 2.23*. Two points are analyzed in this figure, one at the jet centerline and the other at the jet boundary. The figure illustrates how the average velocities converges on the jet center at a distance of 0.5 m from the jet opening. After 670 samples, the mean axial velocity changes in the range of 1% of its asymptotic value, this number of samples increases to 3700 in the jet borders. This is mainly due to the entrainment of the ambient air near the borders and in many studies appearance of vortices was noticed.

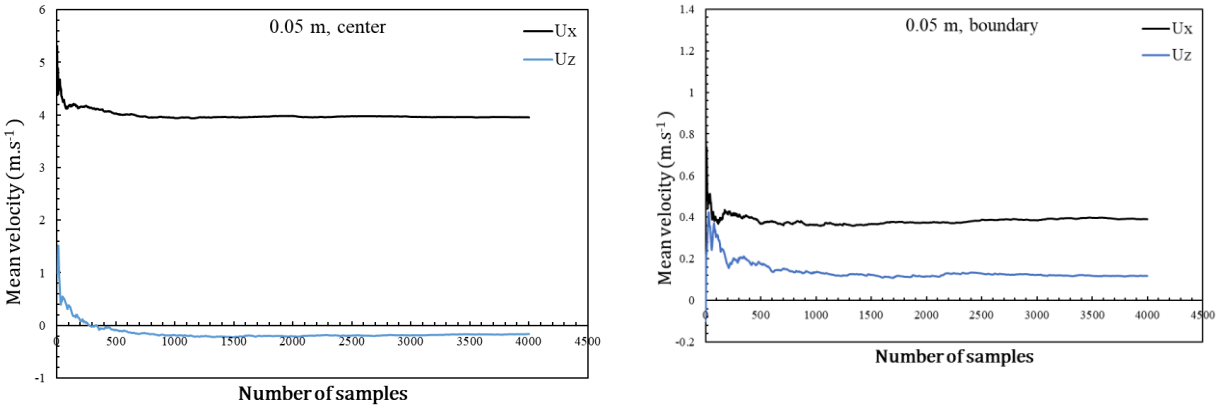

Figure 2.23 change of the average vertical and axial velocity with the number of samples at 0.05m

As shown in *Figure 2.24*, at 0.8m from the jet opening the axial velocity at the center converged to 1% of asymptotic value after 2500 sample. Although it might seem like the radial velocity converges, also, at the jet center of x=0.8m, this is due to the relatively low value of the radial velocity when compared to the axial. In fact, the mean varies in the range of 20%, In addition, no convergence is noticed on the jet boundary at this distance.

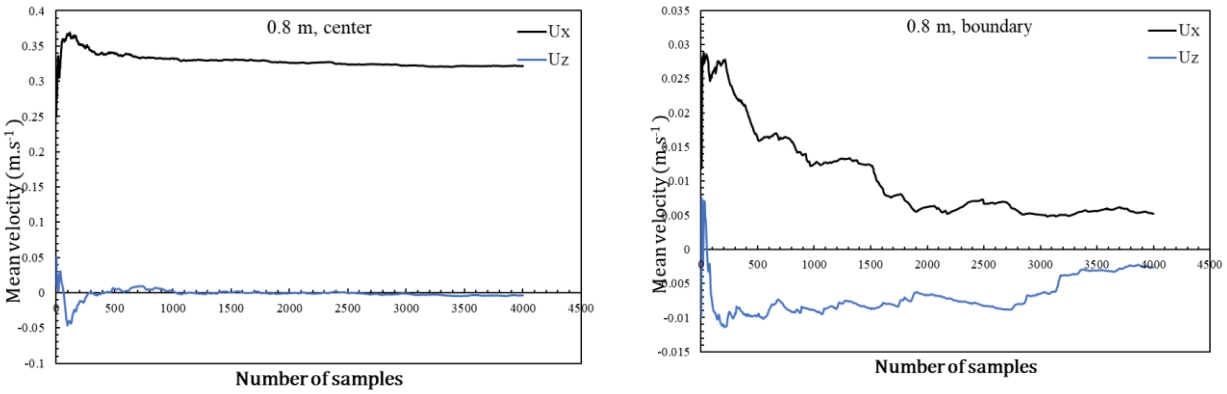

Figure 2.24 change of the average vertical and axial velocity with the number of samples at 0.8m

As discussed above in section 2.2.1 that there are two stopping criteria for the sampling. In the previous section, the number of sampled droplets was chosen as a stopping criterion, 4000 samples, however, this technique shows clear discrepancies on the mean vertical velocity profiles. These discrepancies are proportional to the length of the sampling time, as it increases in the downstream direction. This could be associated with a global change, with time, in the flow structure that is not captured due to the long sampling duration at each point. To address this effect of this flow instabilities, another experimental procedure was performed depending on the sampling duration instead of droplets number. The measurements were conducted for one minute at each point of the 25 points on the profile. Then going back to the first point in the profile the measurements are repeated several times to obtain a reasonable number of sampled droplets. The experiment was repeated 5 times for the profiles at 0.05 m, 0.1 m, 0.2 m, and 0.4 m, due to the limited data rate for the profile at 0.6 m the measurements were repeated 15 times at 0.6m and 20 times for the profile at 0.8m.

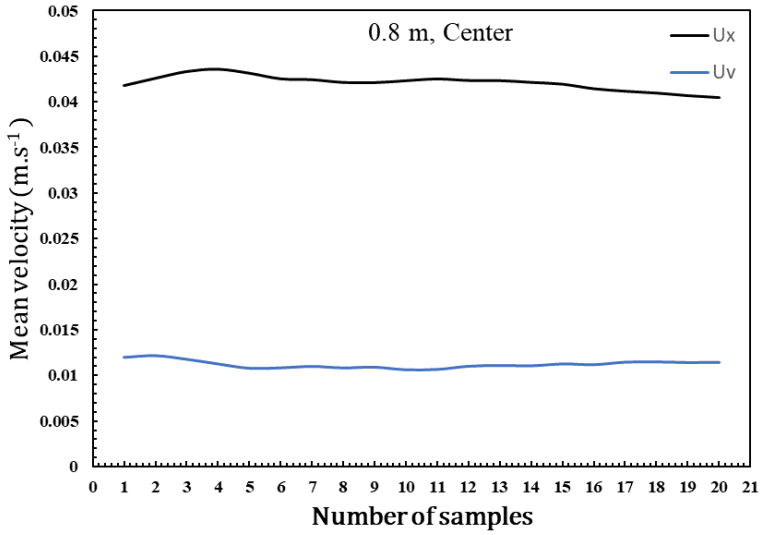

Figure 2.25 change of the average vertical and axial velocity with the number of samples at 0.8m with the improved measurement procedure

Figure 2.25 shows the change of the average velocities with the repetitions of profile measurements. The axial and the radial velocity converge to about 1% of their asymptotic mean after the 17 repetitions. For the following analysis, this procedure is applied for the characterization of both isothermal and buoyant jet, except for the experiment of the decay of the centerline velocity of the isothermal jet. As the data rate near the centerline is high, 50 000 particles were sampled to explore the decay of the centerline velocity of the isothermal jet. The results of these experiments are discussed in the following section.

2.3 Results

In the first part of this section, we present the results obtained from the isothermal jet experiment. This experiment investigates the velocity decay along the jet centerline, and in a second step, it aims at characterizing the flow field in the range of $0<x/D\leq0.8$m. To study the flow field, we analyze the mean axial and radial velocity profiles as well as the turbulence intensity.

Subsequent to the isothermal jet, applying the same analysis, the second part of this section is dedicated to the buoyant jet emitted at an initial temperature of 34°c in an ambient environment of 20°C.

2.3.1 Isothermal jet

Before starting with the analysis of isothermal, the initial conditions of the jet are summarized in *Table 2:3*.

Diameter (D)	10 mm
Velocity (U_o)	5.00 ± 0.05 m.s^{-1}
Reynolds number (Re)	3300
Jet temperature (T_o)	20.0 ± 0.3 °C
Ambient temperature	20.0 ± 0.5 °C

Table 2:3 : *The initial conditions of the isothermal jet.*

To explore the evolution of this flow based on the models represented by *equ. 1*, *equ. 3*, and *equ. 5*. The mean velocity profiles are modeled as the function of the centerline velocity. Hence, the characterization of the jet starts with the definition of the centerline velocity decay. Mainly, determining the decay coefficient and the virtual origin, which is the objective of the next section.

2.3.1.1 Centerline velocity decay

To study the centerline velocity decay, the velocity of 50 000 droplets was recorded at the 37 points previously shown in *Figure 2.19*. At the farthest point from the exit, at x= 0.8 m, the mean axial value changes within a range of 1% after 3500 samples. Accordingly, the 50 000 droplets were sufficient to get a converged value of the mean axial velocity in the spatial range under investigation. The measurement time at the points in the jet core region remained constant, about 1.3 min, while in the main jet region the sampling time increased linearly to reach 29.4 min at x=0.8m.

The maximum magnitude of the axial velocity, at a distance x from the source, is observed at the jet centerline, where the radial velocity tends to zero. Thus, the magnitude of the centerline velocity is obtained by *equ. 20*, considering only the axial velocity component.

$$U_c = \frac{\sum_{i=1}^{N} u_{x,i}}{N} \qquad \textit{equ. 20}$$

Where U_c is the mean centerline velocity, N=50 000, and $u_{x,i}$ is the axial instantaneous velocity measured by the LDA system.

The change of the centerline velocity U_c registered along the jet centerline is presented in *Figure 2.26*. In this figure, the experimental data are shown with the red squares whereas the black line represents the velocity decay predicted by *equ. 1*. Two distinct flow regions are apparent in the experimental data; primarily, the jet core at x/D<6.2, where a slight decay of 4% from the initial velocity is observed. Secondly, the main jet region, at x/D>6.2, where the decay of the centerline velocity could be described by the model. The centerline velocity of the flow decreases from 5 m.s^{-1} near the jet exit to 0.3 m.s^{-1} at 0.8 m from the source.

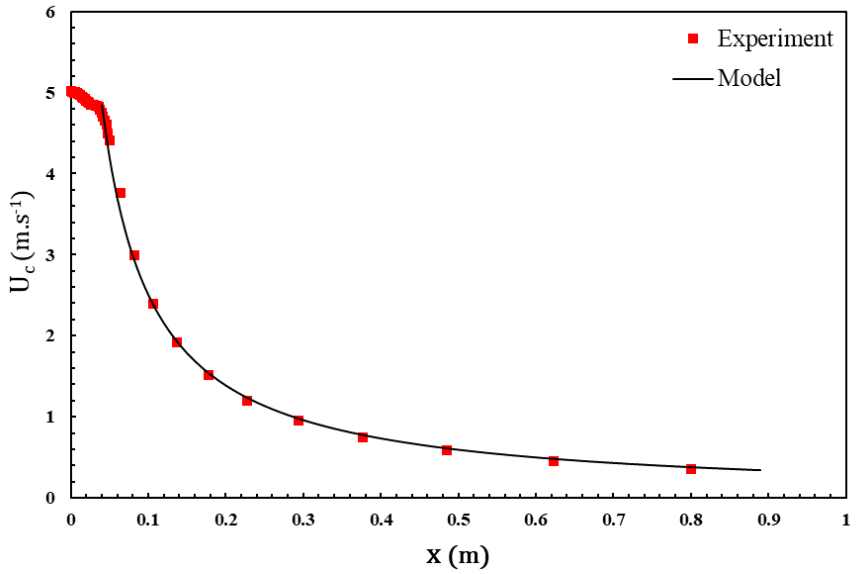

Figure 2.26 The decay of centerline velocity at an initial velocity of 5 m.s^{-1}

equ. 1 has two values that should be obtained from the experimental data: the entrainment coefficient and the virtual origin. As previously discussed in section 1.7, these values depend on the flow initial conditions; namely, Reynolds number and geometry of the exit nozzle.

The dynamic virtual origin is estimated at 24 mm upstream of the exit, which corresponds to a jet entrainment coefficient of 6.2. With these values, the mean absolute percentage deviation (MAPD) is 3%, which indicates that the model represents the obtained data.

Figure 2.27 compares the dimensionless evolution of the axial centerline velocity obtained on this experiment with the results obtained by Hussein et al. [1994] and Capp and George [1982]. In Hussein experiment turbulent airflow with an initial Reynolds number of 10^5 was introduced into a large room. Both hot-wire anemometry and laser doppler anemometry was applied to

characterize the velocity and turbulence intensity of the jet. The measurements conducted by Hussein et al. are in the same distance range x/D as this experiment and the entrainment coefficient (C) obtained by Hussein et al. using the LDA measurement was ≈ 5.8.

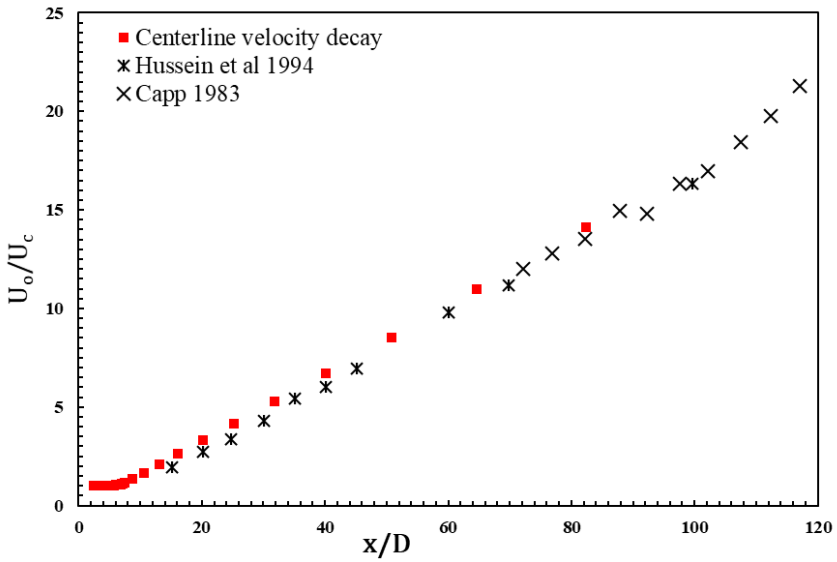

Figure 2.27 The evolution of the centerline velocity with distance from the jet source

2.3.1.2 Mean velocity profiles of the isothermal jet

The results of the optimized measurement procedure developed using the convergence analysis of the mean velocity are presented in this section. Firstly, the mean axial velocity profiles of the isothermal jet are presented in *Figure 2.28*. Generally, the six profiles have similar shape. The centerline velocity at 0.8 m from the exit is less than 10% from its value at 0.05 m, the first measurement point. Meanwhile, the jet width, increases from 34mm to 380mm which indicates that the jet width spread linearly with distance from the source.

Deviation from the model is noticed more near the jet borders as shown in the figure. The highest MAPD is 20% registered for the profile at 0.8 m. This high value is due to the fact that at this distance the mean axial velocity is relatively very low, especially near the jet borders.

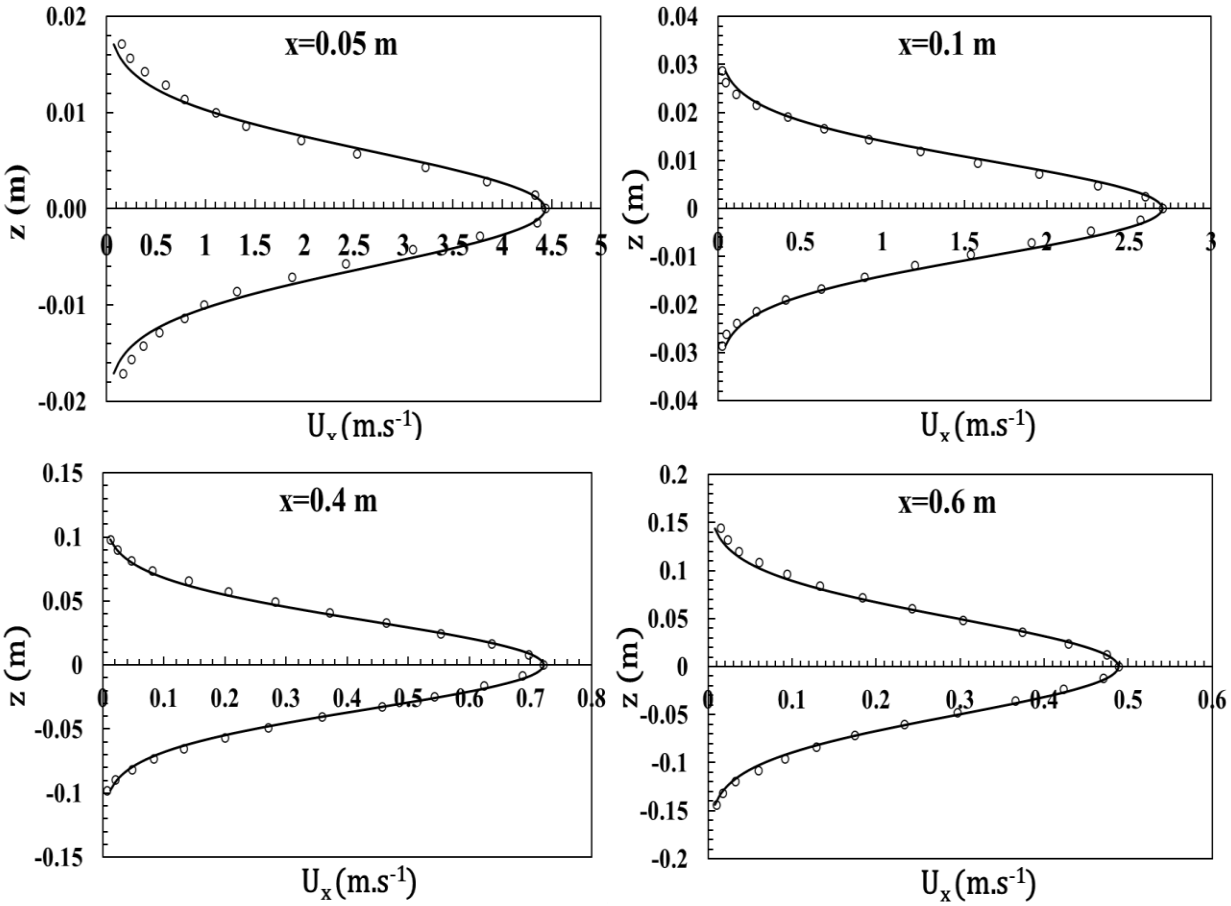

Figure 2.28 The axial velocity profiles at 0.05 m, 0.1 m, 0.2 m, 0.4 m, 0.6 m, and 0.8 m from the exit nozzle.

Further analysis of the axial velocity profiles is present in *Figure 2.29* in the form of normalized velocity profiles. In this graph, the mean axial velocity normalized by the centerline velocity is plotted against the dimensionless radial distance from the centerline normalized by axial distance from the source. The figure compares the results obtained by Hussein et al. [1994] and Wygnanski and Fiedler [1969] with six velocity profiles obtained in the range of $5 \leq x/D \leq 80$.

To interpret this figure, it is important to recall that the plotted model is based on the data acquired in this experiment, of which the decay coefficient is 6.2, and the virtual origin is 2.4D. Whereas in Hussein experiments, the decay coefficient is 5.8, and virtual origin was at 4D.

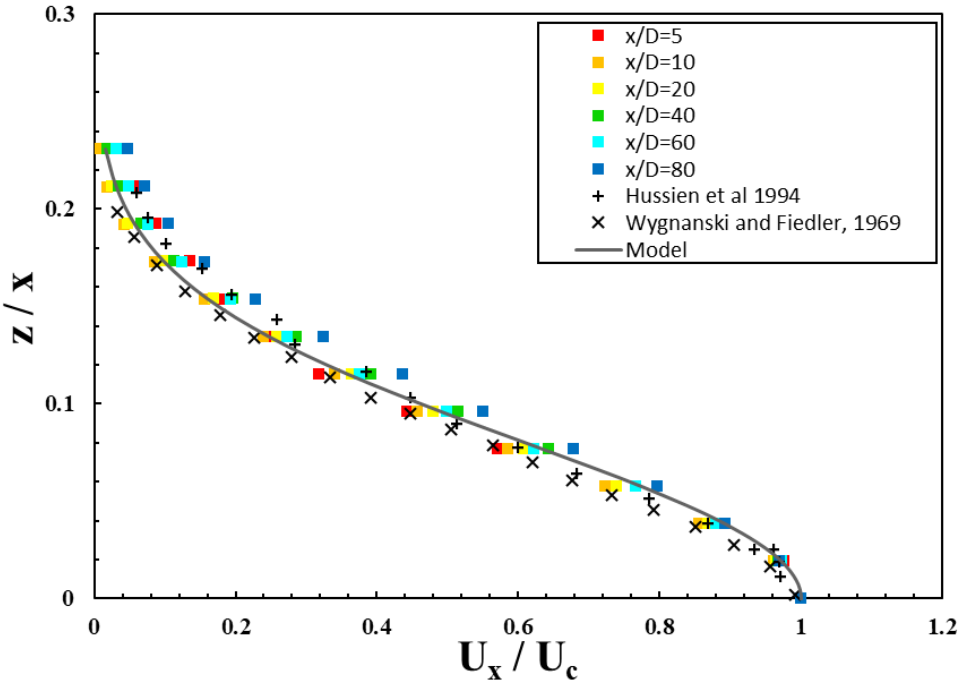

Figure 2.29 The normalized axial velocity profiles and comparison with literature studies

Following the analysis of the axial velocity component, a similar analysis is carried out for the radial component. The mean radial velocity profiles are plotted as a function of the radial distance from the jet center in *Figure 2.30*.

The radial velocity at the jet center is almost zero while the maximum velocity is noticed on inversion points of the upper and lower parts of the s-shaped profiles. The jet expands in the positive jet direction in the upper half of the jet while in the lower half the expansion is on negative direction.

In all the profiles except the one of 0.05 m, the velocity direction changes at the border points. However, this change of direction is not predicted by the model. This change of the velocity direction indicates that instead of the outward expansion of the jet, the jet entrains air inside which is also observed in the CFD analysis. Besides the point on jet boundaries, the model predicts the general increase and decrease trend of the mean radial directions.

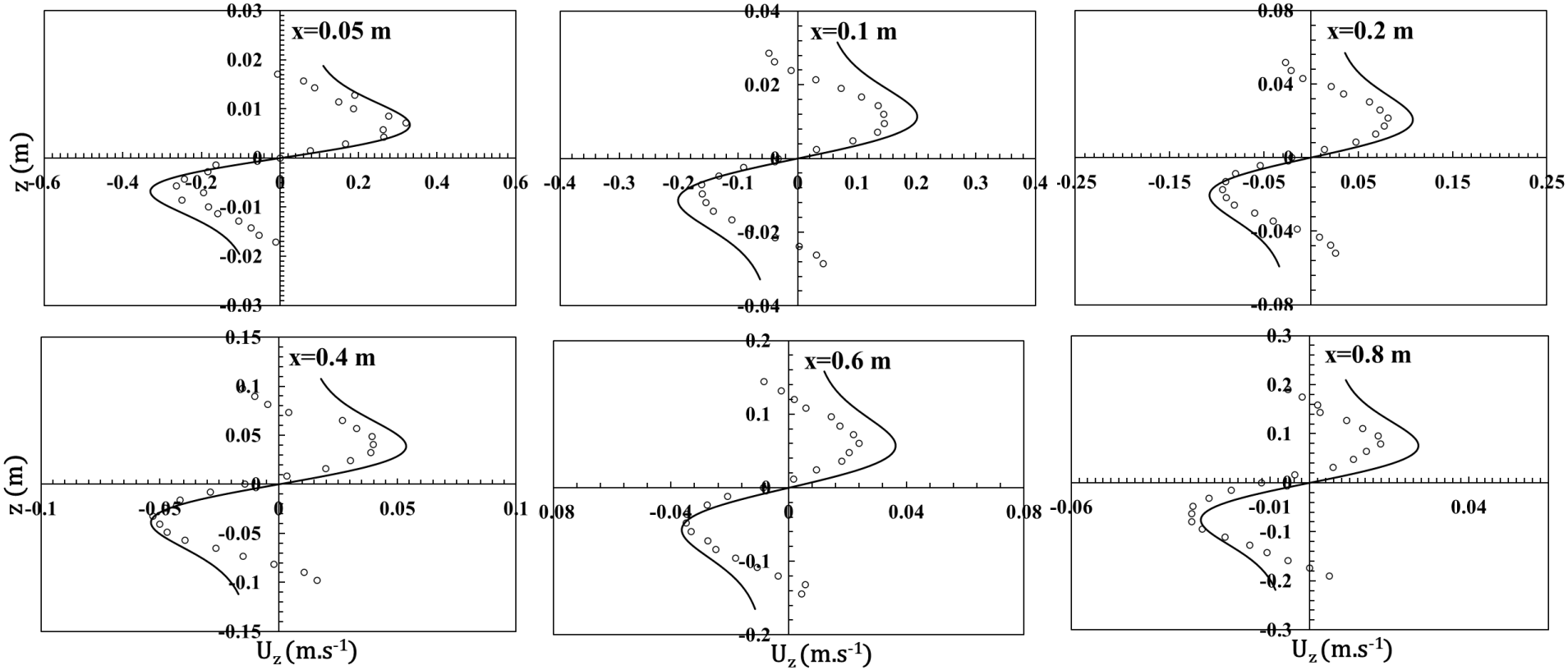

Figure 2.30 The vertical profiles at 0.05 m, 0.1 m, 0.2 m, 0.4 m, 0.6 m, and 0.8 m from the exit nozzle.

The radial velocity profiles normalized by the centerline velocity are illustrated in *Figure 2.31* at dimensionless distances from the jet centerline. In addition, the figure compares these profiles to the experimental data obtained by Falcone and Cataldo [2003]. In Falcone and Cataldo experiment, a water jet with the velocity of 2.4 $m.s^{-1}$ and Re of 27000 was introduced into a non-stratified ambient reservoir where measurements for radial velocity component were conducted up to 40 jet diameters.

The results are less scattered when compared to those obtained by Falcone. The change of the radial velocity direction near the jet borders is also observed in the Falcone and Cataldo experiment.

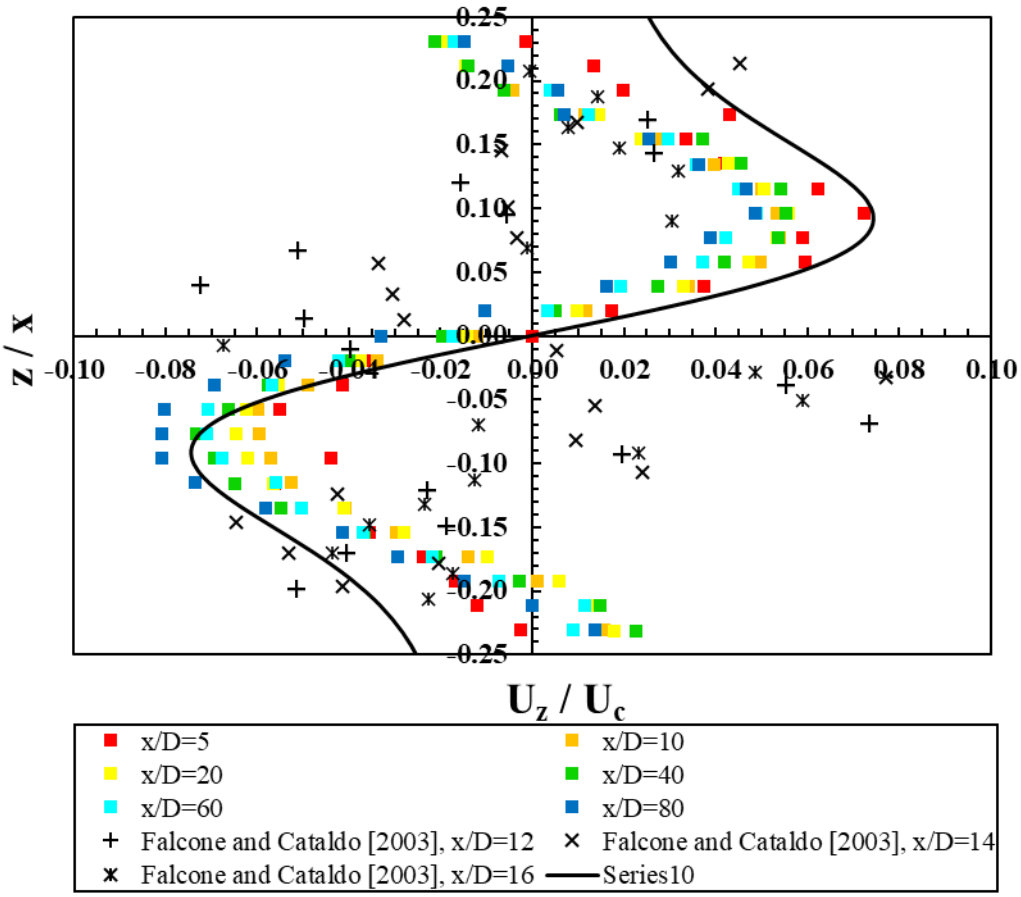

Figure 2.31 The normalized vertical profiles compared to Falcone and Cataldo [2003].

2.3.1.3 The spread angle for the isothermal

In our application, the flow dynamics near the jet boundary are as important as the central region of the jet. The turbulent mixing at the jet borders might induce more evaporation of the droplets when compared to the center of the humid jet. Thus, it is more relevant to define the jet spread by φ^{10} than φ^{50}. As previously explained that the measurement was conducted within an angle of 26° around the jet centerline. With the results presented above, the jet spread angle φ^{10} can be estimated. The angle was obtained by geometrical analysis of the location where the velocity is 10% of the centerline velocity. The result of this geometrical analysis is $\varphi^{10} = 19.7°$.

2.3.1.4 Turbulence

For the following discussion on the turbulence of the isothermal jet, we define the turbulence intensity by equ. 21. In this equation, the turbulence is represented as a function of the axial and radial velocity, assuming that the jet is axisymmetric.

$$Tubulence\ intensity = \frac{\sqrt{\frac{1}{3}\left[\overline{(u_x - U_x)^2} + 2\,\overline{(u_z - U_z)^2}\right]}}{\sqrt{{U_x}^2 + {U_z}^2}} \qquad \textit{equ. 21}$$

Where u_x and u_z are the instantaneous axial and radial velocity, respectively, and U_x and U_z are the mean values of these velocities at location (x, z). In this definition of turbulence, we assume that the velocity fluctuation in the tangential direction is of the same order of magnitude as the radial velocity. However, as the flow is axisymmetric the mean tangential velocity tends to zero.

The turbulence intensity, calculated for the velocity profiles previously presented in *Figure 2.28* and *Figure 2.30*, is illustrated in *Figure 2.32*. In the figure, the turbulence intensity is plotted against the radial distance from the jet centerline. The turbulence intensity along the jet centerline approaches its minimum value which is less than 0.25 in all the profiles. Then it increases in the outward direction of the jet which corresponds to relatively higher fluctuation with respect to the average velocity. Except near the jet borders, the turbulence intensity profiles are similar in the six profiles. For the six border points beyond the range of φ^{10}, the turbulence intensity profile is not symmetrical, and its value is relatively higher.

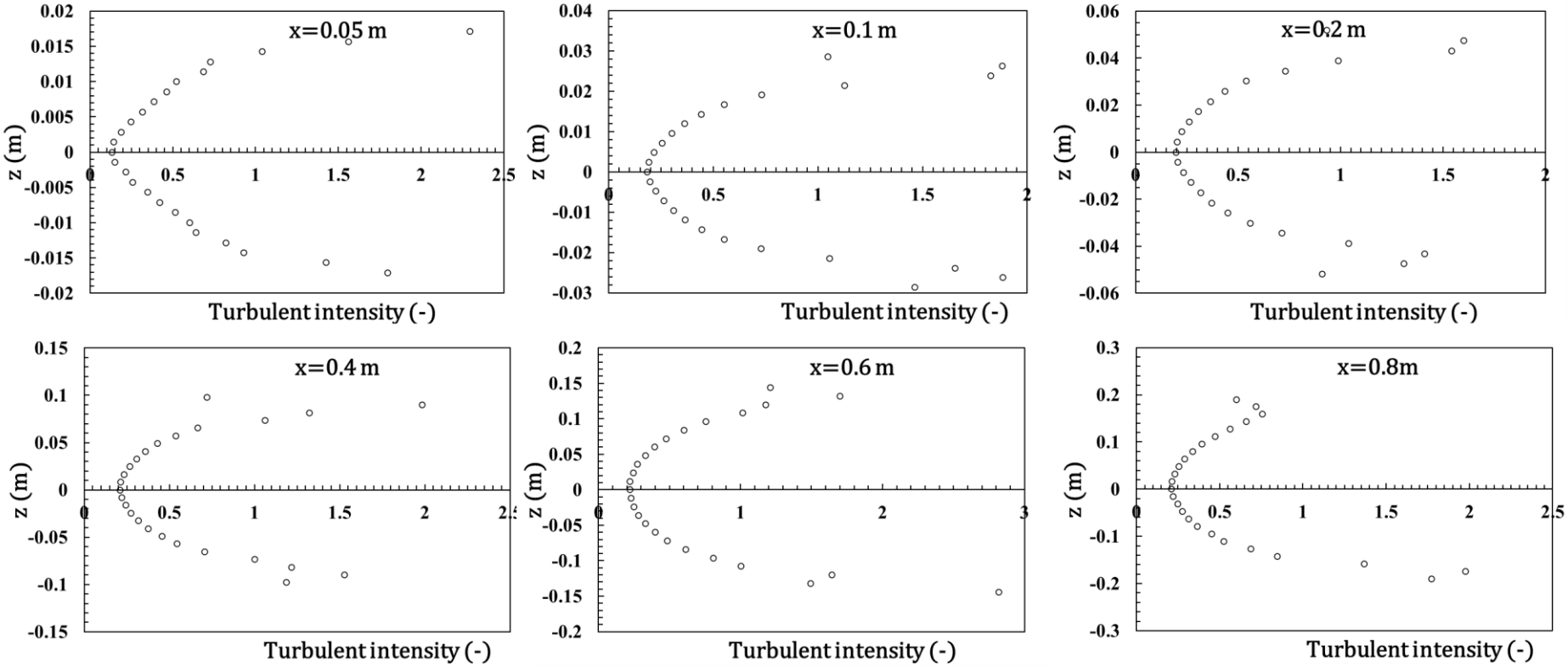

Figure 2.32 The turbulence intensity at 0.05 m, 0.1 m, 0.2 m, 0.4 m, 0.6 m, and 0.8 m from the exit nozzle.

Moreover, the fluctuations of the axial velocity are analyzed in a normalized form. The axial fluctuations are defined by *equ. 22*.

$$\frac{u'_x}{U_c} = \frac{\sqrt{\overline{(u_x - U_x)^2}}}{U_c} \qquad \textit{equ. 22}$$

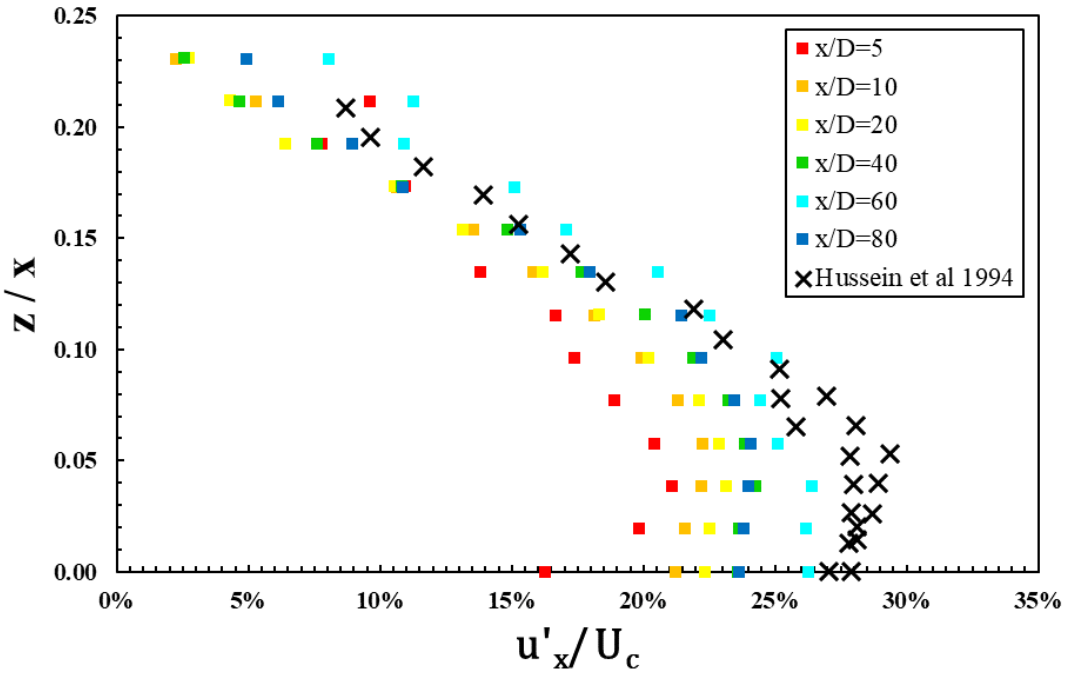

Figure 2.33 The Axial component of the turbulence kinetic energy.

Figure 2.33 shows the percentage of the axial fluctuations for the dimensionless location z/x for a half velocity profile. These data are compared to the results from Hussein et al. [1994]. The percentage of the fluctuations on the jet centerline ranges from 15% to 26% from the centerline velocity, increasing on the downstream direction of the jet. However, these values fall below the value obtained by Hussein et al. [1994] 28% which corresponds to centerline velocity of 4.8 $m.s^{-1}$.

The fluctuations of the radial velocity are examined in the form presented in see *equ. 23*, and compare it with literature data.

$$\frac{u'_z}{U_c} = \frac{\sqrt{\overline{(u_z - U_z)^2}}}{U_c} \qquad \textit{equ. 23}$$

In *Figure 2.34* , the normalized radial fluctuations $\frac{u'_z}{U_c}$ is presented in comparison to the data provided from Falcone and Cataldo [2003]. The figure compares the velocity profiles with the results obtained by Falcone and Cataldo [2003] at x/D equals 8, 10, 12, and 14. It could be noticed that the experimental results overlap even though that Reynolds number in this experiment is 3300 while it was 27 000 for Falcone's free jet. In Falcone experiment, measurements were conducted outside the jet borders to study the jet entrainment. However, in the context of this study, measurements were limited to the main jet region to avoid the extensive measurement time near the jet orders.

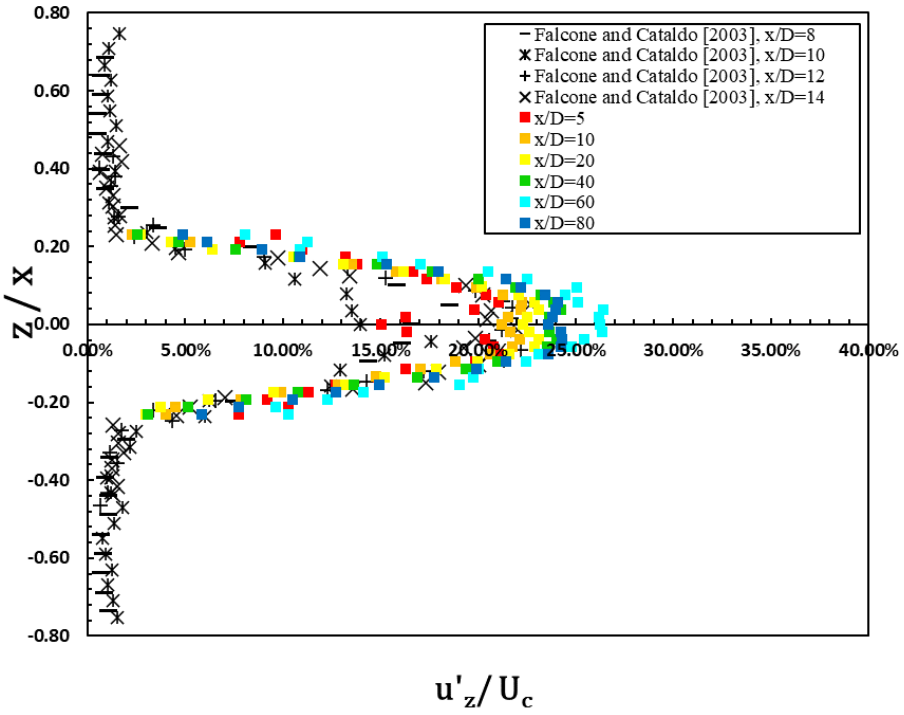

Figure 2.34 The turbulence radial velocity profiles

2.3.2 Buoyant jet

This section presents the result of the buoyant jet experiment. The study of the buoyant jet starts with a definition of the jet deflection due to the buoyancy effect. However, before examining the buoyant jet flow field, it should be considered that the models used to describe the mean velocity profile in section 1.7.2 concern isothermal jets. Therefore, the isothermal jet model is transformed through a process that will be discussed before analyzing the jet velocity decay, the mean velocity, and the turbulence.

2.3.2.1 Buoyant jet centerline

The density change due to the temperature difference between the jet and the ambient air drives the buoyancy effect and drifts the jet upward. The difference between the buoyant jet velocity profiles and the isothermal jet velocity profiles could be explained based on the deflection of the jet centerline. As previously shown, *equ. 15* proposes a correlation between jet thermal and dynamic conditions and upward drift of the jet centerline [Zhivov et al., 2020].

$$\frac{z_c(x)}{\sqrt{A_o}} = \psi \frac{K_1}{K_2} Ar_0 \left(\frac{x}{\sqrt{A_o}}\right)^3 \qquad \textit{equ. 15}$$

Using the equations *equ. 11 - equ. 15* the flow characteristic coefficients shown in Table 2:4 are calculated.

Initial velocity	U_o (m.s^{-1})	5
Initial Temperature	T_o (°C)	34
Ambient Temperature	T_∞ (°C)	20
Initial opening area	A_o (m²)	7.85E-05
Archimedes number	Ar_o	1.51E-04
Prandtl number	Pr	6.99E-01
C		6.20
K1		7.00
K2		6.45

Table 2:4: characteristic coefficients and parameters of the buoyant jet

As described in section 2.2.4.2, 16 profiles were investigated searching for the jet centerline along the distance of 0.8m from the source. *Figure 2.35* shows the maximum values of the axial velocity measured at different distances from the source which forms the centerline of the buoyant jet. The value of the coefficient ψ obtained by the curve fitting is 0.79 with a RMSE of 0.006.

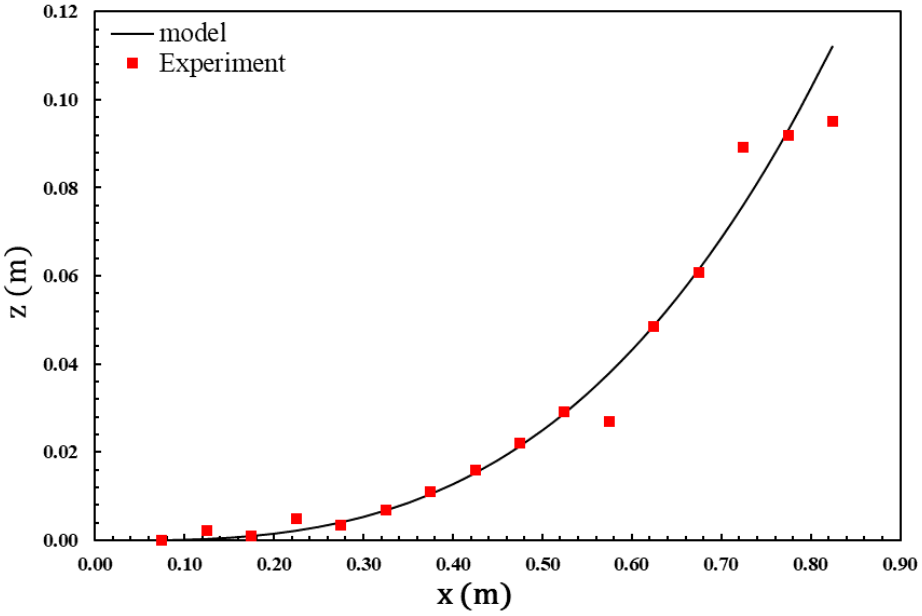

Figure 2.35 : The centerline of the buoyant jet

2.3.2.2 From isothermal to buoyant jet model

To consider the buoyancy effect on the jet propagation, the deflection of the jet centerline should be addressed when calculating the centerline velocity decay and the velocity components. The isothermal jet model discussed in chapter 1 can be reshaped to count for the translation and rotation of the buoyant jet. In other words, the equation of the centerline velocity, axial velocity, and radial velocity mentioned in chapter 1, should be reformulated to take into account the change of the flow direction and the deflection on the jet centerline. The first step after determining the jet centerline is to estimate the corresponding actual deflected distance between the jet opening and the jet opening for a certain point in *x* position. The length of the deflected centerline is illustrated in *Figure 2.36* and is referred to as *s*. Where *s(x)* is the length of the curve at distance *x* from the jet exit, and it can be obtained using *equ. 24*. This length presents the actual distance needed to calculate the velocity decay and the velocity components. So, x is replaced by s the centerline velocity of the flow is shown in *equ. 25*. In *Figure 2.40*-the position where the velocity profiles are calculated is shown in red color.

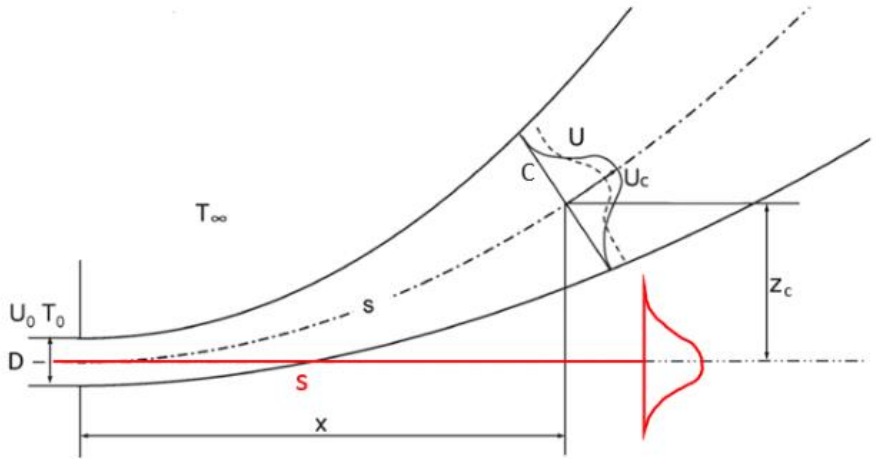

Figure 2.36 The length of the centerline (s) of the buoyant jet

$$s(x) = \int_0^x \sqrt{1 + \left(\frac{dz_c(u)}{dx}\right)^2}\, du \qquad \textit{equ. 24}$$

So, the equation of the centerline velocity decay will be expressed as in *equ. 25*

$$\frac{U_{c\_b}}{U_o} = 6.2\,\left(\frac{s}{D}\right)^{-1} \qquad \textit{equ. 25}$$

Similarly, the axial and radial velocity components could be determined by replacing η by η_b where $\eta_b = \frac{z}{s\beta}$ in *equ. 26* and *equ. 27*.

$$\frac{U_{x\_b}}{U_{c\_b}} = exp(-{\eta_b}^2) \qquad \textit{equ. 26}$$

$$\frac{U_{z\_b}}{U_c} = \frac{\beta}{2\eta_b}\left(-1 + exp(-{\eta_b}^2) - 2{\eta_b}^2\, exp(-{\eta_b}^2)\right) \qquad \textit{equ. 27}$$

The following step after the calculation of the velocity is the rotation of the baseline. The baseline should be rotated by angle θ which the slope of the tangent at point s in the jet.

θ can be expressed as:

$$\theta = \text{atan}\left(\frac{dz_c}{dx}\right) \qquad \textit{equ. 28}$$

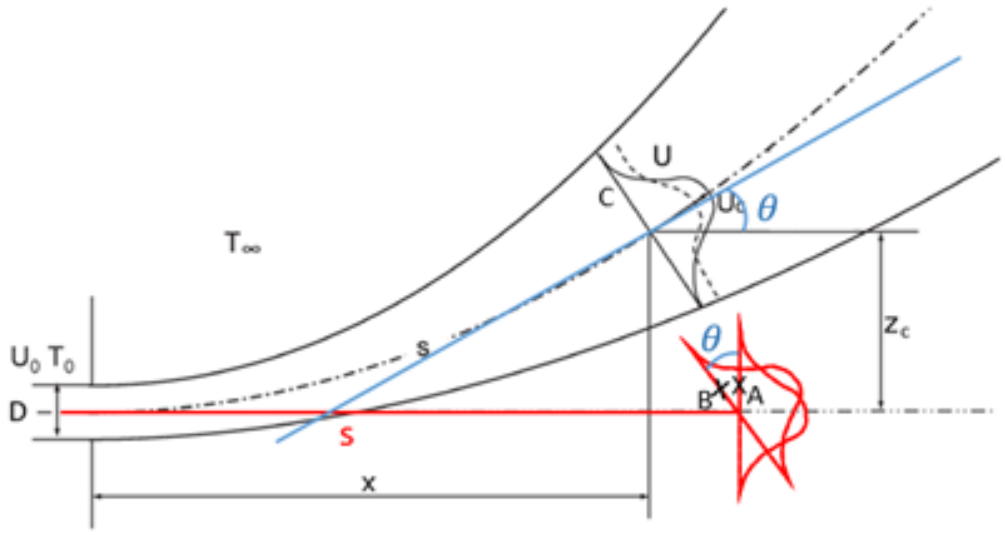

Figure 2.37 The rotating the profile baseline from point A to point B

The baseline rotation from point A to point B, as shown in *Figure 2.37*, and this rotation can be performed following *equ. 29*.

$$\begin{bmatrix} s_B \\ z_B \end{bmatrix} = \begin{bmatrix} 1 & -sin\ (\theta) \\ 0 & cos\ (\theta) \end{bmatrix} \times \begin{bmatrix} s_A \\ z_A \end{bmatrix} \qquad \textit{equ. 29}$$

After, the baseline should be translated from point B to point C, *Figure 2.41*, by applying *equ. 30*

$$\begin{bmatrix} s_C \\ z_C \end{bmatrix} = \begin{bmatrix} s_B + \Delta_x \\ z_B + \Delta_z \end{bmatrix} \qquad \textit{equ. 30}$$

Where $\Delta_x = x - s(x), and\ \Delta_z = z_c(x)$

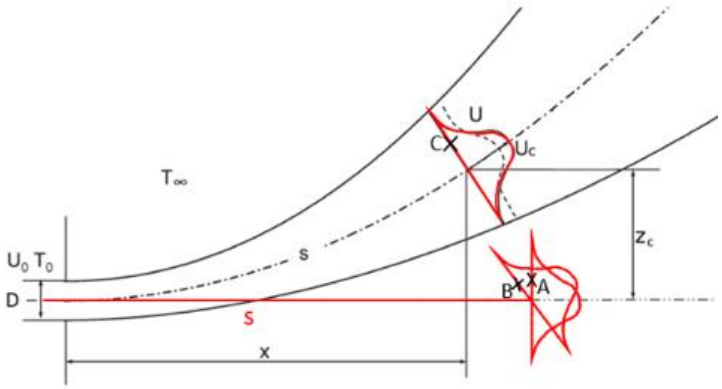

Figure 2.38 The translation of the baseline from point B to point C

The final step is the rotation of the velocity vectors by θ as shown in *Figure 2.39* following *equ. 31*.

$$\begin{bmatrix} U_{xC} \\ U_{zC} \end{bmatrix} = \begin{bmatrix} U_{xB} \\ U_{zB} \end{bmatrix} = \begin{bmatrix} \cos(\theta) & -\sin(\theta) \\ \sin(\theta) & \cos(\theta) \end{bmatrix} \times \begin{bmatrix} U_{xA} \\ U_{zA} \end{bmatrix} \qquad \textit{equ. 31}$$

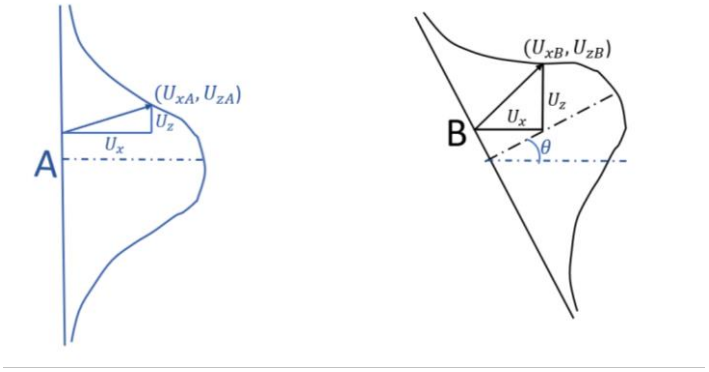

Figure 2.39 The rotation of the velocity vectors in the buoyant jet

Figure 2.40 visualizes the result of using above-described procedure to attain a buoyant jet model. The models predict that at a distance of 0.8 m the centerline of the jet rises about 12 cm.

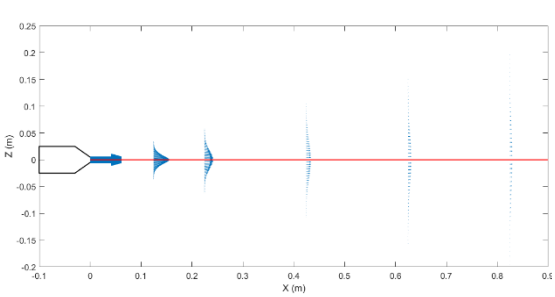

Figure 2.40-a: Isothermal flow velocity profiles

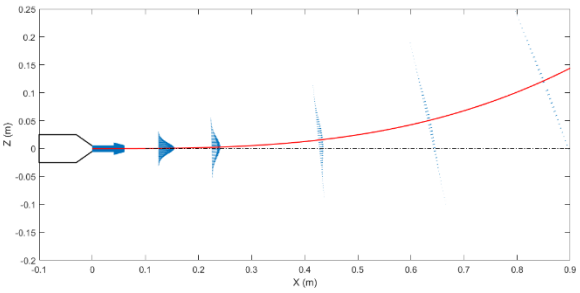

Figure 40-b: Buoyant jet velocity profiles after applying the adopted procedure from isothermal model to buoyant model

2.3.2.3 Centerline velocity decay

The above-described procedure produces velocity profiles that are perpendicular to the upward drifted jet centerline. The deflection angle is a function x, so it is different for each profile. Apply this in constructing the net of the measurement point is complicated and bear uncertainties. To facilitate the experimental procedure, the measurements for each profile were conducted in vertical lines instead of lines perpendicular to the jet centerline. So, numerical interpolation was used to confront the experimental data with the buoyant jet model. Using MATLAB model prediction for the velocity profile was conducted with a fine mesh. Then the mean velocity profiles at the measurement location are calculated numerically.

Figure 2.41 shows the experimentally measured mean centerline velocity in comparison with the values predicted by numerical interpolation of the reshaped buoyant jet model. The MAPD of the experimental data, when compared to the model, was 11.9%. A general trend of error increase with distance from the source was observed, while the maximum error was 20.4% at 0.6 m.

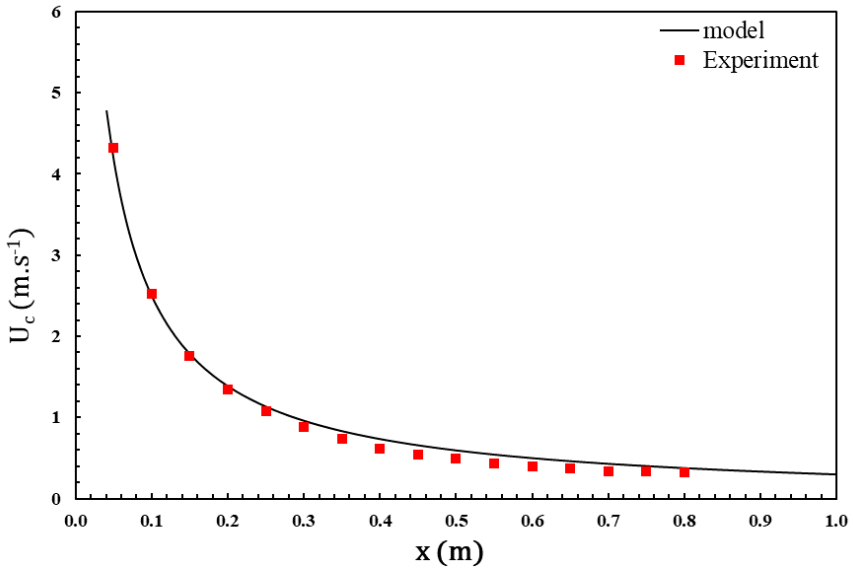

Figure 2.41 The decay of centerline velocity of the buoyant jet

2.3.2.4 Mean velocity profiles

The experimental results of the axial velocity profile of the buoyant jet are presented in *Figure 2.42*. Along with these results, the predictions of the buoyant jet adapted model are plotted at different locations in the jet flow field. Considerable overestimation, about 40% of the actual value, for the centerline deflection is observed at 0.6 m and 0.8 m.

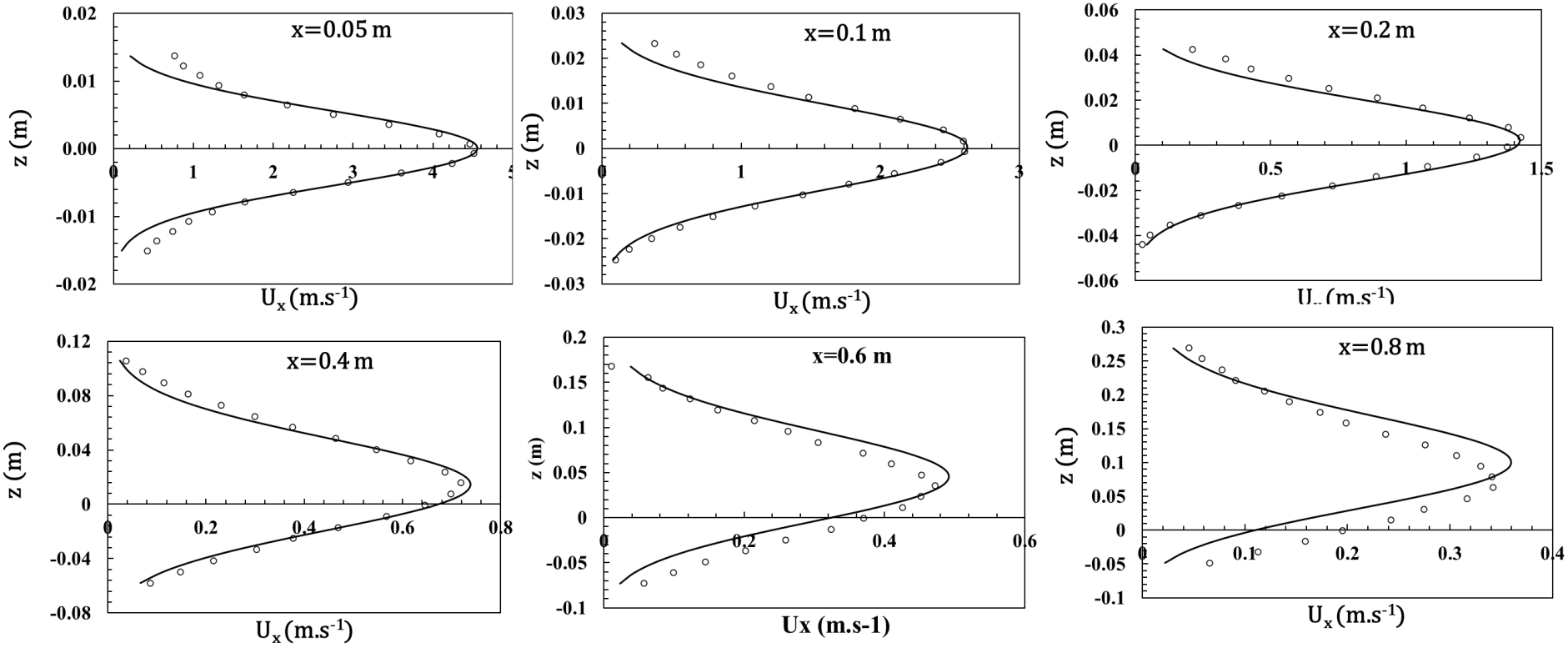

Figure 2.42 The axial velocity component U_x for the buoyant jet

To interpret this overestimation, we carried a sensitivity analysis to address the effect of measurement errors of the ambient and jet temperature as well as a local increase in the ambient temperature. Using *equ. 15* and the values in Table 2:4, the sensitivity analysis is done for ± 2°C from the set temperature for the jet and ambient.

The result of this analysis at x=0.8m is presented in Table 2:5, where the position of the jet centerline in the z-axis is given for different temperatures of the jet temperatures and ambient environment.

From this table, we can see that for the centerline to lower by 40%, the difference between the two jet and ambient temperature should be reduced by 4 °C. However, in the context of this experiment, the jet initial temperature is stable at 34±0.3 °C. Even if a local rise in the ambient temperature occurs it is less likely to be responsible for the deviation between the experimental data and model prediction.

	Z (cm)				
	T_∞ **(°C)**	**18**	**19**	**20**	**21**	**22**
	32	10.9	10.1	9.3	8.5	7.8
T_o **(°C)**	**33**	11.6	10.8	10.0	9.3	8.5
	34	12.3	11.6	**10.3**	10.0	9.2
	35	13.1	12.3	11.5	10.8	10.0
	36	13.8	13.0	12.2	11.5	10.7

Table 2:5: The effect of the change of the jet and ambient temperature in the vertical position of the jet centerline at x=0.8m

Figure 2.*43* Shows the vertical velocity of the buoyant jet at different distances from the source. Due to the upward drift resulting from the buoyancy effect the vertical velocity profiles are not symmetrical as in the case of the isothermal jet. The up drift is notices as the maximum vertical velocity below the jet centerline is greater to that above the centerline. The difference between these two maximum velocity increases in the downstream direction of the flow.

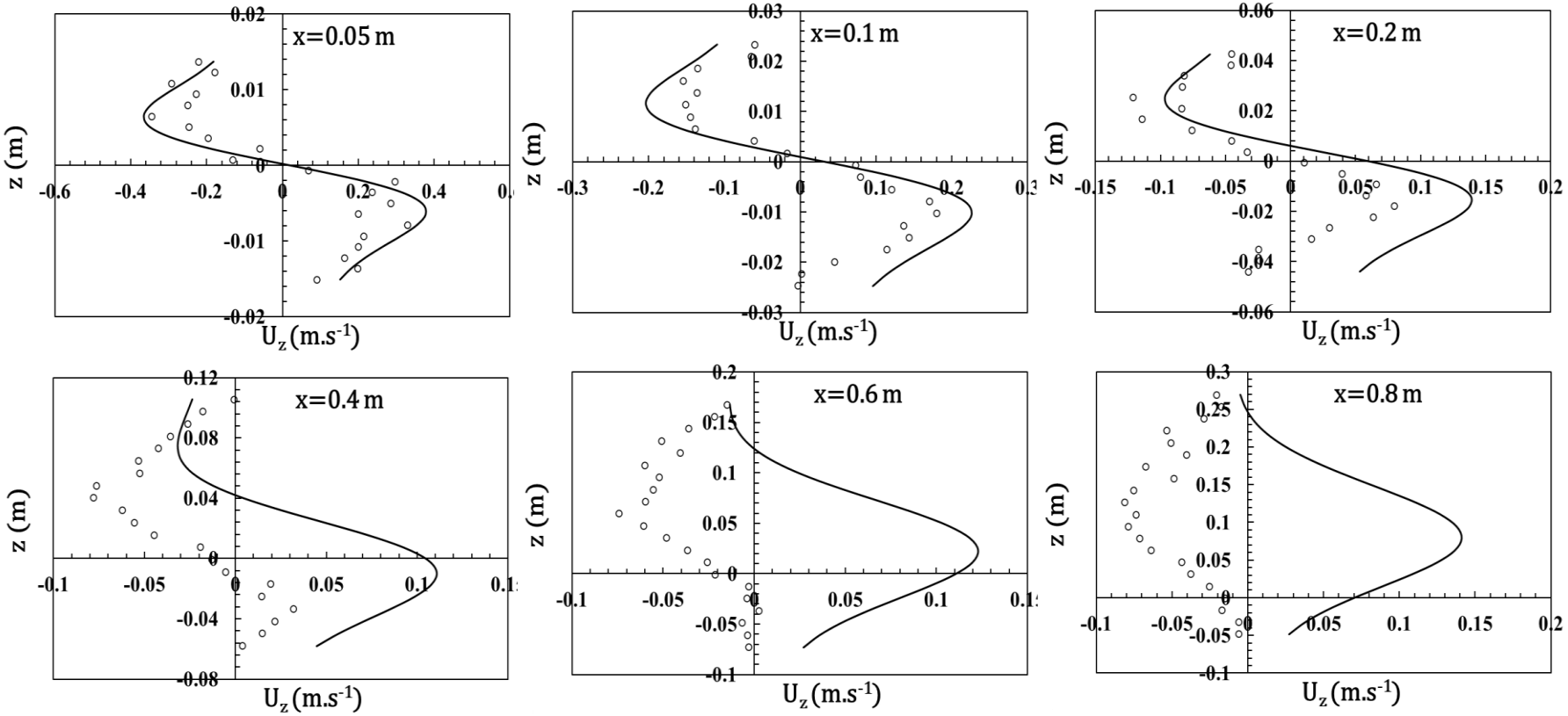

Figure 2.43 The radial velocity component U_z for the buoyant jet

2.3.2.5 Turbulence of the buoyant jet

Figure 2.44 and *Figure 2.45* show the axial and radial velocity fluctuations, respectively. In the momentum-driven part of the flow, the fluctuations profiles are similar to the isothermal jet. When the buoyancy effect started to appear later downstream, the shape of the profiles changes to have a single maximum value near the jet centerline. The normalized axial fluctuations are about 18% higher on average than the radial fluctuations.

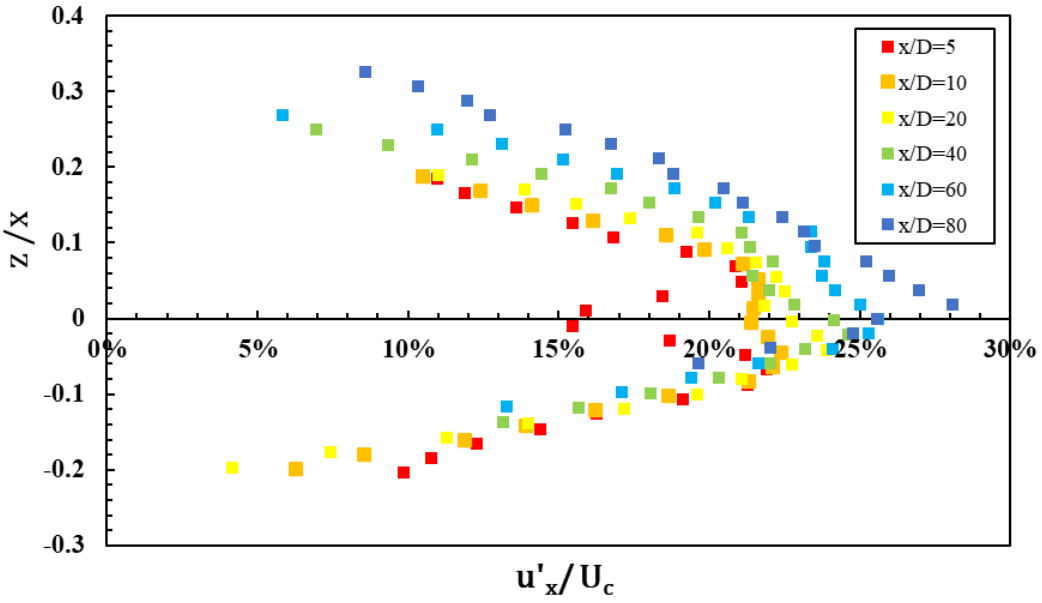

Figure 2.44 The axial component of the turbulence kinetic energy of the buoyant jet

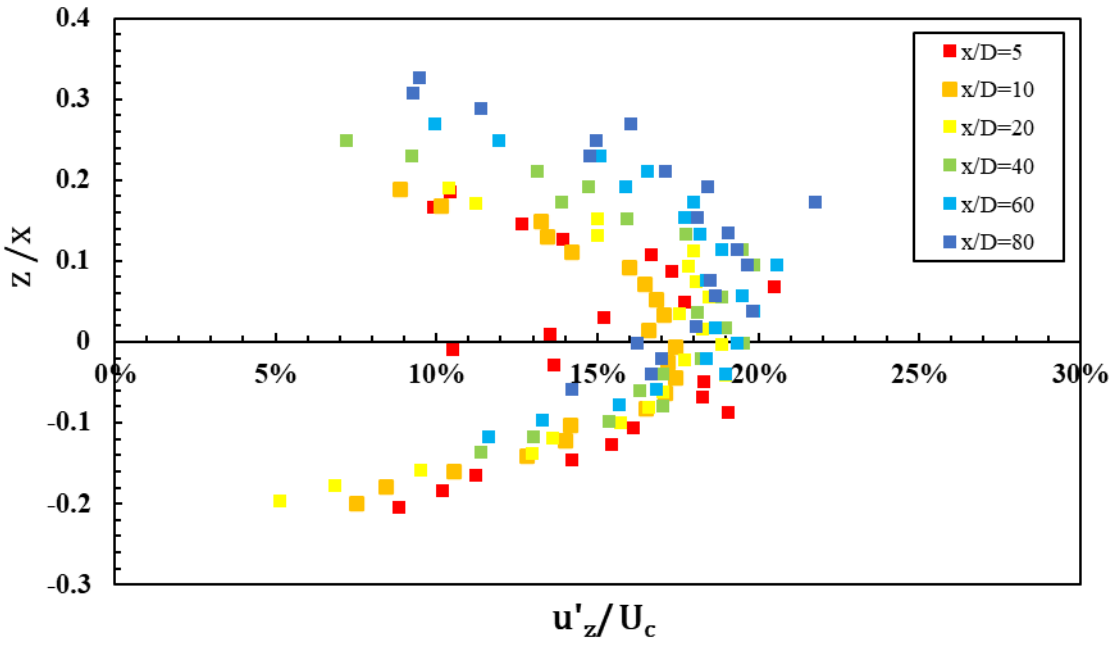

Figure 2.45 The radial component of the turbulence kinetic energy of the buoyant jet

2.4 Summary and conclusions

This chapter focuses on the design of a new experimental bench for the characterization of the gas flow. The experimental bench is composed of an environmental chamber where the measurements took place. The design of this chamber was based on the results of a CFD study that investigated the effect of the confinement due to chamber dimensions. The chamber was fabricated in ESTACA workshop with dimensions of 3.0 m x 2.0 m x 2.7 m. The objective was to characterize the flow field of an air jet of 5 m/s^{-1}, 34 °C and > 95% relative humidity. The air velocity was controlled with the help of a mass flowmeter, and DEHS was used as a gas tracer.

The first step in the characterization of the flow field was the study of an isothermal jet configuration with the same initial velocity. The study of this isothermal jet permitted the optimization of the measurement procedure using the Laser Doppler Anemometry. An improved measurement procedure was defined, with measurements that were conducted by repeating multiple one minute acquisition periods, instead of a previous procedure that measures 4000 particles in each point before moving to the next one.

The characterization of the isothermal air jet started with the study of the centerline velocity decay. The jet entrainment coefficient was established at a value of 6.2, and the mean absolute percentage deviation was only 3% between the experimental data and the model. Axial and radial velocity profiles were examined up to 0.8 m distance downstream. Each velocity profile is composed of 25 points at different distances from the jet centerline. The axial velocity profiles were compared with experimental studies and the model. The MAPD for all the axial velocity profiles is 8% excluding the three border points. Generally, near the jet borders, the measurement time is relatively high, meanwhile the flow instabilities are more frequent due to flow entrainment. Less odd points are noticed in the radial velocity profile when compared to the result obtained by Falcone and Cataldo [2003]. The model did not predict the change of the radial velocity direction due to jet entrainment near the jet border.

For the buoyant jet, there was a lack of experimental studies with such flow configuration. The study of the buoyant jet started with the definition of the jet centerline, which is executed by exploring 16 velocity profiles in the measurement range up to 0.8 m. With no existing model for the velocity profiles of the buoyant jet, we developed a procedure in MATLAB to transform the velocity profile of the isothermal jet configuration to the defined coordinates of the buoyant jet. This new buoyant jet model captured the effect of the buoyancy on the axial velocity profile. However, for the radial velocity profiles, the model didn't reflect the buoyancy effect manifested in the experiment results, which can be a subject for a future numerical study.

Chapter 3
Experimental study on the dynamics of droplets in a human-like horizontal jet

In the literature review article presented in Chapter 1 we have concluded that there is a lack of experimental data on droplet evaporation in human and human-like exhaled airflows. Besides, the evaporation models in the literature [Chen et al. 2020] [Wei and Li, 2015] are validated with data acquired from freefall evaporating droplet [Kukkonen et al. 1989] or a stagnant droplet [Liu et al. 2017].

In addition to their initial characteristics -composition, size, and velocity-, the dynamics of the exhaled droplets depend on the interaction between the exhaled airflow and the ambient environment. This interaction, as shown in *Figure 3.1*, governs the evaporation and motion of the droplets. In other words, the evolution of the droplet diameter and velocity is affected by the temperature, humidity, and velocity of the air jet.

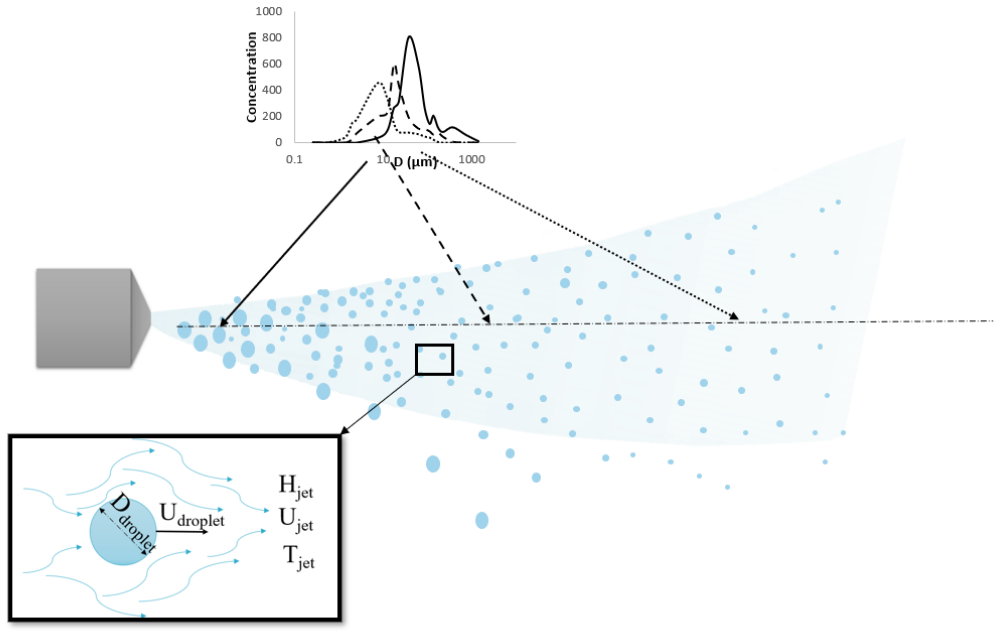

Figure 3.1 The motion and evaporation of a droplet in a humid buoyant turbulent jet

In *Figure 3.1*, the change of size distribution of the droplets as we progress downstream is illustrated. First, the concentration of the droplets decreases as the jet expands and mix with ambient air when it proceeds downstream. Second, the mode of the size distribution decreases downstream due to evaporation.

To explore these droplet dynamics, we studied in the first part of this study, 0, the velocity field of the buoyant turbulent jet that carries these droplets in terms of mean velocity components and

turbulence intensity. The next step is to explore the size and velocity change of NaCl-water solution droplets in the near field of such jets, which is the objective of this chapter.

This experimental study is conducted in the bench used in 0 and described in Sections 2.1.1 and 2.1.2. The measurements were carried out in the same environmental chamber using the LDA/PDA system described in the referred sections. The main difference in this bench is the droplets generation system. This alternative generation setup aims at studying the droplets dynamics in a humid buoyant jet, and it is presented in Section 3.2. The adopted experimental procedure is explained in section 0 and the results of this experiment are discussed in section 3.4.

3.1 Experimental Bench

As mentioned above, the same experimental bench employed to characterize the velocity field of the buoyant turbulent air jet in the previous chapter is used to study the droplet dynamics in this chapter. *Figure 3.2* displays the experimental bench and illustrates how the droplets and the air jet are introduced to the environmental chamber. The nozzle -previously shown in *Figure 2.15*- introduces the droplet-laden humid buoyant jet to the environmental chamber. As seen in the zoomed in part of *Figure 3.2*, the droplet generator injects droplets along the central axis of the nozzle, while the humid jet is introduced by a radial hole in the nozzle body. The air jet and the droplets are then mixed inside the nozzle of 10 cm in length and 10 cm in diameter. The ensemble of this generation system is called the oropharyngeal emission simulator and its development was part of this research project. A comprehensive description of the oropharyngeal emission simulator is provided in the next section.

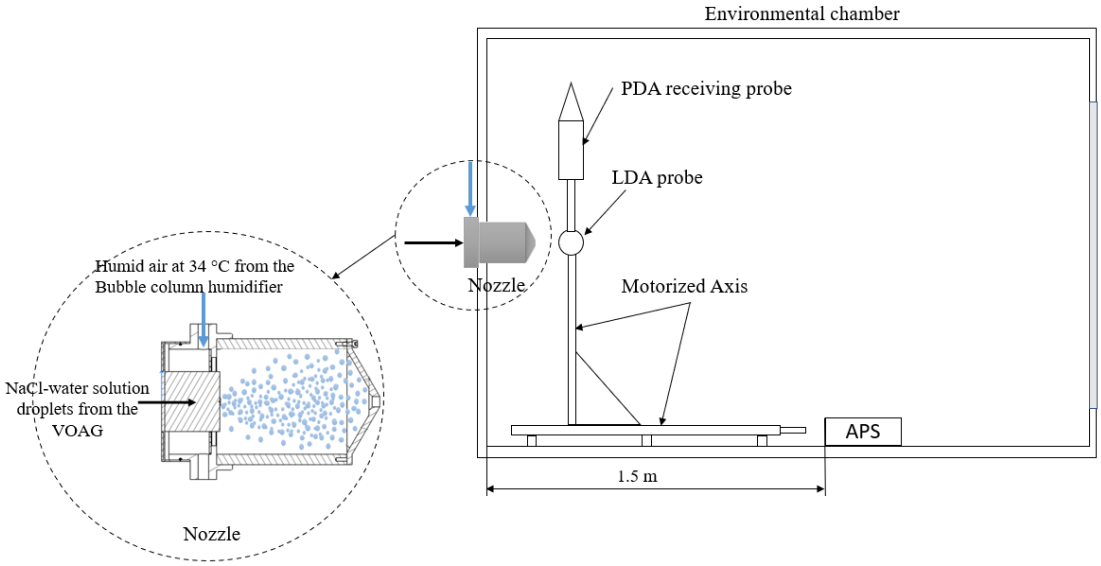

Figure 3.2 The experimental bench for the droplet dynamics study

The measurements were conducted using the **L**aser **D**oppler **A**nemometry (LDA) system to measure the droplets velocity and **P**hase **D**oppler **A**nemometry (PDA) to determine the size of the droplets. In addition to the LDA / PDA system the Aerodynamics Particle Sizer was used to measure the size distribution of the dry residues of the droplets. These measurement techniques are presented briefly in the section 3.1.1 and section 3.1.2.

3.1.1 Laser Doppler Anemometry and Phase Doppler Anemometry

As previously explained, in a LDA system, an ellipsoid measurement volume is formed by the intersection of two beams of coherent light. When a particle passes through this volume, it reflects a light signal. The analysis of this signal allows us to find one of the components of the particle's velocity. In the previous experiment, we used this technique to indirectly measure the air velocity, provided that the particle is sufficiently small to follow the air jet, a tracer. On the contrary, in this experiment, the objective is the particle itself. We will use the two-components LDA system to track the droplets' velocity in the near-field of the jet.

Phase **D**oppler **A**nemometry (PDA) is an extension to the LDA for measuring the optical diameter of particles. The principle consists of placing two receivers at different locations, when the droplet passes the measurement volume the two signals are recorded. The phase shift between the two signals is linearly related to the diameter of the particle.

In the current used PDA system from Dantec the receivers are placed in the receiving probe shown in *Figure 2.1*. The probe is mounted on the motorized axis at 62° degrees from the emitting probe.

3.1.2 Aerodynamic Particle Sizer (APS)

In addition to the PDA measurements for the size of the droplets, we used the Aerodynamic Particle Sizer (APS) from TSI to evaluate the size of the dry residues. The APS measures the aerodynamic diameter by evaluating the time of flight of a particle being accelerated in a jet flow. The time of flight here is the time the particle takes to travel between two light beams. The APS measures the aerodynamic diameter of the particle depending on its capacity to accelerate between the two light beams. The APS measures particles in the range of 0.5 µm - 20 µm with a sampling airflow of 1 $L.min^{-1}$ that is mixed with a sheath airflow of 4 $L.min^{-1}$. It is worth mentioning that evaporation might occur when accelerating the particle during the measurement process. Thus, the APS is not applied to measure the size of volatile droplets and it is only suitable for dry residues. The results of the APS measurements are discussed in section 3.5.

3.2 The oropharyngeal emission simulator (OES)

The objective of this generation system is to generate an air jet with controlled temperature and humidity laden with monodispersed droplets of NaCl-water solution. This droplet generator is based on the Vibrating Orifice Aerosol Generator (VOAG) from TSI. Conventionally, the VOAG

is used to produce monodispersed particles from liquid solutions with specific concentration. The working principle of the VOAG comprises of applying uniform disturbances to a liquid jet, which generates monodispersed droplets. These droplets then go through a controlled drying process to produce monodispersed dry residues.

However, in this experimental study, our objective is to inject monodispersed droplets in a humid buoyant jet to study their dynamics. This application implies modifications to the operation of the generator. The first version of this modified system - the oropharyngeal emission simulator- is developed in the CERTES lab by Da et al. [2015]. The oropharyngeal emission simulator produces monodispersed droplets of sodium fluorescein water solution with a mass concentration of 10 $g.L^{-1}$. This concentration simulates the presence of salts in human saliva [Da et al., 2015]. In section 3.2.1 and section 3.2.2, we will describe the conventional operation of the VOAG then explain the modifications applied to the current second version of the emission simulator, respectively.

3.2.1 The conventional use of the Vibrating Orifice Aerosol Generator

The working principle of the Vibrating Orifice Aerosol Generator (VOAG) is based on generating a cylindrical liquid jet and applying a periodic disturbance to this jet in order to break it into uniform droplets. The jets such as the one produced by the VOAG are naturally unstable and break into nonuniform droplets [TSI, 2013]. Applying disturbances to these jets controls the size of the droplets resulting from the jet breaking. In *Figure 3.3* the break-up of a cylindrical liquid jet into uniform droplets is illustrated. As shown, the liquid breaks after passing the vibrating orifice of the generator.

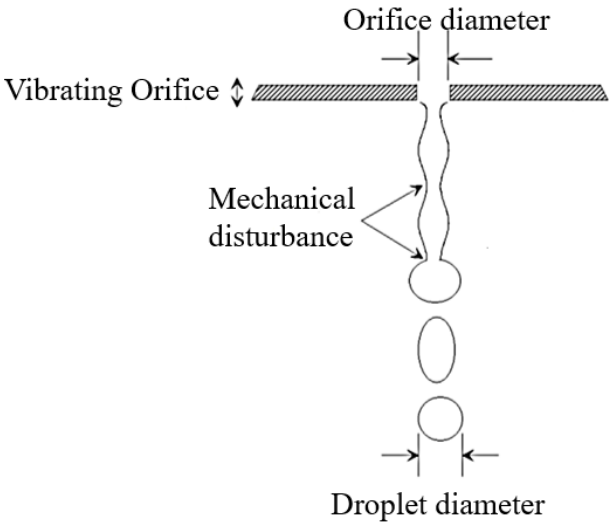

Figure 3.3: The break-up of liquid jet into uniform droplets [TSI, 2013]

The VOAG comprises two systems: liquid system and air system. The objective of the liquid system is to generate monodispersed droplets. The liquid system is shown in *Figure 3.4* in blue color and is composed of a syringe pump, membrane filter, an orifice, a drain, and all these parts are connected with Teflon piping. To generate monodispersed droplets, the syringe pump if filled with a solution of known concentration, and the pump is driven by a stepper motor. The liquid from the syringe passes through a membrane filter before being injected through an orifice to generate the cylindrical liquid jet. The orifice is placed in the VOAG head as shown in *Figure 3.4*. The orifice seat is connected to the membrane filter from one side and a drain valve from the other size. When the drain valve is closed, the pressure builds up on the orifice's inner side, and the liquid is pushed through the orifice generating the jet. As illustrated in *Figure 3.4*, the VOAG head holds a piezoelectric ceramic. The signal generator applies a periodic signal to this piezoelectric ceramic, which induces uniform vibration on the orifice and leads to the generation of the uniform droplets.

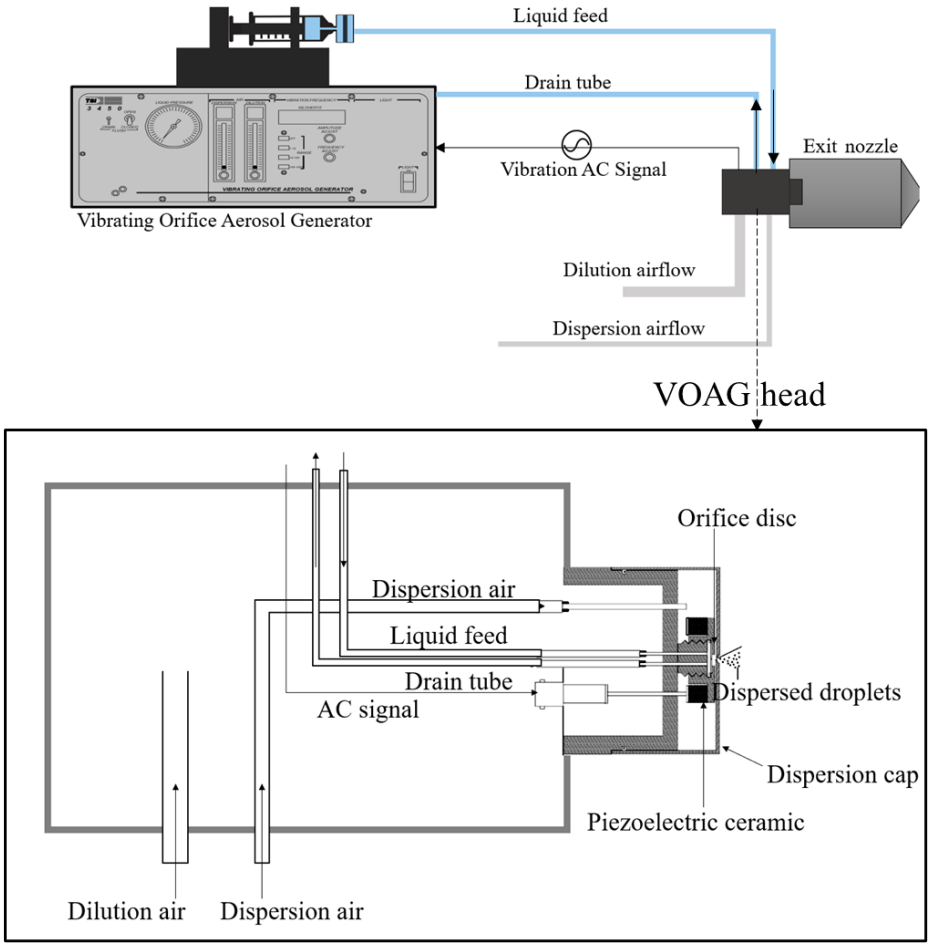

Figure 3.4: The Vibrating Orifice Aerosol Generator from TSI

To prevent the collision and combination of the droplets after the orifice, a dispersion airflow is injected into the dispersion cap shown in *Figure 3.4*. Adjusting the dispersion flow rate reduces the chances of the formation of double or triple droplets. To produce monodispersed particles, the droplets are mixed with a dilution airflow inside a cylinder to evaporate. In the conventional operation of the VOAG, dry air passes through a filter to supply both the dispersion and dilution flowrates, which is called the air system.

However, in this experiment, we need to prevent the evaporation of the droplets before the exit nozzle. Hence, dry air is replaced by humid air at 34°C. This alternative system is explained in the following section.

3.2.2 The second version of the oropharyngeal emission simulator (OES V.2)

In the conventional operation of the VOAG, the recommended airflow for the jet dispersion and dilution flow rate are 1.5 $L.min^{-1}$, and 50-80 $L.min^{-1}$, respectively. Adjustments were made to this system in order to replace it with humid air. On the exploratory phase of the experiment, the dilution air system was replaced by a direct supply from the bubble column humidifier that is enough to obtain 5 $m.s^{-1}$ of air velocity at the nozzle exit.

The bubble column humidifier - built for this experiment - is composed of a glass cylinder of 10 cm diameter that contains pure water. A copper heating coil was placed inside the cylinder to control the temperature of the pure water. The working fluid in the heating coil is heated in a controlled temperature water bath. The airflow first passes through a filter before it is regulated by a thermal mass flow controller (Brooks instruments, SLA5800Series). Then the air is introduced into the cylindrical column through a porous air diffuser. The air temperature is measured with a thermocouple placed inside the nozzle as shown in *Figure 3.5*. To adjust the air temperature to 34°C at the nozzle, the temperature of the water inside the humidifier glass cylinder is regulated with the controller of the water bath.

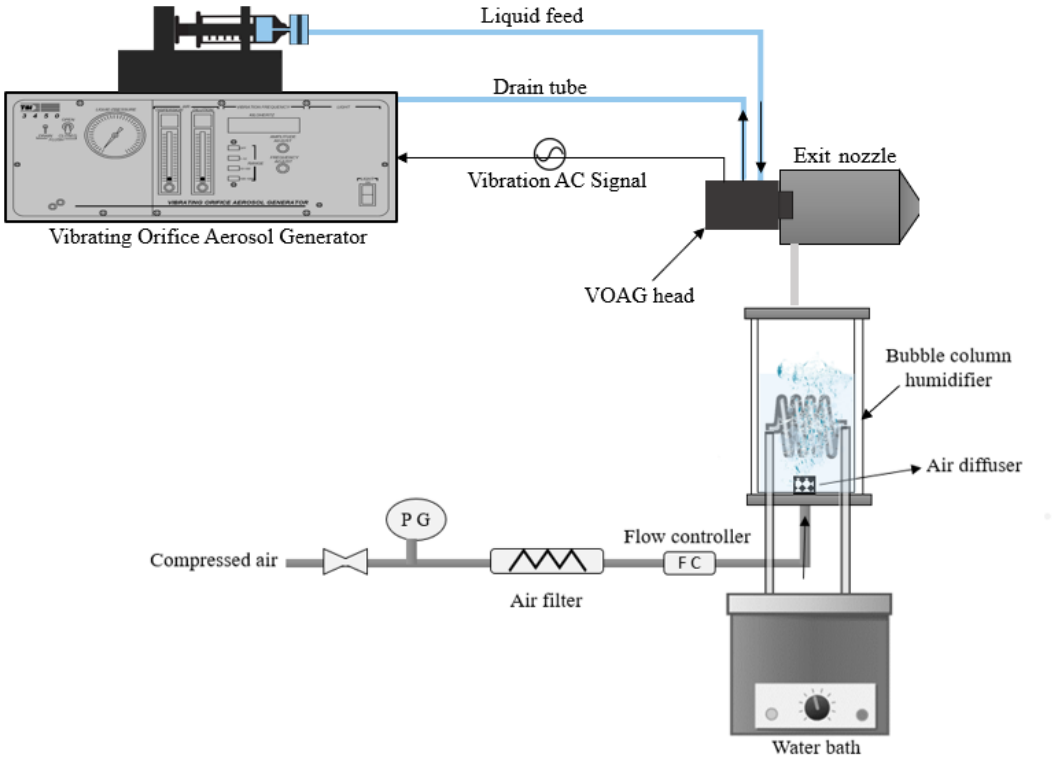

Figure 3.5: *The second version of the oropharyngeal emission simulator*

The dispersion airflow rate was set to its recommended value, and the conventional dry air is replaced by humid air. This flow configuration resulted in significant condensation in the piping system of the dispersion airflow, which affected the stability of the flow itself because condensation changes the density of the humid air.

In another trial, we returned to using dry air for the dispersion, which resulted in a multimodal droplet size distribution at the nozzle exit as illustrated in *Figure 3.6*. In this figure, the number of droplets recorded for during 30 minutes is presented for each droplet size. It must be pointed out that the PDA system records the size of the droplets in bins of 0.1 µm.

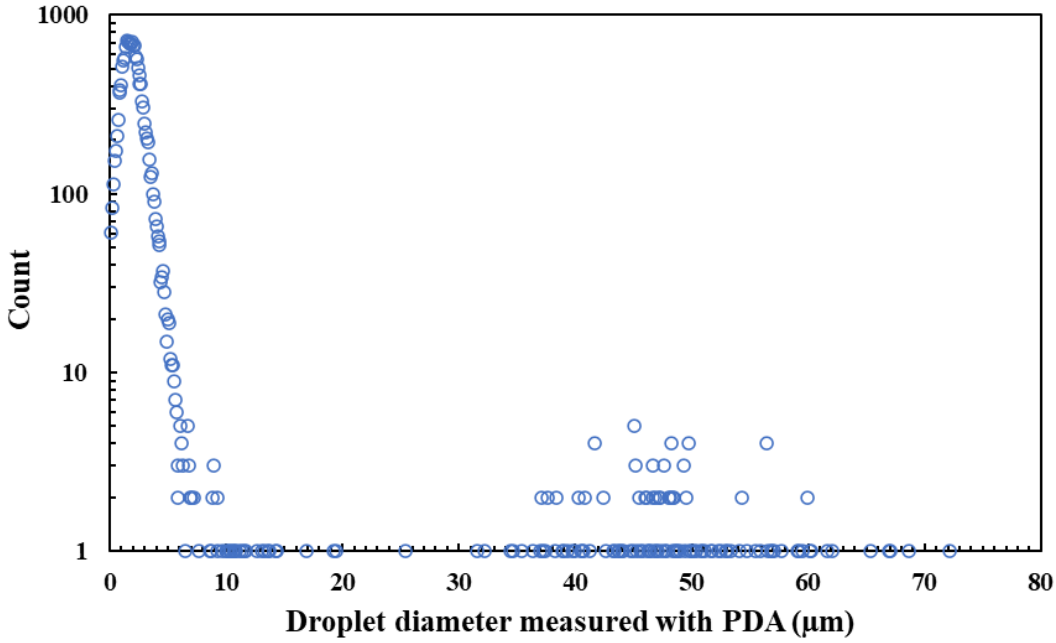

Figure 3.6: The size distribution of the droplet with dry dispersion airflow at nozzle exit (x=0.003 m, y=0, z=0) of 30 minutes count

In *Figure 3.6*, the majority of the counted droplets are less than 7 µm while the droplets generated by the VOAG are 1% of the total count. The droplets of less than 7 µm were measured even when the VOAG isn't working, and only humid air enters the nozzle. These droplets are assumed to be generated in the bubble column humidifier. They might be generated on the liquid surface inside the generator as the air bubbles inside the liquid column cause rupture in the liquid surface. These droplets are then carried by the airflow. Although the formation of these droplets was not anticipated, they can be considered as a tracer for the gas velocity.

To analyze larger droplets, we zoomed into the size distribution in *Figure 3.7*. In this figure, the droplets of more than 10µm are presented in bins of 2 µm. In addition to the typical size range produced by the VOAG in the range of 30-50 µm, double and triple droplets are noticed. The evaporation and condensation occur due to the mixing of humid and dry air inside the nozzle result in generating droplets in the range of 10-20µm. Droplets are considered monodispersed if the geometric standard deviation of the size distribution is less than 1.2. Accordingly, the droplets generated using dry dispersion airflow are not monodispersed as the geometric standard deviation of the droplets larger than 10 µm is 1.56.

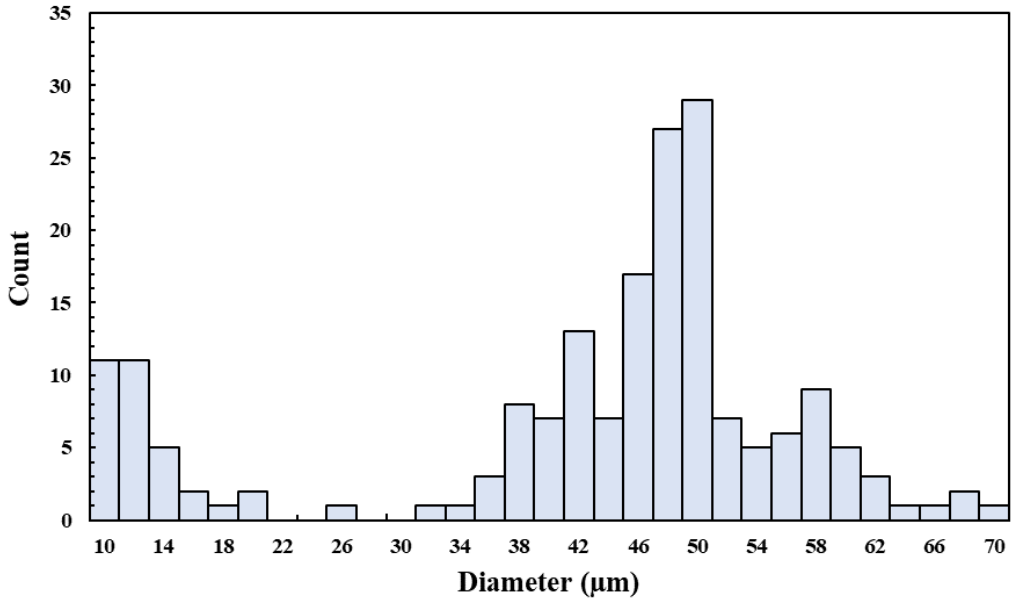

Figure 3.7: The size distribution of droplets larger than 10 µm with dry dispersion airflow at nozzle exit (x=0.003 m, y=0, z=0) of 30 minutes count

To minimize the effect of evaporation and condensation inside the nozzle, no dispersion airflow is applied, and humid air is introduced directly to the nozzle after the VOAG exit. The size distribution of the droplets obtained from this configuration is shown in *Figure 3.8*. The geometric mean of the distribution is 45.8, and it is considered a monodispersed as the geometric standard deviation is 1.18. It is observed in the figure that the droplets in the range of 10-35 µm disappeared when no dry air is introduced in the VOAG.

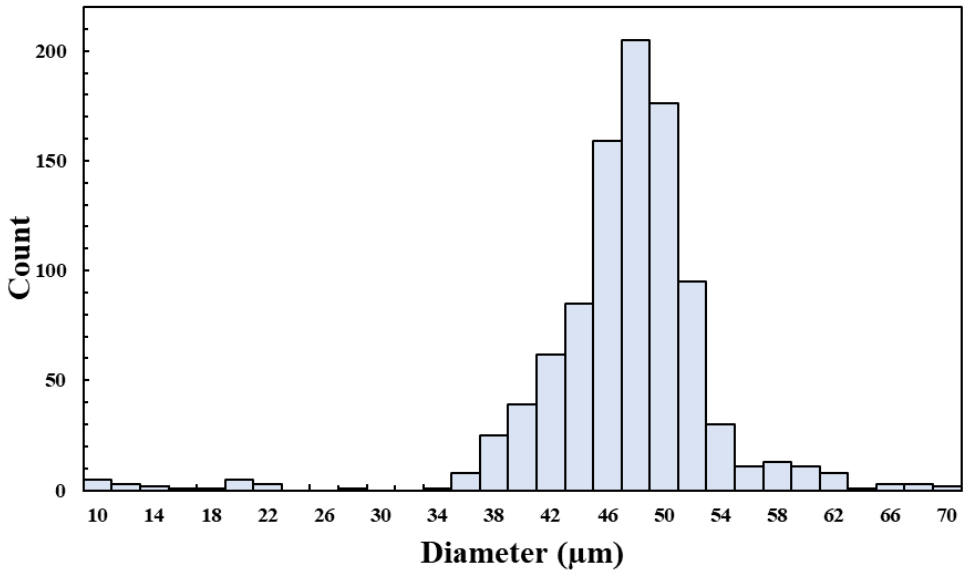

Figure 3.8: The size distribution of the droplet without dispersion airflow at (x=0.003 m, y=0, z=0) of 30 minutes count

The theoretical mode calculated using the frequency and liquid flow rate of the VOAG is 40 μm, but PDA measurements show a mode of 45.8 μm, which can be attributed to condensation inside the nozzle. *Figure 3.9* depicts a photograph taken at the nozzle entry, where condensation was clearly visible on the nozzle interior surface.

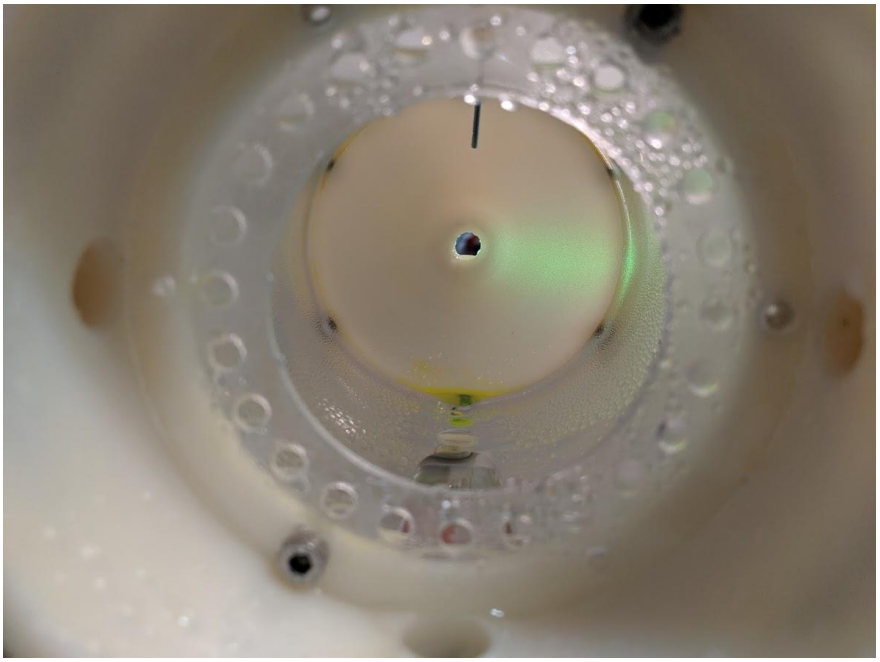

Figure 3.9: *A photograph taken at the nozzle entry shows condensation on the nozzle's inner surface.*

3.3 Procedure

In this section, we explain the procedure adopted to measure the velocity and size measurement of monodispersed droplets. The procedure starts with the generation of the monodispersed droplets. As mentioned in the thesis introduction, we will use, in this experiment, a sodium chloride solution of 10 $g.L^{-1}$ concentration. The solution is prepared right before each experiment to avoid the formation of NaCl crystals. For the preparation of the solution, 5.000±0.001 g of NaCl is weighted using an analytical balance (kern ABT 100-5m), then the salt is mixed with 500 mL of ultra-pure water in a volumetric flask.

3.3.1 VOAG operation

To start the operation of the VOAG, a syringe of 60 mL volume is filled with the NaCl solution and then connected to the stepper motor. The liquid feed rate is 0.138 $mL.min^{-1}$ as the syringe diameter is 26.6 mm.

A particular pressure level should be applied to launch the jet through the 20 µm orifice diameter used in this experiment. In the beginning, a higher pump speed is applied to build a sufficient liquid pressure jet. After the start of the jet, the liquid flow rate is set to its operating value.

When the jet is stabilized, the signal generator applies periodic vibration at 69 kHz frequency to generate droplets of 40 µm diameter. A deflection test, suggested by the manufacturer, is performed to conduct the first visual check for droplets' monodispersity. The is done by applying an airflow between 5-15 $mL.min^{-1}$ in a perpendicular direction to the liquid jet axis. If the droplets are monodispersed, then the droplet jet will have a single trajectory otherwise, another trajectory will be observed as shown in the photos below.

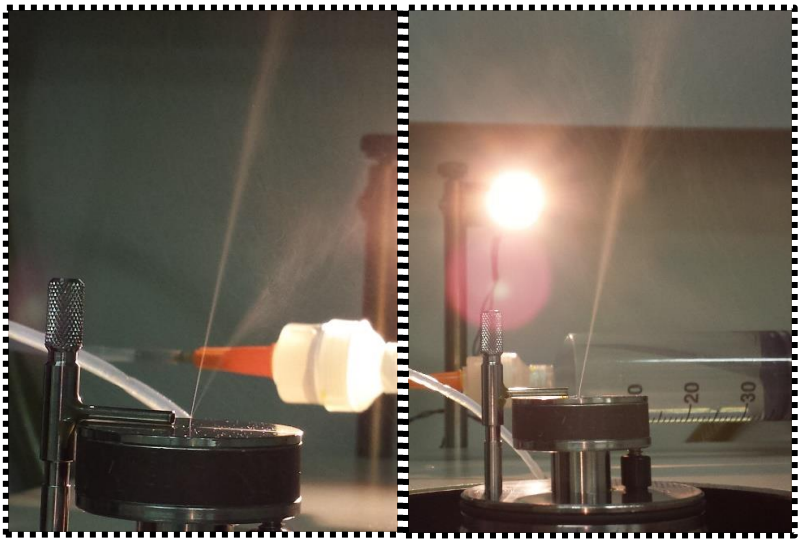

Figure 3.10: VOAG deflection test [Zambrelli, 2014]

After the deflection test the VOAG head is attached to the nozzle and the initial conditions of the jet, namely, the velocity and, temperature are set during a process that usually takes 3 hours. This setting time is required to obtain thermal equilibrium between the systems and the ambient environment before conducting any measurements. Maintaining a stable initial jet conditions is a technical challenge. In the following section we discuss to what extend each of these conditions is controlled.

3.3.2 The stability of the jet initial conditions

In this experiment, the main technical challenge is to stabilize the jet initial conditions, namely, size distribution, temperature, and velocity. The first concern is the VOAG generation itself, as the 20 µm orifice can be easily clogged because of the presence of any slat or dirt particles in the liquid system. The second concern is the stabilization of the jet velocity, as the velocity is sensitive to the temperature change, which might happen for any of the following reasons:

- Temporary removing the VOAG to perform the deflection test.
- When adding water to the bubble column humidifier
- Injecting the salt droplets into the nozzle. Because the presence of these droplets changes the thermal state inside the nozzle. Thus, the regulation of the velocity and temperature should be done during the steady operation of the VOAG.

To observe the stability of the initial velocity and temperature, a 100 mins experiment was conducted. First, a series of trials were made to find the setting parameters for the water bath and mass flow controller. Then, the temperature in the nozzle is registered using a thermocouple, and the droplets' velocity and size were measured near the nozzle exit using the LDA/PDA systems.

The temperature inside the nozzle, as well as in the environmental chamber, are shown in *Figure 3.11*. The temperature in the nozzle rises by 0.3 °C from its initial reading, 33.8 °C. While the temperature in the chamber increased by less than 1 °C during the total time of the experiment.

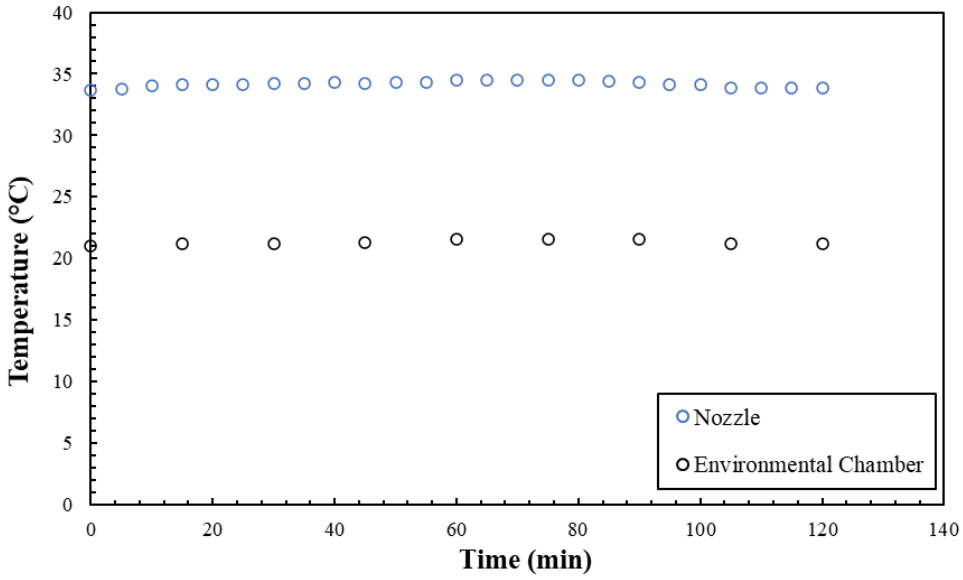

Figure 3.11: The initial exit temperature of the humid air and the environmental chamber temperature monitored for two hours experiment

The analysis of the velocity for the different droplet sizes is illustrated in *Figure 3.12*. This figure shows the velocity of the droplets measure during 100 mins at the jet exit. The mean axial and radial velocities are averaged during this period for each droplet size. The mean is calculated by averaging the velocity of the droplets in each size bin given by the PDA system -0.1 µm. In this figure, we can identify four distinguished size groups. The first group is the small droplets of less than 7µm. The mean axial and radial velocities of these droplets are the same, which are 5 $m.s^{-1}$ and ≈0 $m.s^{-1}$, respectively.

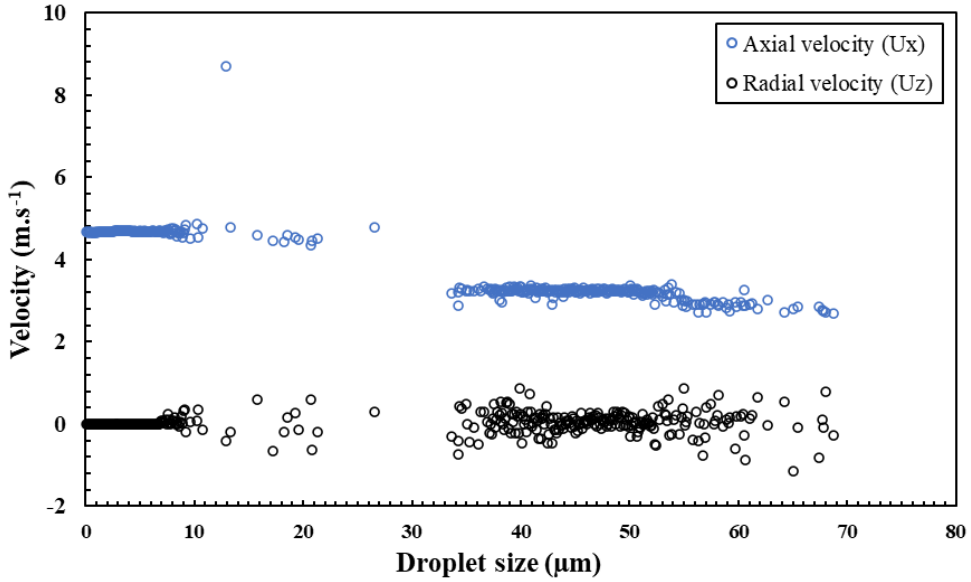

Figure 3.12: The mean axial and radial velocity for the droplets of different sizes at nozzle exit (x=0.003 m, y=0, z=0) for 100 minutes count

The second group is between 10 and 30, which looks scattered in this figure. These droplets, as presented in *Figure 3.8*, are very low in number. Which explains why the mean velocity has this discrepancy. The thirds group contains the droplets in the conventional VOAG generation range, 30-50 µm. Although the radial velocity of these droplets is the same as the droplets in the first group, which is anticipated in the jet center, of course, their axial velocity is 4 $m.s^{-1}$. The last group is the droplets of more than 57 µm, which are, in fact, the doubles and triples of droplets typically generated by the VOAG. These droplets are formed due to inadequate dispersion and dilution flow rates. However, as discussed above, this was the best possible technical solution to produce droplets with the required initial velocity, temperature, and humidity within this size range. For the following discussions and results analysis, we will focus on the third group, and the first group is considered as a gas tracer.

Figure 3.13 shows the axial velocity of the droplets less and more than 7 µm averaged over one minute. During the experiment, the velocity seems to change within a range of ±10% of the initial value, 5 $m.s^{-1}$. The sudden change of the droplets' velocity at 40 mins and 54 mins remains unexplained as it is not linked to specific intervention during the experiment.

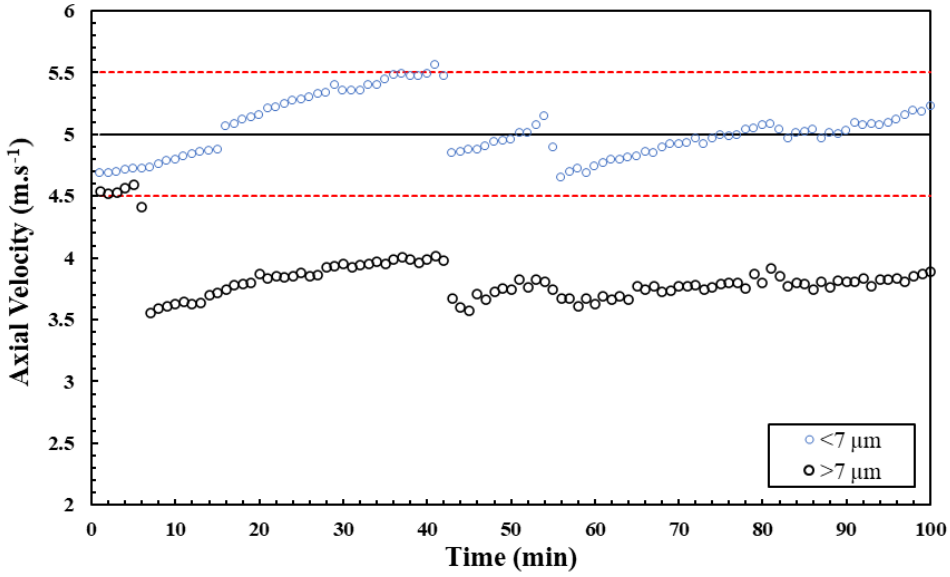

Figure 3.13 The mean axial velocity of the droplet less than and more than 7 µm, at the nozzle exit (x=0.003 m, y=0, z=0) for 100 minutes count

The jet initial conditions and the set parameters of the experimental setup, discussed in the previous sections, are summarized in Table 3:1.

Environmental chamber temperature	20 (°C)
Mass flow controller set point	14 (nL.min^{-1})
Set water temperature of the humidifier	43 (°C)
Initial air temperature, nozzle	34 (°C)
VOAG operating parameters	
Syringe volume	60 (mL)
Orifice diameter	20 (µm)
Salt concentration	10 (g.L^{-1})
Frequency	≈69 (kHz)
Liquid feed rate	0.138 (mL.min^{-1})

Table 3:1 The jet initial conditions and the set parameters

3.3.3 The temperature and humidity along the jet horizontal axis

The characterization of the temperature and humidity field is important in the interpretation of the droplets' size evolution. With the jet parameters described above in Table 3:1, temperature and humidity measurements were conducted along the jet axis from (0.003, 0, 0) to (0.4, 0, 0). Measurements were conducted using a Kimo thermo-hygrometry probe [KTHP-130-BRF] that works in the temperature range (-20 to +70 °C) and humidity range of (5 to 95 %RH).

Figure 3.14 shows how the jet temperature along the horizontal axis decreases from 32 °C at the jet exit (x=0.003 m) to 21.3 °C at (x=0.403 m). 77.3% of the decay in the temperature appears in the first 0.1 m, after this distance, the decay occurs at a lower rate. A similar graph for the humidity in the same range, is presented in *Figure 3.15*.

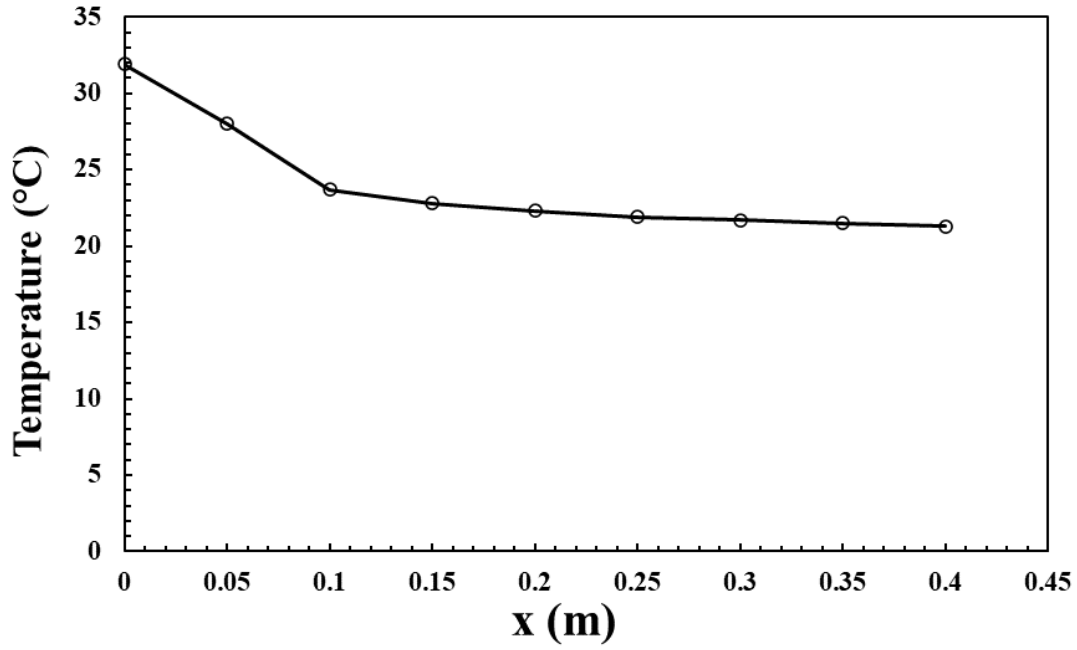

Figure 3.14 The temperature along the jet horizontal axis (0.003, 0, 0) to (0.4, 0, 0)

The relative humidity drops from 91.5% at x=0.053 m to 53% at x=0.403 m. It is important to note that the measurement of relative humidity near the exit is not accurate because the humidity level is above the device measurement range.

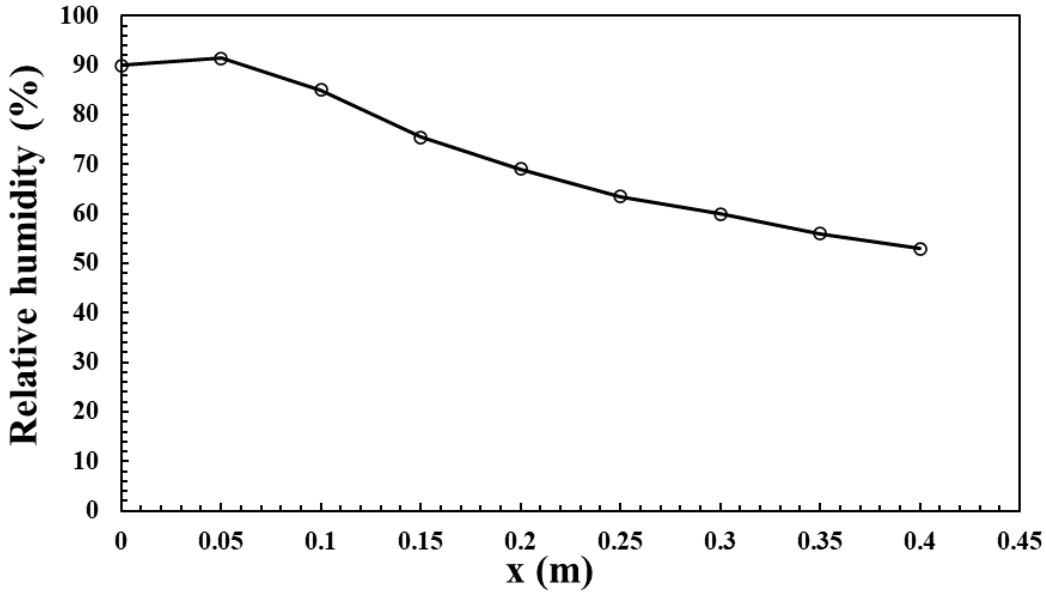

Figure 3.15 The humidity along the jet horizontal axis (0.003, 0, 0) to (0.4, 0, 0)

To understand the effect of the humidity and velocity fields, we used a simple model [Hinds, 1999] to predict the evaporation of a pure water droplet of 40 µm at 32 °C and 91.5 % RH, which is 16.6 s, while the same droplet evaporates in 2.9 s at 21.3 °C and 53 %.

3.3.4 Measurements of droplets size and velocity in a humid jet

LDA and PDA measurements were conducted on the jet centerline between 0.003 m and 0.4 m from the nozzle exit, and on vertical profiles at 0.05 m, 0.1 m, 0.15 m and 0.2 m between $-2 < \eta < 2$, η, with $\eta = \frac{z}{(x+x_o)\beta}$, and β is the jet spread constant = 0.114. One of the outcomes of the convergence analysis of the previous jet campaign is that it is better to minimize the sampling time at one point and repeat the measurement over the full profile. Hence, in this experiment, data were collected for 1 min at each point, and the whole measurement sequence -11 points in the case of vertical profiles- is repeated 15 times.

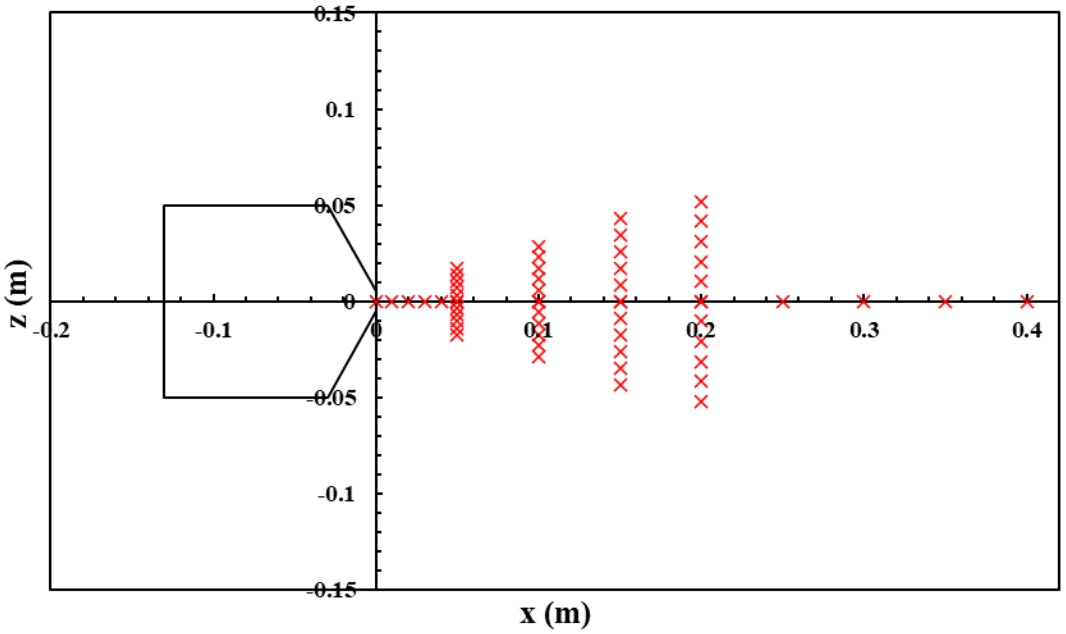

Figure 3.16 The location of the measurement points using PDA/LDA

Figure 3.16 illustrates the location of the measurement points along the centerline as well as the vertical profiles. In the next section, we present the results of the measurement conducted at these points. The evolution of size distribution and velocity is analyzed separately for the droplets:

- Along the centerline in the range of 0.003 m - 0.053 m.
- Along the centerline in the range of 0.003 m - 0.403 m.
- Each of the vertical profiles at 0.05 m, 0.1 m, 0.15 m, and 0.2 m.

The size and number of the droplets generated by the VOAG and measured at the nozzle exit (x=0.003 m, y=0, z=0) depend on flow conditions inside the nozzle as well as the operating parameters. Controlling all these factors together is a very delicate process, which results in changes in the size distribution measured at the nozzle exit. The size distribution at the exit is considered as a reference distribution in each experiment, and these distributions are presented in Annex A. We present in Table 3:2 the different experiments their results will be discussed later, their data, the explored range in addition to the reference of the figure in the Annex.

Experiment	**Date**	**Studied range**	**Reference to size distribution at the exit**
E1	26 March 2021	Centerline up to 0.05 m	*Figure: A-1*

E2	17 March 2021	Centerline up to 0.4 m	*Figure: A-2*
E3	10 March 2021	Vertical profile at 0.05 m	*Figure: A-3*
E4	11 March 2021	Vertical profile at 0.1 m	*Figure: A-4*
E5	11 March 2021	Vertical profile at 0.15 m	*Figure: A-5*
E6	09 March 2021	Vertical profile at 0.2 m	*Figure: A-6*

Table 3:2 The conducted experimental campaigns

3.4 Results on dynamics of the NaCl-water solution droplets

In this section, we explore the change of the droplet's velocity as a function of its size and location from the nozzle exit. Then the results of measurements are analyzed to observe the evolution of the droplets' size along the jet centerline and across five vertical profiles. The objective of this analysis is to detect notions of evaporation in a droplet-laden jet.

3.4.1 The velocity of the droplets

The objective of this section is to analyze the change of the droplet velocity along the centerline. The BSA software provides information about the droplet's axial and radial velocity in addition to the diameter of the droplet. The objective of this section is to analyze the change of the droplet velocity along the centerline. The BSA software provides information about the droplet's axial and radial velocity in addition to the diameter of the droplet. As mentioned before, the size of the droplet is given in bins of 0.1 μm. For this analysis, the mean velocity for each droplet size in each measurement point is calculated and plotted against the droplet size. The mean axial velocity of the droplets at the jet exit, 0.0125 m, 0.025 m, 0.0375 m, and 0.05 m is presented in *Figure 3.17* as a function of their size.

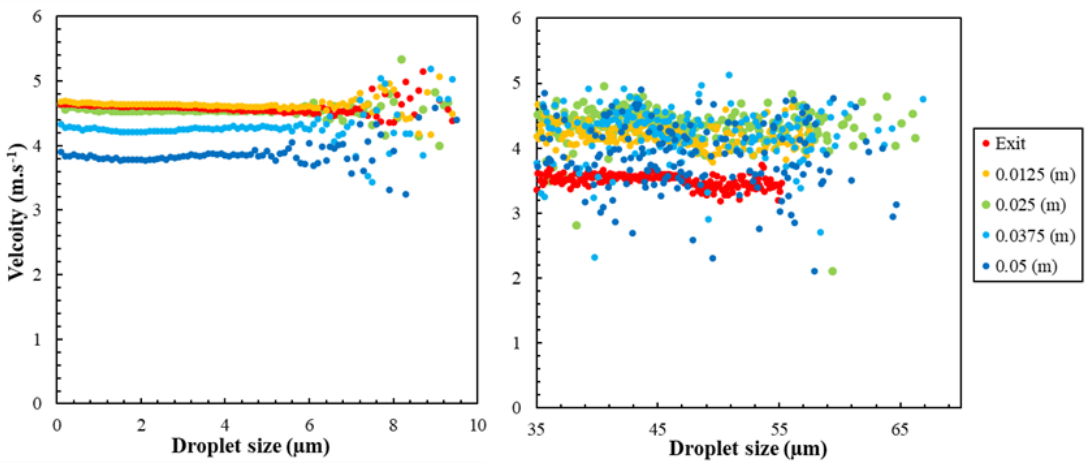

Figure 3.17 The mean axial velocity of the droplets over 0.05 m along the jet centerline

As shown in the Figure, the velocity of the smaller droplets -which are considered tracer particles- at the first two points downstream is very close to the exit velocity. This is because these two points are actually inside the jet core region, where only a slight change in the air velocity occurs (see *Figure 2.26*). At 0.0375 m and 0.05 m, the velocity of these droplets decreases to 4.2 $m.s^{-1}$ and 3.8 $m.s^{-1}$ from an initial value of 4.6 $m.s^{-1}$. As the jet proceeds and the droplet number decreases, we start to see discrepancies in the velocity of the droplets. These discrepancies appeared for the droplets of more than 5.5 µm as 98.5% of the droplets near the exit have less than 5.5 µm diameter.

The mean velocity of the VOAG-generated droplets increases inside the jet core from 3.86 $m.s^{-1}$ -near the exit- to 4.24 $m.s^{-1}$, and 4.35 $m.s^{-1}$ at 0.0125m, and 0.025, respectively. The mean initial velocity of these droplets in the VOAG exit is less than the velocity of the humid air coming from the generator. The velocity of these droplets increases with distance to reach the air velocity at 0.025 m from the exit. After this point, these droplets start to decelerate with distance.

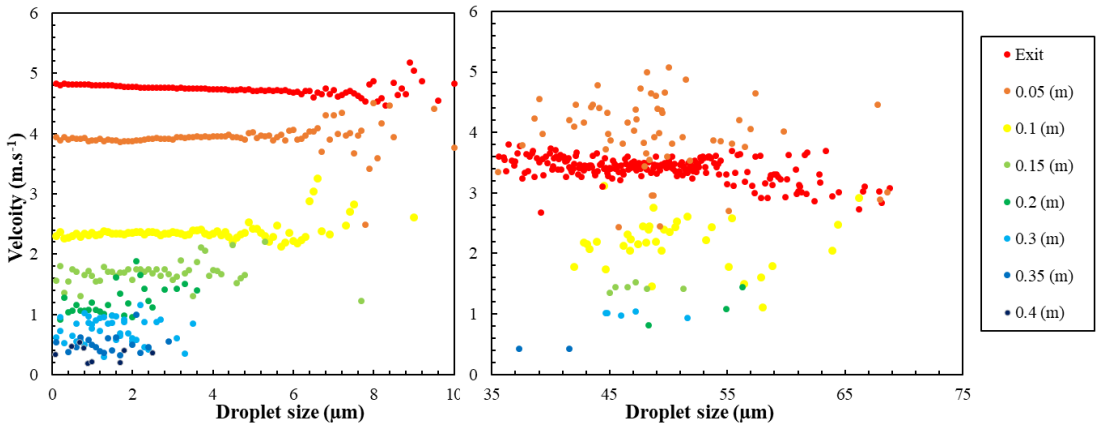

Figure 3.18 The mean axial velocity of the droplets over 0.4 m along the jet centerline

Figure 3.18 shows the change of the droplets velocity up to 0.4m downstream. The velocity of the droplets <10 µm continues to decrease with distance, even when only few droplets were measured. As previously noticed, the velocity of the droplets in the range of 35 µm-70µm increases after passing the exit of the nozzle and before it starts to decelerate later.

3.4.2 The evolution of the droplets size along the centerline

Before investigating the change of the diameter of the droplet with distance, it is necessary to analyze the PDA measured parameter. The PDA measures the size of the droplets passing the measurement volume and records the number of the droplets in bins of 0.1 µm. In a simplified form, the number of counted droplets in a specific location depends on the concentration of the droplets at that location, the cross-sectional area of measurement volume, the velocity of the droplet, and the measurement time. If we assume that the droplet crosses the measurement volume in a direction that is perpendicular to the crossectional area then the number count can be expressed as follows

$$Count \propto S \times \Delta t \times U \times conc. \qquad \textit{equ. 32}$$

Where S is the cross-sectional area, Δt is the measurement time, U the droplet velocity, and conc. is the droplets concentration. *Figure 3.17* shows that the velocity of the droplets at a specific location doesn't change with their size for the two droplets populations. Since the measurement time is constant and the cross-sectional area of the measurement volume is also constant, then the count is directly related to the concentration in the location. So, in the following analysis of the

droplet size, the count graphs represent the concentration wherever the droplets velocity doesn't change with droplet size.

The exploration of the size of the droplets along the jet centerline is conducted in two steps each comprises a separate experiment. The first experiment focuses on the field near the nozzle, up to 0.05 m downstream, where the second experiment goes up to 0.4 m further downstream. At the level of the nozzle exit, there are two main droplet groups; the droplets generated by the VOAG -35 µm-70µm- and the droplets generated by the bubble column humidifier, in the range of 0.1 µm - 7.5 µm (shown in *Figure 3.6*). In the following discussion, we will examine the diameter change in each group separately.

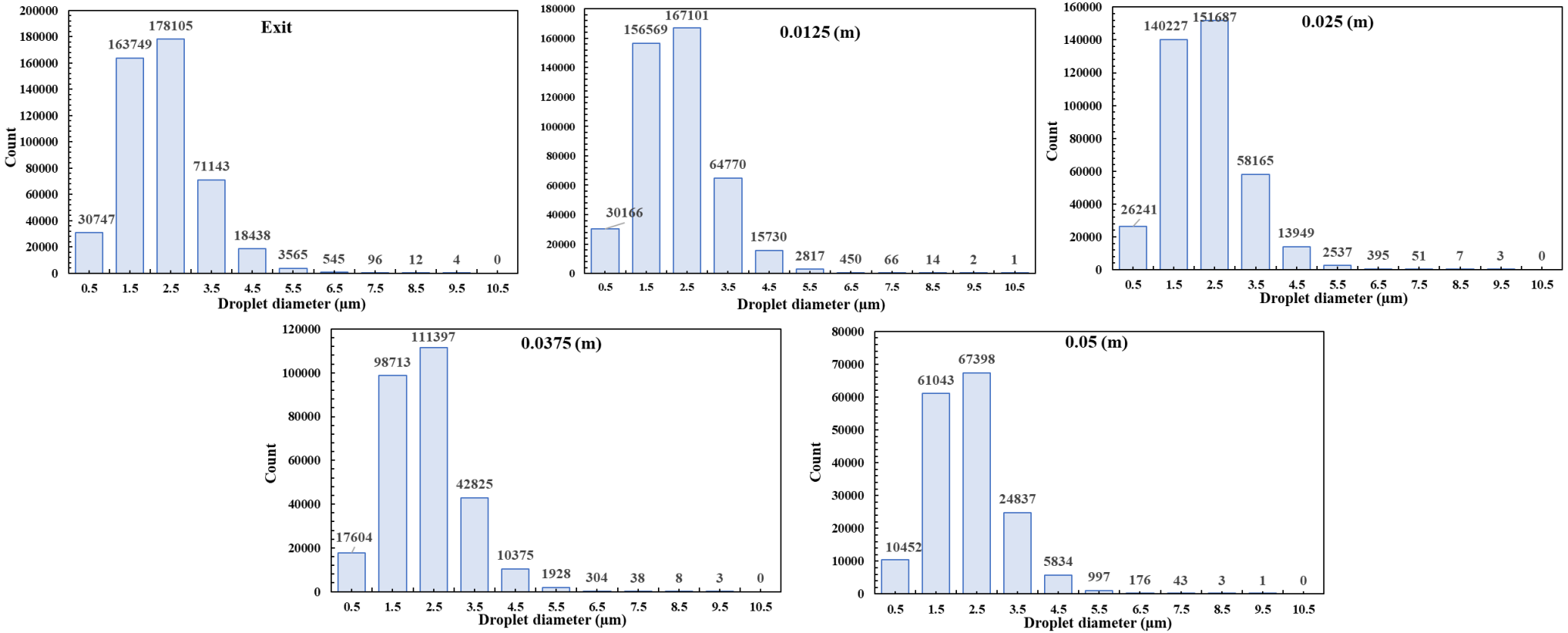

Figure 3.19 The change of count distribution of the droplets <10μm along 0.05 m of the jet centerline. (E1, measurement time at each point: 15 mins)

The count distribution of the droplets of less than 10 µm diameter measured near the exit, at 0.0125 m, 0.025 m, 0.0375 m, and 0.05 m are shown in *Figure 3.19.* As discussed before, the count distribution represents the size distribution because the velocity of the droplets at each location does not depend on the droplet's diameter as shown in *Figure 3.17*. The size distribution is illustrated in bins of 1 µm, and it is clear that the mode in all these distances is between 2 µm and 3 µm with more than 98.5 % of the droplets of less than 5 µm diameter. It is necessary to recall that the first three points fall inside the jet core, where only a slight change of the jet dynamics can be noticed. To address the effect of evaporation and jet dilution of the jet, *Figure 3.20* compares the size distributions in this size range. The figure presents the distribution of droplets in bins of 0.1 µm, as measured by the PDA system.

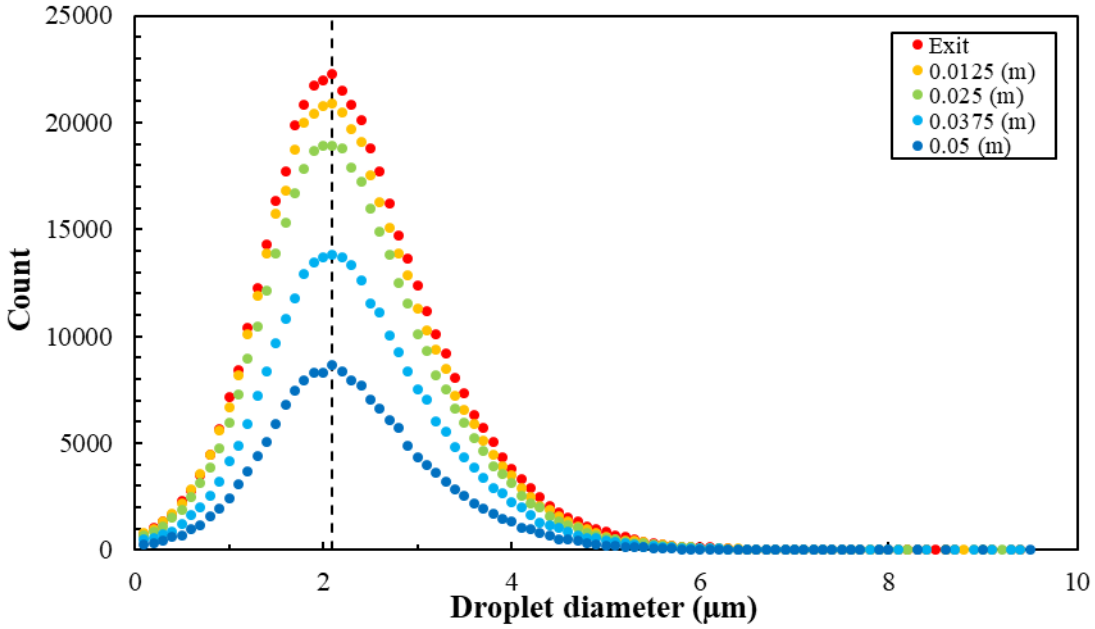

Figure 3.20 Comparison between the droplet count of the droplets <10µm along 0.05 m of the jet centerline. (measurement time at each point: 15 mins)

Figure 3.20 shows how the mode of these size distributions is 2.1 µm. If we assume that evaporation should produce a shift of the size distribution mode to the left, we might state that no significant evaporation occurs in the centerline of the humid jet. Moreover, the evaporation time of a 2.1 µm water droplet at 28 °C and 91.5 % relative humidity -conditions at 0.05 m from nozzle exit- is 0.046 s which is fourth folds the time needed to reach the distance of 0.05 m from the exit. However, the number of the counted droplets decreased by 63.5% in the first 0.05 m from the exit. This decrease in the number of droplets with distance from the nozzle can be attributed to two reasons. The first reason is the decrease in the droplets velocity as the number of droplets shown in *Figure 3.20* is the number of the droplets crossing the measurement volume within a constant acquisition time of 15 minutes. The second reason is the decrease in the concentration of the droplets due to jet expansion.

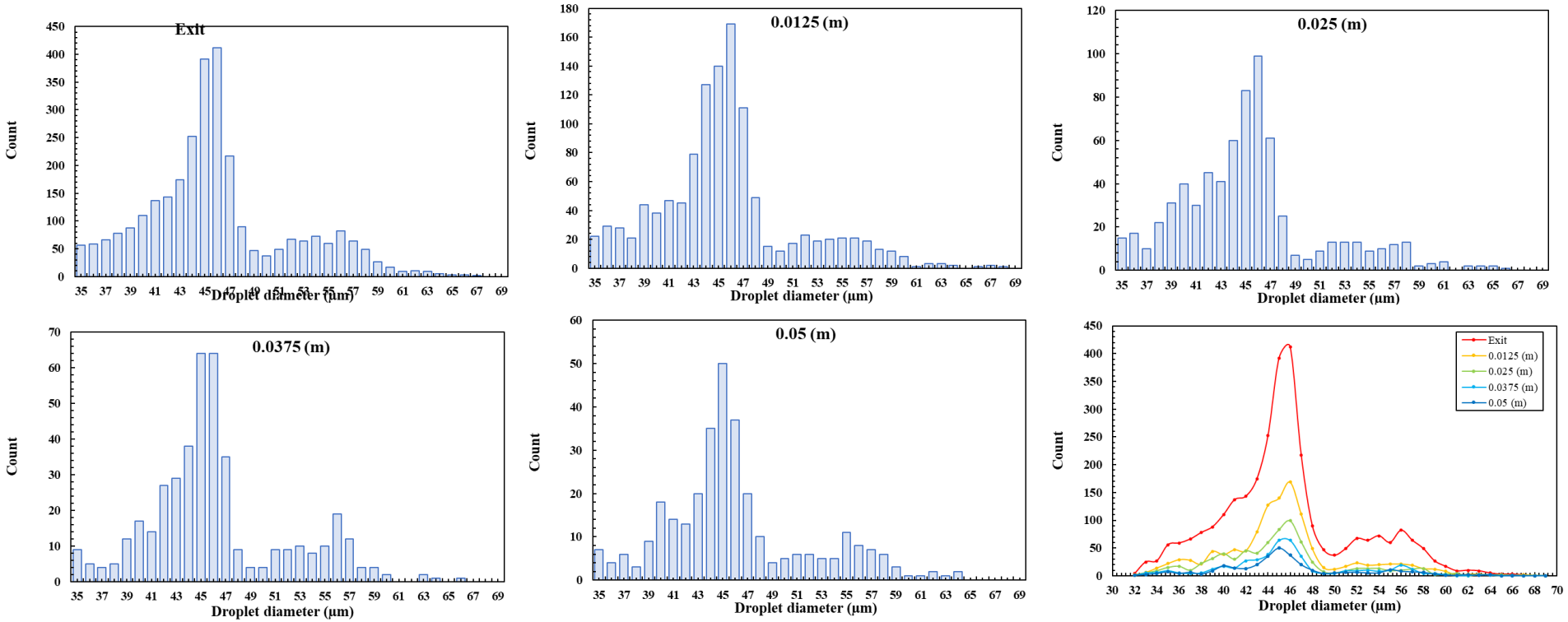

Figure 3.21 change of count distribution of the droplets 35 μm – 70 μm along 0.05 m of the jet centerline. (E1, measurement time at each point: 15 mins)

The change of the size distribution of the VOAG-generated droplets in the first 0.05 m from the exit is presented in *Figure 3.21* for experiment E1. The size distribution near the exit shows the droplets ideally produced by the VOAG in the range of 35 µm - 49 µm. The mode of these droplets falls in the bin 46 µm-47 µm. This mode remains the same up to 0.025 m. After, a similar number of droplets is measured in the bins 45 µm-46 µm and 46 µm - 47 µm. At 0.05 m, the mode shifts to 45 µm -46 µm bin. A percentage of 41.5%, 25.1%, 14.6%, and 10.8% of the droplets initially counted at the exit was observed at the distance of 0.0125 m, 0.025 m, 0.0375 m, and 0.05 m, respectively.

The droplets of a diameter more than 49 µm are double droplets generated by the VOAG due to the adaptions made in the dispersion and dilution flow systems. The volume of two 45 µm droplets is equivalent to the volume of a 56.7 µm droplet, the number of these doubles is less than 20% of the total number. The number of these droplets decreases at about the same rate as the droplets ideally generated by the VOAG. The decay in the number of the VOAG-generated droplets with distance is very high when compared to the smaller droplets of less than 7.5 µm.

A second experiment, E2, was carried out to explore the change of the size distribution further downstream up to 0.4 m with a step of 0.05m on the jet centerline. The results of the experiment are shown in *Figure 3.22* for the droplets of less than 10 µm. The mode changed from 2.1 µm near the jet exit to 1.9 µm at 0.05 m and 0.1 m and to 1.8 µm at 0.15 m. The droplets count decreased significantly over the distance since the count at 0.05 m and 0.1 m are 45.4% and 4.3% of the count at the nozzle exit.

Likewise, the droplet generated by the VOAG, in the size range of 35 µm -70 µm decreased significantly with distance. The total number of the droplets measured during 15 minutes at the exit in this size range is 705, with a majority of the droplets range between 48 µm -49 µm. 10% of these droplets are counted at the distance of 0.05m, with the majority of the droplets between 47 µm - 48 µm. The size distribution of the droplets measured near the exit and at 0.05 m, 0.1 m, and the comparison between them is shown in *Figure 3.23*. At 0.1 meter downstream, the number of the counted droplets of a diameter larger than 35 µm is 5.8% from the number measured at the exit. Further downstream at 0.15 m, 0.2 m, 0.25 m, 0.35 m, and 0.4m only 6, 3, 5, and 2 droplets were recorded, respectively, during the 15 mins measurement time. No droplets were detected at a distance of 0.35 m.

In addition to the concentration decay because of the jet expansion, the decrease of the droplets count might be due to gravity. The study of Bourouiba et al. [2014] shows that some of the droplets leave the jet and follow a ballistic trajectory.

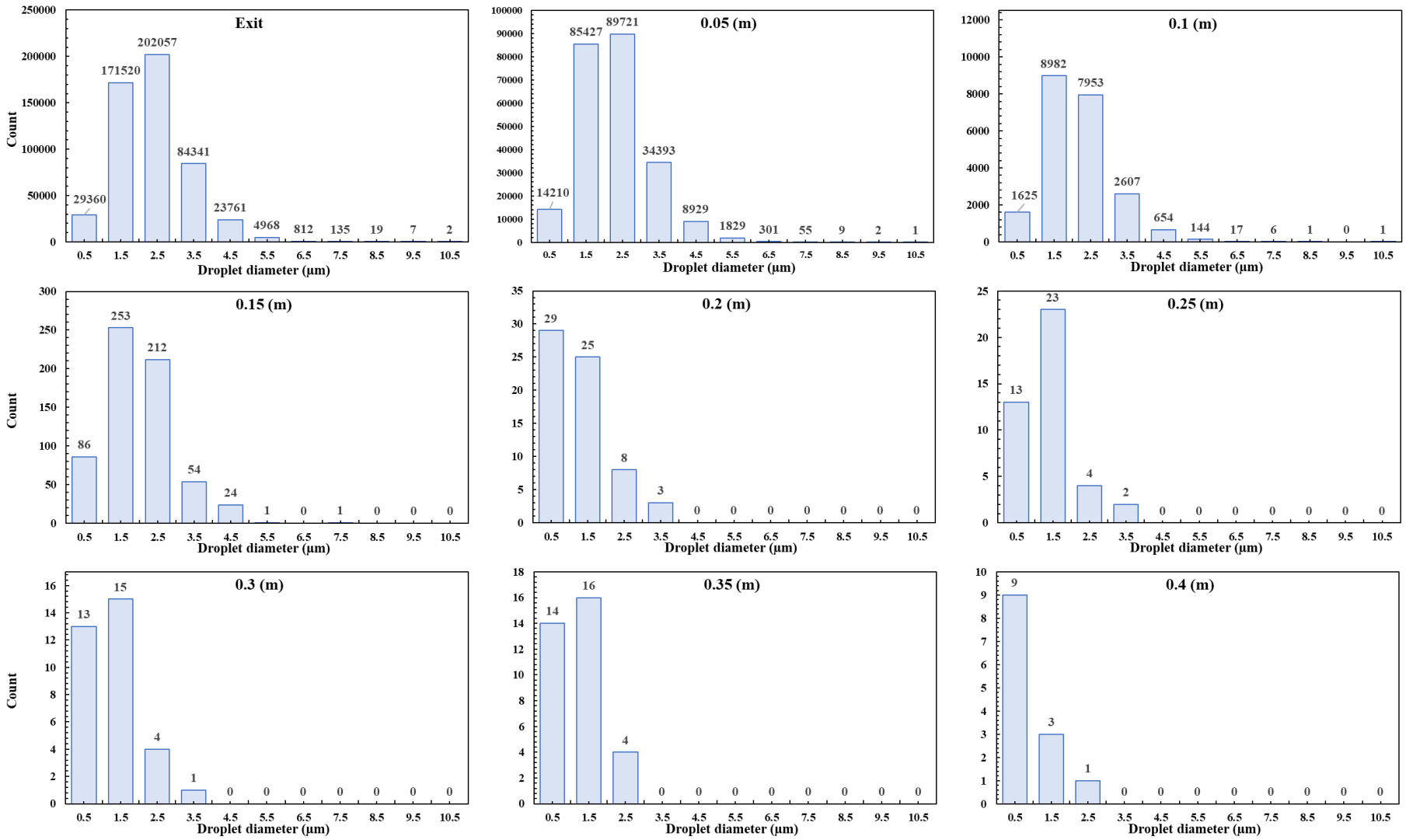

Figure 3.22 The change of count distribution of the droplets <10μm along 0.4 m of the jet centerline. (E2, measurement time at each point: 15 mins)

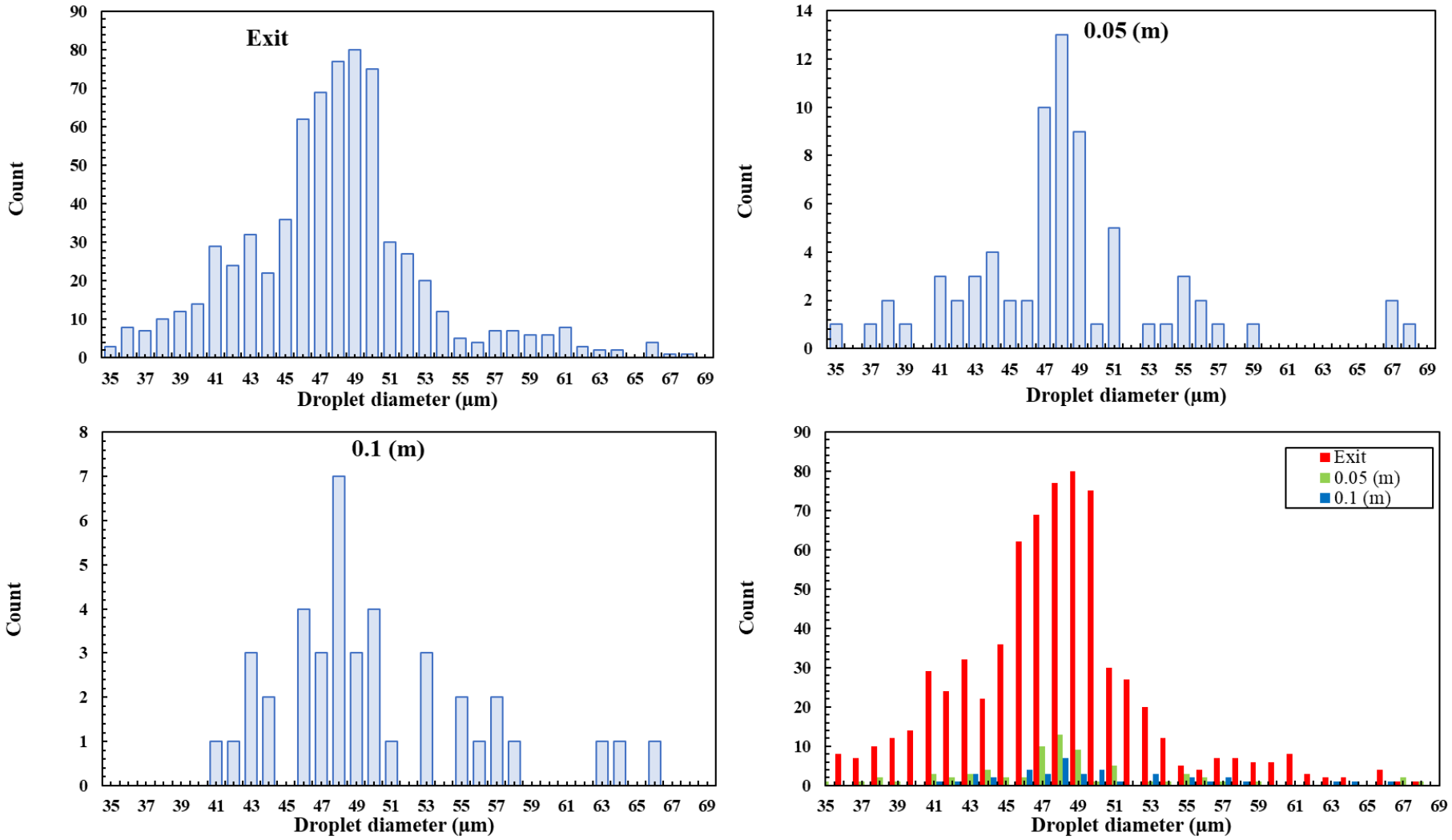

Figure 3.23 The change of count distribution of the droplets 35 μm – 70 μm along 0.1 m of the jet centerline. (E2, Measurement time at each point: 15 mins)

3.4.3 Measurements of the droplets on the vertical profiles

In addition to the exploration of the dynamics of the droplets on the jet centerline, vertical profile measurements were made on the central plane of the humid jet at 0.05 m, 0.1 m, 0.15 m, and 0.2 m. The measurements were made at 5 points above and under the jet centerline. To analyze the distribution of the droplets along the vertical profile, the count number for the two droplet groups is plotted at each point.

Figure 3.24 shows the number of the droplets less than 10 µm and between 35 µm - 70 µm measure at the vertical profile at 0.5 m from the jet exit. The graph on the left shows that the maximum number of the droplets -202377 droplets- is measured at the center of the jet. The As shown in *equ. 32*, the droplet count depends on the velocity of the droplet, and in this vertical profile the velocity ranges from almost zero near the jet border to its maximum at the jet center. Hence, the count graphs shown in *Figure 3.24* combine the effect of the radial evolution of the velocity as well as the concentration. Similarity, in the *Figure 3.26*, *Figure 3.27* and *Figure 3.30* these graphs gives information about the droplet count at each point but counts from two points are not comparable.

As the total number of droplets in the range of 35 µm - 70µm measured at this distance is relatively low, there are no droplets measured near the jet border. The figure on the right shows that the number of the droplets counted above and under the centerline is almost the same, which indicates that at 0.05m from the source these droplets are momentum-driven, and the effect of gravity and buoyancy is not significant.

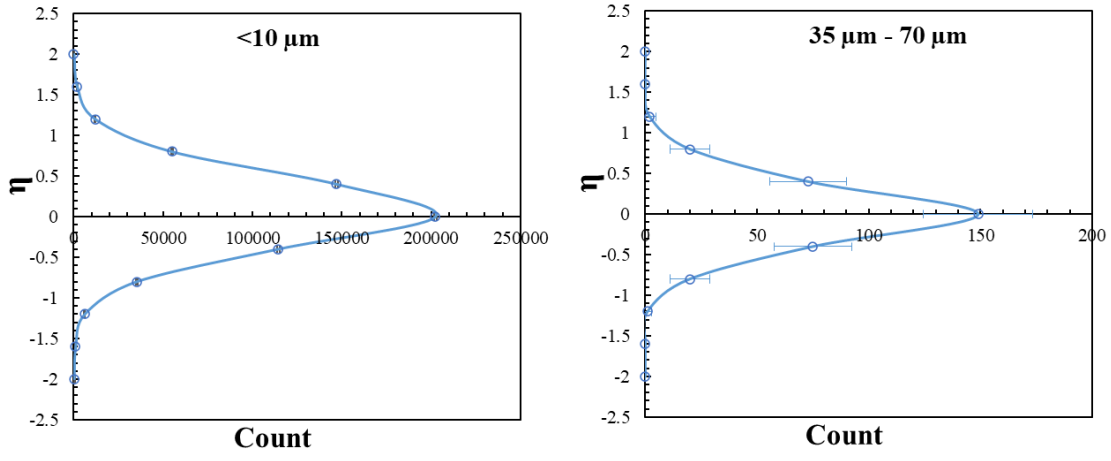

Figure 3.24 The number of the droplets along the vertical profile at x= (0.05m + 0.003m) from the exit (Measurement time at each point: 15 mins)

Figure 3.*25* shows the size distribution of the droplets in the range of 35µm -70 µm at the vertical profile on x= (0.05m + 0.003m). Recall that all these measurements are conducted on the central plane of y=0 in the range of η= 2 to η =-2 where $\eta = \frac{z}{x\beta}$. The figure confirms the previous conclusion drawn from Figure 3.*24*. on the uneven distribution of the number of droplets above and under the jet centerline. Concerning the evaporation, there no change in the mode diameters on the radial explanation of the jet. On the jet borders, more mixing with the ambient air occurs, which highly affects the number of the measured droplets. The evaporation effect is also more likely to develop near the jet border. However, given the current emission source and measurement time, the number of droplets passing the measurement volume around the jet border is negligible.

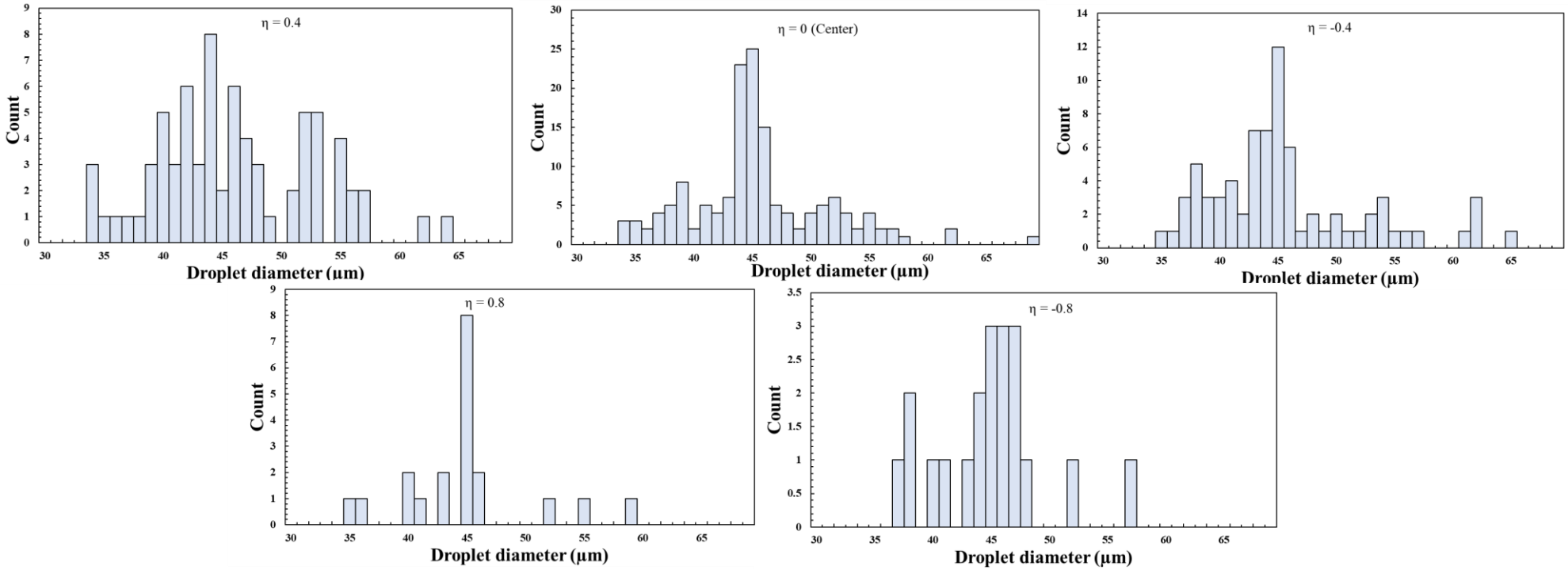

Figure 3.25 The size distribution along the vertical profile at x= (0.05m + 0.003m) from the exit at η=-0.8, -0.4, 0, 0.4, 0.8 (E3, measurement time at each point: 15 mins)

Before continuing on the discussion of the results obtained on the other vertical profiles, it is worth mentioning that each profile was examined in a separate experiment. Similar to *Figure 3.24*, the number of droplets observed at 0.1 m from the exit is illustrated in *Figure 3.26*. At this distance, the effect of the buoyancy forces becomes noticeable as the number of the droplets of less than 10 µm measured above the jet centerline is almost twice -192 %- the number under the centerline.

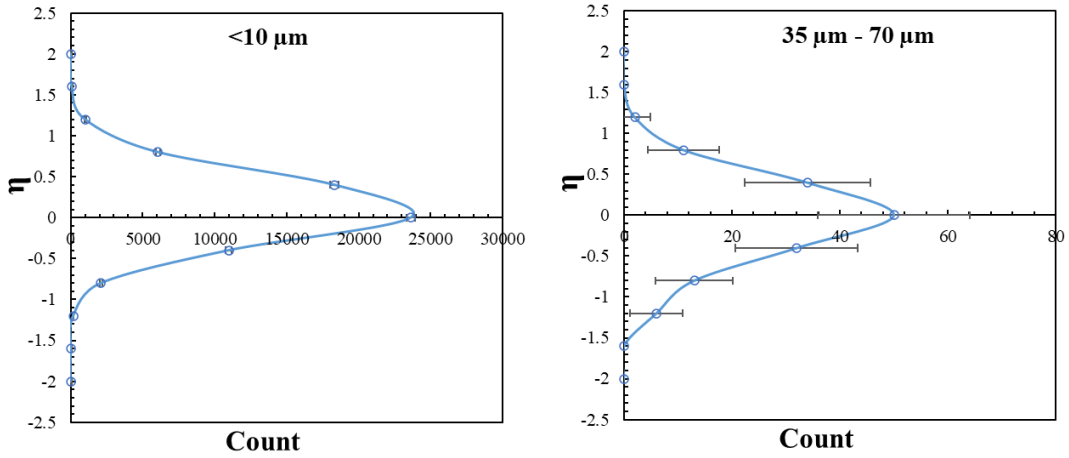

Figure 3.26 The number of the droplets along the vertical profile at x= (0.1m + 0.003m) from the exit (Measurement time at each point: 15 mins)

However, for the droplets in the range of 35 µm - 70 µm, there is no significant difference between the number of the droplet above and under the jet centerline. 47 droplets were measured above the centerline, while 51 were under the center. It is critical to draw a conclusion about the forces governing the dispersion of these droplets considering the low number of the measured droplets.

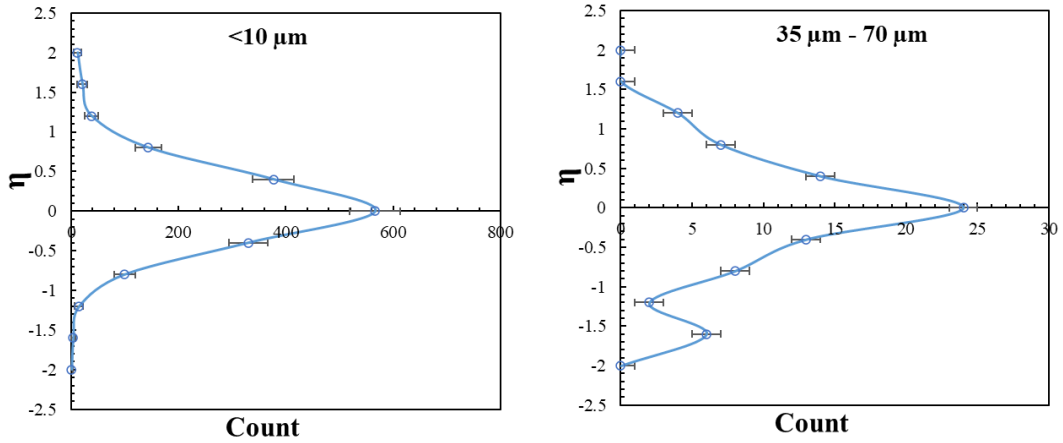

Figure 3.27 The number of the droplets along the vertical profile at x= (0.15m + 0.003m)from the exit (Measurement time at each point: 15 mins)

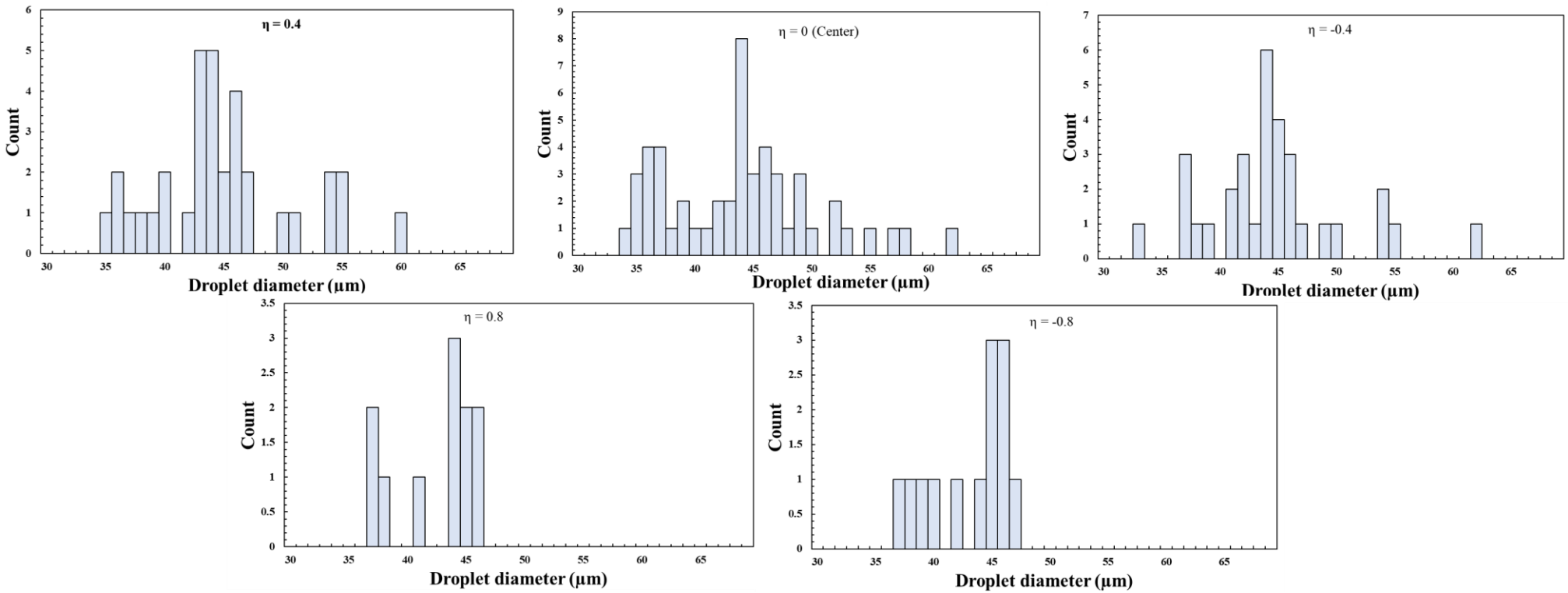

Figure 3.28 The count distribution along the vertical profile at x= (0.1m + 0.003m) from the exit at η=-0.8, -0.4, 0, 0.4, 0.8 (E4, measurement time at each point: 15 mins)

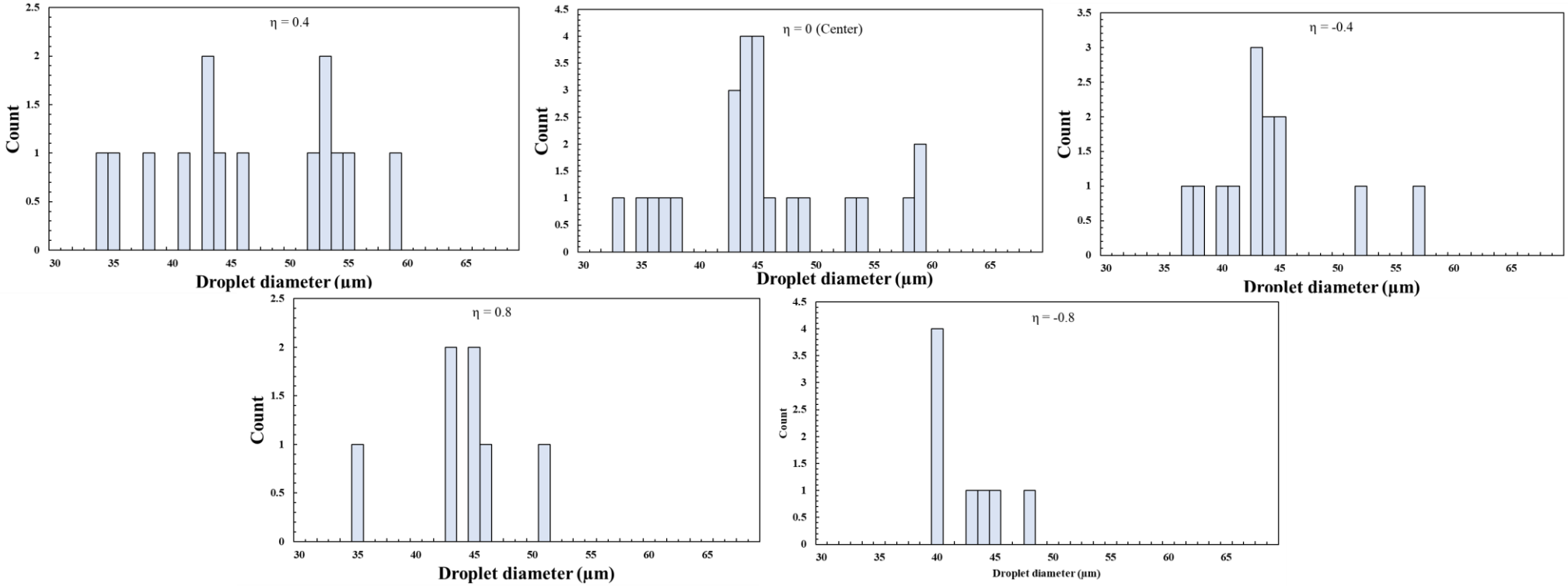

Figure 3.29 The count distribution along the vertical profile at x= (0.15m + 0.003m) from the exit at η=-0.8, -0.4, 0, 0.4, 0.8 (E5, measurement time at each point: 15 mins)

Similar to the size distribution on the vertical profile at x= (0.05 m +0.003m), the effect of the evaporation cannot be observed on the profiles at x= (0.1 m +0.003m), and x= (0.15 m +0.003m). Although, as the jet proceeds downstream more turbulent mixing is observed (see *Figure 2.44*, and *Figure 2.45*).

As the jet proceeds, the number of the detected droplets becomes very low. *Figure 3.27* and *Figure 3.30* shows the droplets measured at 0.15 m and 0.2 m, respectively. At 0.15 m the number of the droplets above the jet centerline is 130% of the count number under the centerline. At the same distance, a total of 78 droplets in the range of 35 µm -70 µm is measured with the maximum number of 24 droplets measured downstream.

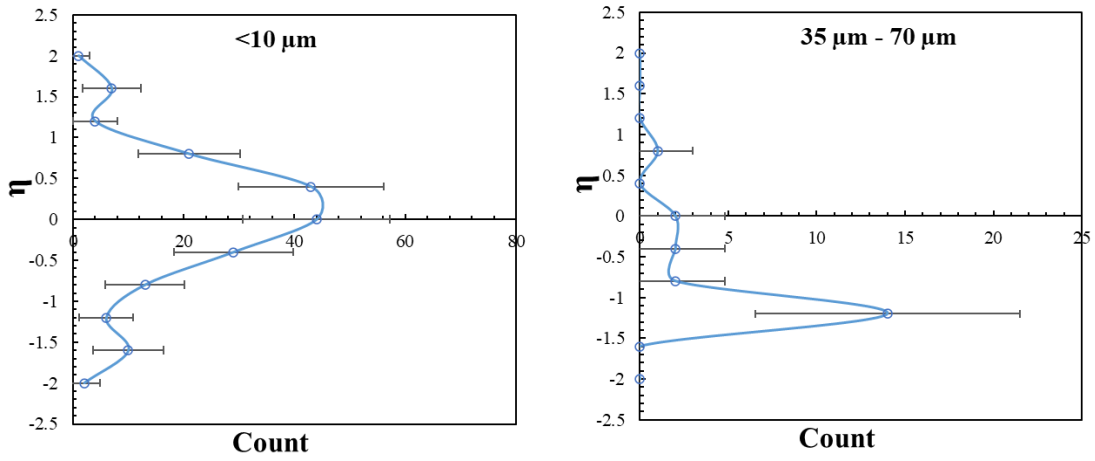

Figure 3.30 The number of the droplets along the vertical profile at x= (0.2m + 0.003m)from the exit (Measurement time at each point: 15 mins)

The center of the measurement's vertical line is kept unchanged for all the profiles. In other words, the measurement points weren't shifted upward to match the expected drift of the humid jet due to buoyancy. Thus, in *Figure 3.30*, the number of measured droplets of less than 10 µm at two central points is similar as the actual center lies between these points. Only three droplets in the range of 35 µm - 70 µm are observed above and on the jet centerline, while 13 droplets were counted at the third point under the center. More investigation is needed under the jet centerline before and after 0.2m from the jet exit to know if these droplets have a ballistic trajectory around this point.

3.5 Results on the dry residue of the NaCl-water solution droplets

Mahjoub Mohammed Merghani et al. [2020] discussed that the APS can only be used to measure the dry residues of human exhaled droplets. Similarly, here, the APS examines the size of dry residues of the NaCl-water solution droplets. Moreover, the PDA is a pointwise measurement technique, while the APS enables real-time measurement for the concentration of the particles inside the chamber. Hence, the results of the APS are complementary to those of the PDA and allows us to have a continuous evaluation of the droplets generated by the VOAG.

The air inside the environmental chamber is not filtered, so to analyze the size of the dry residues, measurements were conducted before emitting the droplets as well as during the experiment. *Figure 3.31* presents in black color the size distribution of the background particles before introducing the generation of the emission simulator. The results shown here are carried out on the 11th of March during E4 and E5 (see Table 3:2). They are discussed as an example, and the APS results for all the experiments are provided in Annex B. The frequency illustrated in the graph is the sum of 90 samples recorded in 15-seconds sampling intervals. These measurements show that initially there is a relatively high concentration of particles of less than 4µm. The mode of the particles formulated after the drying process of the NaCl-water solution droplets is 9 µm aerodynamic diameter.

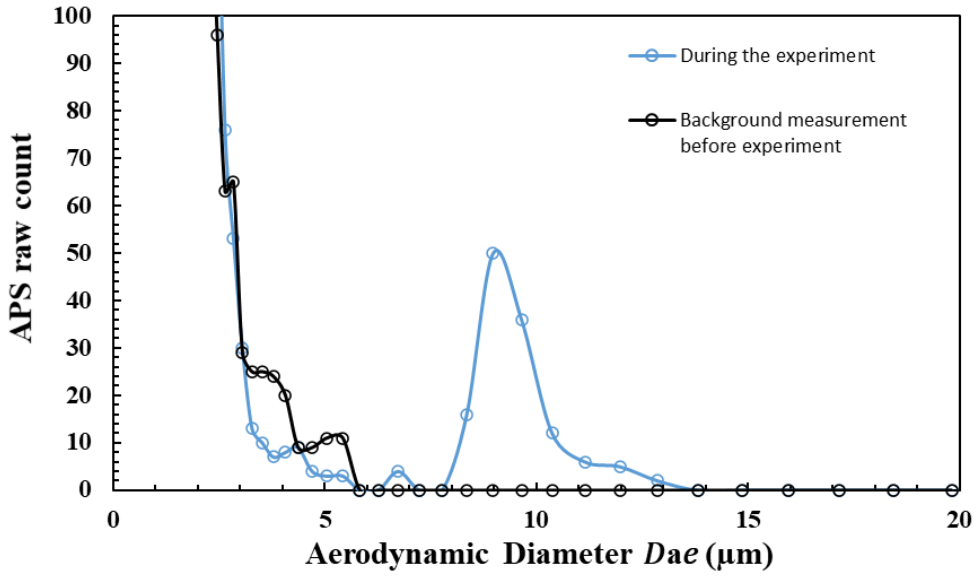

Figure 3.31: The concentration of the particles inside the environmental chamber before starting the VOAG generation (background) and during the experiment. (Measurement duration:15 mins)

The measurement conducted using the APS estimates the size distribution of the dry residues which can be obtained by PDA. With the APS measurements, it is possible to estimate the initial size of the droplets from the size of the dry residues measured by the APS. The relationship between the droplet's initial diameter ($D_{droplet}$) and the aerodynamic diameter of the dry residues $D_{dry\ residue}$ measured by the APS can be expressed using *equ. 33*.

$$D_{droplet} = D_{dry\,residue} \times \rho_r^{\frac{1}{2}} \times \rho^{\frac{-1}{6}} \times C_m^{\frac{-1}{3}} \qquad \textit{equ. 33}$$

Where ρ is the density solid residues, and ρ_r is the reference density ($\rho = 2170$ g.L^{-1} and ρ_r=1000 g.L^{-1}) and C_m is the mass concentration of NaCl of the initial droplets (10 g.L^{-1}) .

The estimation of the initial droplet size from the aerodynamic of the dry residues using *equ. 33* is illustrated in *Figure 3.32*. By comparing the two size distributions, we found that the mode of the initial droplets of the dry residues measured by the APS is between 36.6 µm and 39.3 µm. This mode is lower than the mode measured by the PDA, 46 µm.

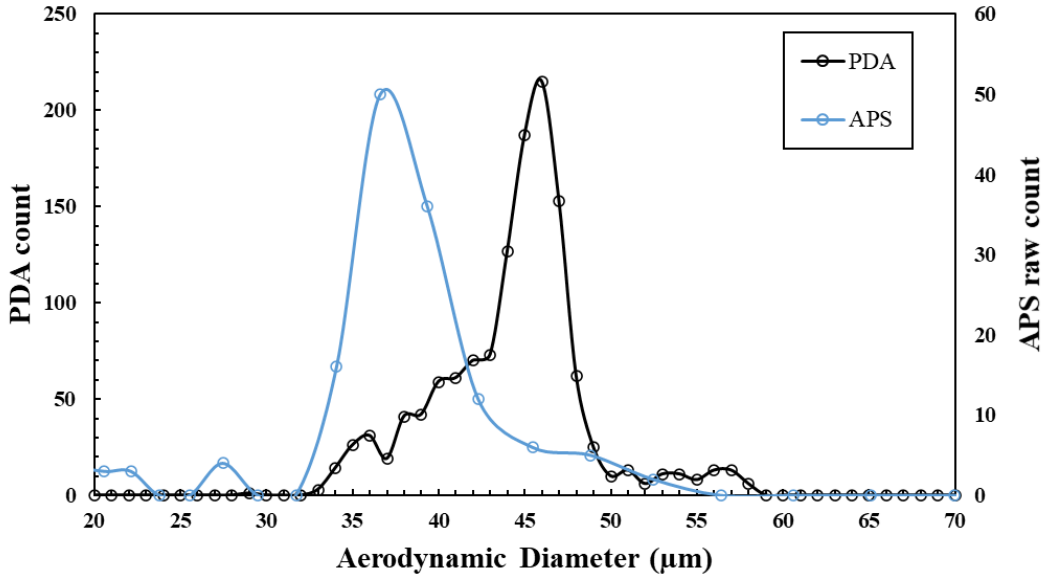

Figure 3.32: Prediction of the initial NaCl-water solution droplets from the size of the dry residues

To investigate this difference in between the results of the PDA and APS, we can calculate the initial size of the droplets using the VOAG parameters. The initial size of the droplets produced by the VOAG could be calculated by the following equation.

$$D_d = \left(\frac{6\,Q}{\pi\,f}\right)^{\frac{1}{3}} \qquad \textit{equ. 34}$$

Where Q is the liquid flow rate of the VOAG (2.3 x 10^{-9}, f is the VOAG frequency(69 kHz). So the droplet diameter that is theoretically produced by the VOAG is 39.96 µm which is convenient with the results obtained from the APS measurements. The larger droplet diameter measured by the PDA might be due to droplet growth inside the nozzle. This droplet growth issue could be addressed in the future modification of the OES.

3.6 Conclusion

The objective of the first part of this chapter was to develop an oropharyngeal emission simulator that generates monodispersed droplets of water-NaCl solution based on the previous version of the simulator that was established in a previous project, Primequal.

The second version of the simulator OES V.2 generates a humid airflow with a controlled temperature and velocity. Although the airflow conditions are stable the interaction between the water-NaCl droplets is very complex, which led to changes in the initial size distribution of the droplets. Two development suggestions could improve the measurements results:

- Using a filter at the exit of the bubble column humidifier which will eliminate the appearance of the small droplets of less than 7.5 µm.
- Control the humidity level inside the nozzle will regulate the size distribution of the droplets at the nozzle exit.

The existence of droplets of less than 7.5 µm allowed tracking the air velocity. The droplet produced by the VOAG accelerates at the first 0.025 m after the nozzle exit where it nearly reaches the air velocity. The velocity of the droplets decreases as the flow proceeds, however, there is not enough data to obtain statistics about droplets velocity.

This significant decrease in the droplet count with distance from the source has two reasons, the decay of the velocity downstream and the concentration decay due to jet expansion. Yet the effect of the jet expansion is more significant than the velocity because the velocity of the droplets produced by the VOAG at 0.05 m is higher than the velocity at the nozzle exit (*Figure 3.17*, *Figure 3.18*) a significant decay is noticed (*Figure 3.21*, *Figure 3.23*).

Future experiments could explore the concentration decay by adjusting the measurement proportional to the droplets velocity at the measurement location.

No evaporation is detected in the near field for the two droplet populations, and in the far-field, the data rate was not enough to draw conclusions about the droplet's evaporation.

Chapter 4
General conclusion and perspectives

Our current understanding of the transmission of infectious diseases can be traced back to the 1890s, when Flügge [1897] demonstrated that the droplets expelled during exhalation carry pathogen, and these droplets could transfer pathogen from one person to another when they are in close contact. Currently, this transmission route is referred to as droplet transmission. It was not until the 1930s when we understood that droplets can be transported further and so pathogens. It is the study of Wells [1934] that revealed another dominant route of transmission, airborne transmission. Wells studied the evaporation of the droplet and their falling rates as a function of the initial size and built an evaporation curve based on a simple calculation technique. This curve shows that the droplets of >100 µm fall quickly due to the gravitation effect, and the droplets of <100 µm evaporates and fall further at about 2 m. Based on Wells' study the 2 m of social distancing role is applied during the Covid19 outbreak, however, no proceeding study confirmed this exposure distance.

Wells distinguishes between two transmission routes, the droplet route that occurs when large droplets transfer directly from host to host, and the airborne route that occurs when initially emitted small droplets or dry residues/droplets nuclei evaporates, remain suspended in the air, and get transported by the airflow. Although this definition is still used, it is worth mentioning that the Wells' evaporation curve addresses droplets' evaporation in an ambient environment of 0% relative humidity and 18°C. These conditions are different from the initial conditions of the human exhalation as the expelled air is humid, and its temperature is around 34°C. In addition, the effect of the ambient air is not taken into account. Despite the importance of the initial droplet size on its fate, not considering these parameters questions this cutoff diameter, and how far these droplets can travel. Xie et al. [2007] revisited Wells' curve to numerically evaluate the effect of initial velocity and ambient humidity. Because there is no experimental data on the dynamics of droplets in motion -due to the sophistication of tracking moving droplets- numerical studies -which are dominate in this research area- rely on experimental results from free falling droplets or stagnant droplet.

In the first Chapter of this manuscript, we report a comprehensive review of the experimental techniques implemented to study the characterization of oropharyngeal droplets. Early experimental studies on the characterization of the exhaled droplets were focused on determining the initial size distribution of the exhaled droplets. Experimental techniques like solid impaction, optical particle counter, and aerodynamic particle sizer were used to measure the size of the exhalation particles. These techniques are intrusive techniques where droplets travel from the sampling point to the measurement point. This sampling process induces evaporation which

makes these techniques only suitable for the measurements of the dry residues and not the initial or evaporating droplet size.

Later, non-intrusive techniques such as high-speed photography and the Laser measurement techniques based on Mie theory were used to measure the size of the droplets. The laser measurement techniques can be applied to measure the size of the droplets at different distances from the source and allow investigation of the evaporation of the droplets. However, the measurement volume of these techniques is very small in comparison with the volume of the exhaled jet which makes it difficult to estimate the emission rate and the concentration. The later advancement in high-speed photography provides means for the tracking of the exhaled droplets clouds to estimate how far droplets can travel as well as illustrating their trajectory. Recently, digital inline holography was applied to visualize the shape of the exhaled droplets and to estimate their size in the surrounding environment.

The initial size of the droplets was estimated in the literature using two techniques, the first technique was the solid implication. In the solid impaction, the size of the initial droplets was estimated using a correlation between the size of the dry droplet spots impacted on a plate and the initial size of the droplet. Another study measured the size of the droplets at two different locations using Mie Imaging (IMI) technique. The size distributions in the two locations were compared to evaluate the evaporation and then estimate the initial size distribution of the droplets.

After the release of the droplets, they interact with the airflow resulting from the combination of the exhaled jet and the surrounding. In addition to the review of the experimental techniques applied to the exhaled droplets, we also reviewed the techniques utilized to study the exhaled airflow and its propagation in the ambient environment. Schlieren photography and high-speed photography techniques show how the air exhaled during the different exhalation activities propagates in terms of propagation velocity, direction, and propagation distance. Meanwhile, quantitative velocity measurements of the exhaled flow could be obtained by PIV or pointwise anemometers.

The conclusion of the review is that there is a lack of experimental results on the dynamics of the exhaled droplets. The exiting studies were focused on the characterization of the size distribution of initial droplets or the dry residues, meanwhile, the change of the size of the droplets with distance due to evaporation was not thoroughly investigated. Moreover, the interaction of the droplets with the airflow remains a critical gap in the understating of the transmission of infectious diseases.

The objective of this study is to explore the dynamics of the droplets in a humid buoyant turbulent jet. A steady jet of 34°C initial temperature, > 95 % relative humidity, and 5 m.s-1 initial velocities are considered in this study. The initial velocity of the flow corresponds to the initial velocity of speaking. In this work, the Laser doppler anemometry and phase Doppler anemometry measurement system are used. This technique is one of the non-intrusive techniques that have not

been yet used in this research field. It allows measuring the velocity and the size of the droplet, simultaneously. The study started by characterizing the gas velocity field of the turbulent jet in chapter 2, and then explored the change of the droplet's velocity and diameter at different distances from the source, in Chapter 3.

To explore the velocity field of the free humid buoyant jet, an environmental chamber was built to stabilize and monitor the ambient conditions. The chamber was designed while taking into account the confinement effect in the streamwise direction as well as the height considering the upward drift due to buoyancy. The air was laden with DEHS droplets which were used as a tracer for the Laser doppler anemometry measurement. We first investigated the isothermal jet configuration and compared velocity profiles as well as turbulence intensity profiles with models and experimental exiting literature. This investigation also allowed the development of an improved measurement procedure, addressing the problem of the flow instabilities. Using this procedure, we also examined the flow field of the buoyant jet configuration. A model of the velocity profile of the buoyant jet was developed based on an analytical model of the isothermal jet model using MATLAB. The model captures the buoyancy effect on the horizontal velocity profile, however, more analysis is needed for the radial velocity profiles. In conclusion, we identified the defining characteristic of the air jet, namely, centerline velocity decay, axial and radial velocity profile in addition to the turbulence levels in a flow field that is 0.8 m downstream the emitting nozzle.

The second part of this experimental study was dedicated to examining the change of the droplet's diameter and velocity with distance from the exit nozzle. In the context of this study, we developed a second version of an oropharyngeal emission simulator. The first version of the simulator was developed in a context of the frame of the Primequal program entitled "Study of the environmental determinants of viral exposure: application to the monitoring and management of respiratory viruses in classrooms". The OES V.2 generates humid air at controlled temperature and velocity laden with droplets of water-NaCl solution. Using the LDA/PDA system we measured the two velocities components and the optical diameter of the emitted droplets on the horizontal axis of the jet and at different locations for the vertical profiles.

We observed an unanticipated production of droplets of less than 10 µm, probably generated during the heating and humidification process of the air. Despite their unexpected generation these droplets allow measuring the velocity of the air, as they are small enough to be considered as a gas tracer. For these droplets and droplets generated by the OES, 35 µm -70 µ m, the change of the velocity along the centerline up to 0.4m distance was explored in addition to vertical profiles. Significant time was dedicated to the development process of the OES V.2 and the stabilization of the initial conditions of the jet. When reasonable experimental conditions were achieved, we conducted this exploratory measurement campaign. The analysis of the droplet count along the centerline and on the radial direction does not show the evaporation effect on the explored space. The mode of the size distribution, for both <10 µm droplet and the droplets generated by the OES,

doesn’t change in the first 0.05 m from the nozzle. For the droplets of <10 µm the mode changes from 2.5 µm at the exit to 1.5 µm at 0.1 m from the source to 0.5 µm at 0.4 m. This change in the mode indicates evaporation effect, however, the droplets count decreases significantly after 0.15 m from the nozzle, and the number of the measured droplets wasn’t enough to obtain rigorous conclusions after this distance. This decrease in the droplet count was more important for the droplets in the range of 35 µm -70 µ m with an initial count that is lower than the < 10µm droplets. No change in the mode of these droplets -48 µm- was observed in the near field.

However, in a humid jet, evaporation is expected to appear further downstream where the humidity level decreases. With the currently used experimental procedure the measurement time was fixed and the count at each point depends not only on the measurement time but also on the concentration and the velocity of the droplets at this location. The droplets' concentration changes due to both the jet expansion, as well as droplets' evaporation. As these effects are intertwined, we couldn't evaluate the decay of the number of droplets with distance due to the different mechanisms. Further analysis could be performed by developing a concentration decay model using the data acquired from the gas experiment where no evaporation occurs. The comparison between the predictions of this model and the acquired data could be used to estimate the evaporation rate.

Despite the increasing number of studies focusing on the transmission of airborne diseases especially after the COVID 19 epidemic, the results are contradictory and the significance of each of the transmission routes is not clear yet. The numerical models of the studies that investigate the behavior of the exhaled droplets after release are validated with experimental data of free-falling droplets, stagnant droplets, or suspended droplets. This study proposes a new methodology for tackling the problem by experimental exploration of the droplets dynamics in a well-defined gas flow field and providing quantitative data. These quantitative data could contribute to improving the results of the numerical studies and maybe bringing certain coherency to these results.

However, the significant contribution that numerical investigation could provide is to produce complementary information about droplet dynamics. The experimental technique adopted in this study provides mean quantitative values and combined with a Lagrangian numerical investigation, we could track within the jet flow a population of identified droplets. Although providing a detailed answer of what happens to the droplet after release in terms of temperature, pressure, and concentration change might be optimistic, it is the central question in infectious diseases transmission now. Because the comprehensive understanding of the transmission mechanisms can only be achieved when the droplet physical history is coupled with the biological characteristics of the pathogens. Moreover, the numerical study of the jet can provide a global picture of the velocity, temperature, and humidity fields.

In a complex flow field such as the one resulting from the interaction between the exhaled air and ambient environment, a global image of the flow provides a better interpretation of the results.

High-speed photography is a developing technique recently used to visualize the flow field and the propagation of the droplets in the ambient air. The images provided by high-speed photography capture the main aspects of the behavior of the droplets such as: falling out of the jet area after a certain distance, when the flow velocity becomes less than the droplet settling velocity or remain suspended in the air after a relatively long time which is a description proposed by a recent study using high-speed photography [Bourouiba et al., 2020]. Despite the importance of such a global field technique, the results are mostly qualitative as we talk about small and large droplets. The coupling of the technique applied in our study that provides quantitative information with these more global imaging-based flow field measurement techniques could be a significant improvement to help getting a more comprehensive understanding of the interaction between the droplets and the gas flow field.

Nomenclature

Symbols

A_0	Area of the jet opening	[m^2]
Ar_0	Archimedes number	[-]
Ar_x	Local Archimedes number	[-]
b	Jet width	[m]
C	Jet entrainment coefficient	[-]
D	Initial jet opening diameter	[m]
F	Froude number	[-]
g	gravitational acceleration	[$m.s^{-2}$]
Pr	Prandtl number	[-]
s	Length of the buoyant centerline curve	[m]
T_0	Initial jet temperature	[K]
T_∞	Ambient jet temperature	[K]
U_c	Centerline velocity	[$m.s^{-1}$]
U_o	Initial jet velocity	[$m.s^{-1}$]
U_x	Mean axial velocity component	[$m.s^{-1}$]
U_z	Mean Radial velocity component	[$m.s^{-1}$]

U_c	Mean centerline velocity	[m.s^{-1}]
u_x	Instantaneous axial velocity component	[m.s^{-1}]
u_z	Instantaneous Radial velocity component	[m.s^{-1}]
$\grave{u}_x$	Axial velocity fluctuations	[m.s^{-1}]
$\grave{u}_z$	Radial velocity fluctuations	[m.s^{-1}]
x	Axial distance from the source	[m]
z	Radial distance from the jet centerline	[m]
z_c	The vertical distance between the buoyant jet centerline and the jet horizontal axis	
x_o	The virtual origin of the jet	[m]
x_{exit}	The axial distance from the nozzle exit	[m]
N	The droplet number	
n	The number of the measurement points for each profile	

Greek Symbols

φ	Jet spread angle	[°]
η	Dimensionless radial distance from the jet centerline ($\eta = \frac{z}{(x+x_o)\beta}$	[-]
ρ_0	Initial jet density	[kg.m^{-3}]

ρ_∞	Ambient jet density	[kg.m^{-3}]
θ	Slope of the buoyant centerline tangent	[°]
ν	Momentum diffusivity	[m^2·s^{-1}]
α	Thermal diffusivity of heat	[m^2·s^{-1}]
$D_{droplet}$	The diameter of the droplet	[µm]
$D_{dry\ residue}$	The diameter of the dry residues of the droplets	[µm]
C_m	The mass concentration	[kg.m^{-3}]
ρ_d	The density of the droplet	[kg.m^{-3}]
ρ_r	The reference density (1000)	[kg.m^{-3}]

References

[Abdel-Rahman et al., 1997] Abdel-Rahman AA, Chakroun W, Al-Fahed SF. (1997) LDA measurements in the turbulent round jet. Mechanics Research Communications.

[Abramovich, 1963] Abramovich GN. Turbulent free jets of liquids and gases. Moscow, Russia.: Gosenergoizdat; 1963.

[Baturin, 1972] Baturin V (1972) Fundamentals of Industrial Ventilation, Pergamon Press, Oxford.

[Capp and George, 1982] CAPP,S . P. & GEORGE W, . K. 1982 Measurements in an axisymmetric jet using a two-color LDA and burst processing. Proc. Intl Symp. on Appl. of LDA to Fluid Mechanics (ed. P. Durao et al.), $1.2, Lisbon, Portugal.

[Chen et al. 2020] Chen W, Zhang N, Wei J, Yen H-L, Li Y. Short-range airborne route dominates exposure of respiratory infection during close contact. medRxiv. March 2020:2020.03.16.20037291.

[Chao et al., 2009] Chao, C., Wan, M., Morawska, L., Johnson, G., Ristovski, Z., Hargreaves, M., Mengersen, K., Corbett, S., Li, Y., Xie, X., and Katoshevski, D. (2009). Characterization of expiration air jets and droplet size distributions immediately at the mouth opening. Journal of Aerosol Science, 40(2):122–133.

[Corrsin and Uberoi., 1949] Corrsin, Stanley and Uberoi, Mahinder S. (1949) Further experiments on the flow and heat transfer in a heated turbulent air jet.

[Da et al, 2015] Da, Guillaume & Géhin, Evelyne & Gooly, Seehan & Delaby, Stéphane & Sebastien, Ritoux & Ha, Thi Lan & Robine, Enric. (2015). Investigation of exhaled particle dispersion in indoor environment: an experimental study in a classroom. The topic deals with the dispersion of exhaled droplets in a full-scale control environment.

[DANTEC, 2020] Measurement Principles of LDA. Dantec Dynamics | Precision Measurement Systems & Sensors. https://www.dantecdynamics.com/solutions-applications/solutions/fluid-mechanics/laser-doppler-anemometry-lda/measurement-principles-of-lda/. Accessed December 4, 2020.[Grimitlyn, 1982] Grimitlyn MI. Air distribution in rooms. Moscow, Russia: Stroiizdat; 1982.

[George, 1989] GEORGE, W. K. 1989 The self-preservation of turbulent flows and its relation to initial conditions and coherent structures. Advances in Turbulence (ed. W. K. George & R. E. A. Arndt), pp. 39-72. Hemisphere.[Kähler et al. 2002] Kähler C, Sammler B, Kompenhans J. Generation and control of tracer particles for optical flow investigations in air. Experiments in Fluids. 2002;33:736–742.

[Falcone, 2003] Falcone AM, Cataldo JC. Entrainment Velocity in an Axisymmetric Turbulent Jet. Journal of Fluids Engineering. 2003;125:620–627.

[Flügge, 1897] Flügge C. 1897. Über Luftinfection. Zeit. Hyg. Infektionskrankh. 25:179–224

[Guerra, 2004] D. Guerra. Modélisation du transfert d'un aérocontaminant dans un local ventilé en champ proche d'une source d'émission accidentelle. Thèse de doctorat, Institut National Polytechnique de Toulouse, 2004.

[Hinds, 1999] Hinds, William C. 1999. Aerosol technology: properties, behavior, and measurement of airborne particles. New York: Wiley.

[Hinze, 1975] Hinze, J. O., (1975) Turbulence. Second edition, Mc Graw-Hill serie in mechanical engineering.

[Hoppe, 1981] P. Hoppe. Temperatures of expired air under varying environmental conditions. International Journal of Biometeorology, 25(2):127–132, June 1981.

[Hussein et al., 1994] Hussein HJ, Capp SP, George WK. Velocity measurements in a high-Reynolds-number, momentum-conserving, axisymmetric, turbulent jet. Journal of Fluid Mechanics. 1994;258:31–75.

[Kukkonen et al. 1989] Kukkonen J, Vesala T, Kulmala M. The interdependence of evaporation and settling for airborne freely falling droplets. J Aerosol Sci. 1989;20:749–763.

[Kwon et al., 2012] Kwon, S.-B., Park, J., Jang, J., Cho, Y., Park, D.-S., Kim, C., Bae, G.-N., and Jang, A. (2012). Study on the initial velocity distribution of exhaled air from coughing and speaking. Chemosphere, 87(11):1260–1264.

[Lee and Chu 2003] Lee JHW, Chu VH (2003) Turbulent jets and plumes: a Lagrangian approach. Kluwer Academic Publishers, Boston

[List, 1982] List EJ. (1982) Mechanics of Turbulent Buoyant Jets and Plumes. In: Turbulent Buoyant Jets and Plumes. Elsevier.

[Liu et al. 2017] Liu L, Wei J, Li Y, Ooi A. Evaporation and dispersion of respiratory droplets from coughing. Indoor Air. 2017;27:179–190.

[Mahjoub Mohammed Merghani et al., 2020] Mahjoub Mohammed Merghani K, Sagot B, Gehin E, Da G, Motzkus C. A review on the applied techniques of exhaled airflow and droplets characterization. Indoor air. 2021 Jan;31(1):7-25. DOI: 10.1111/ina.12770.

[Melling, 1997] Melling A. Tracer particles and seeding for particle image velocimetry. Measurement Science and Technology. 1997;8:1406–1416.

[Mih, 1989] Mih WC. (1989) Equations for Axisymmetric and Two-dimensional Turbulent Jets. Journal of Hydraulic Engineering.

[Morton et al., 1956] Morton BR, Geoffrey Taylor FRS, Turner JS. (1956) Turbulent gravitational convection from maintained and instantaneous sources. Proceedings of the Royal Society of London Series A Mathematical and Physical Sciences.

[Orlu, 2009] Orlu R. Experimental studies in jet flows and zero pressure-gradient turbulent boundary layers. 2009.

[Papadopoulos and Pitts, 1999] Papadopoulos G, Pitts WM. A Generic Centerline Velocity Decay Curve for Initially Turbulent Axisymmetric Jets. Journal of Fluids Engineering. 1999;121:80–85.

[Reichardt, H., 1942] Reichardt, H. (1942). "Gesetzmassigkeiten der freien turbulenz." Forschungsheft 414,Verein Deutscher Ingenieure.

[Sarh, 1990] Sarh, B., "Contribution à l'étude des jets turbulents à masse volumique variable et des flammes de diffusion turbulentes. " Thèse de doctorat, université Pierre et Marie Curie, Paris, 1990.

[Schlichting, 1930] Schlichting H. Ueber das ebene windschaftenproblem. Ing Arch 1930;5.

[TSI, 2013] TSI. Vibrating orifice aerosol generator model PAID3450, User's manual. 2013.

[Wei and Li, 2015] Wei J, Li Y. Enhanced spread of expiratory droplets by turbulence in a cough jet. Building and Environment. 2015;93:86–96.

[Wygnanski and Fiedler, 1969] Wygnanski I, Fiedler H. Some measurements in the self-preserving jet. Journal of Fluid Mechanics. 1969;38:577–612.

[Xie et al., 2007] Xie, X., Li, Y., Chwang, A. T. Y., Ho, P. L., and Seto, W. H. (2007). How far droplets can move in indoor environments revisiting the wells evaporation falling curve. Indoor Air, 17(3):211–225.

[Zambrelli, 2014] Audrey Zambrelli, Suivi de Contamination Particulaire dans une Piece, Master thesis, 2014.

[Zhivov et al., 2020] Zhivov A, Skistad H, Mundt E, et al. (2020) Chapter 7 - Principles of air and contaminant movement inside and around buildings. In: Goodfellow HD, Kosonen R, eds. Industrial Ventilation Design Guidebook (Second Edition). Second Edition. Academic Press.

[Ferrand et al, 2003] Ferrand V, Bazile R, Borée J, Charnay G. Gas–droplet turbulent velocity correlations and two-phase interaction in an axisymmetric jet laden with partly responsive droplets. *International Journal of Multiphase Flow*. 2003;29:195–

Annexes

Annex A: The count distribution of the droplet at the nozzle exit

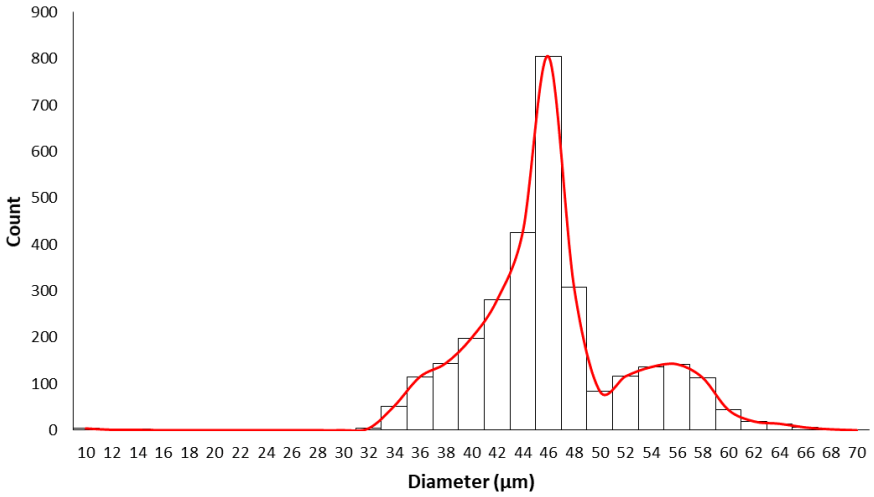

Figure: A-1 : Count distribution of the VOAG generation at (0.003,0,0) for E1

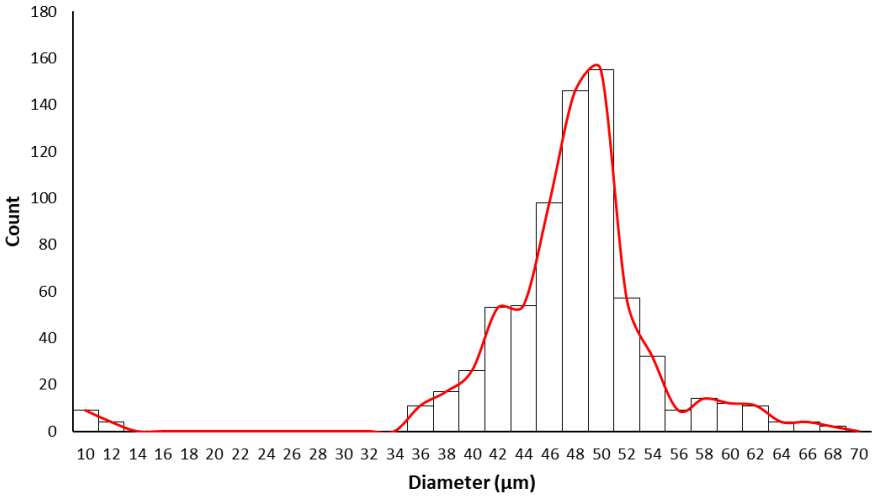

Figure: A-2 : Count distribution of the VOAG generation at (0.003,0,0) for E2

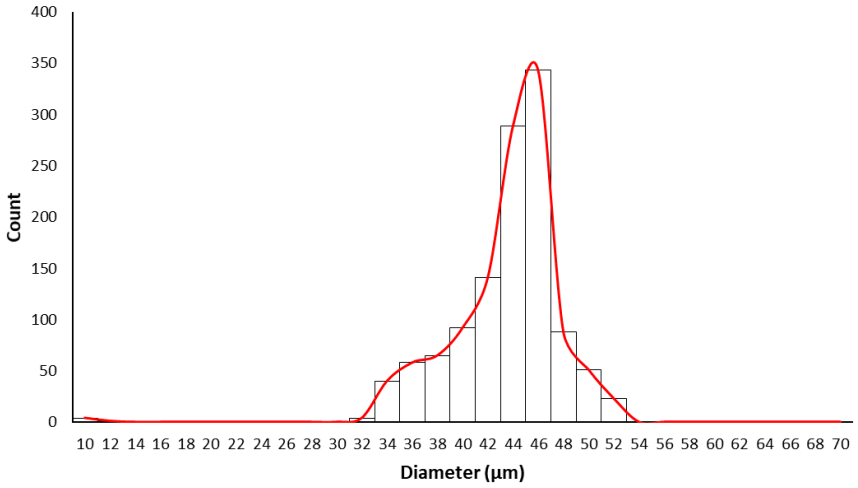

Figure: A-3 : Count distribution of the VOAG generation at (0.003,0,0) for E3

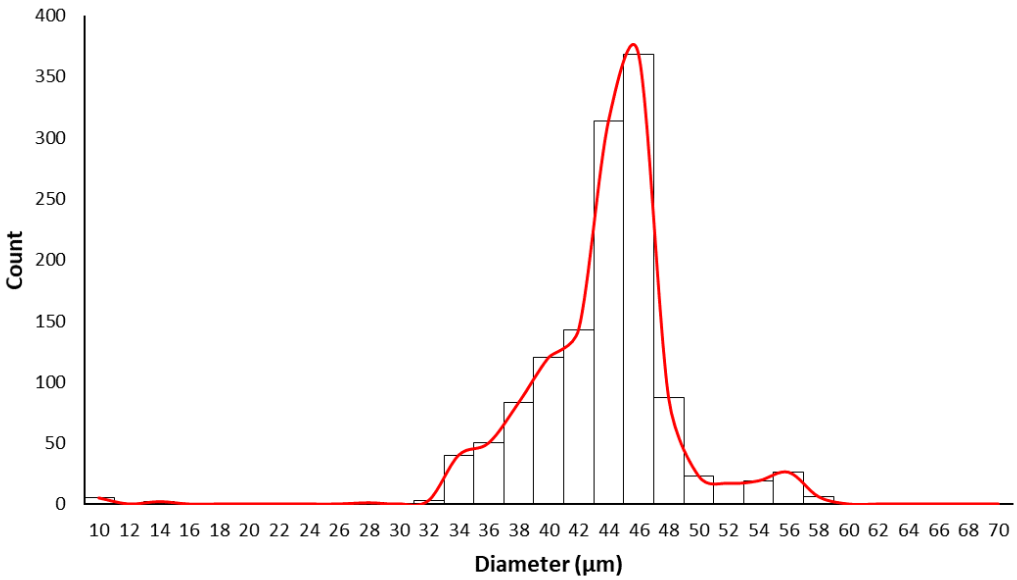

Figure: A-4 : Count distribution of the VOAG generation at (0.003,0,0) for E4

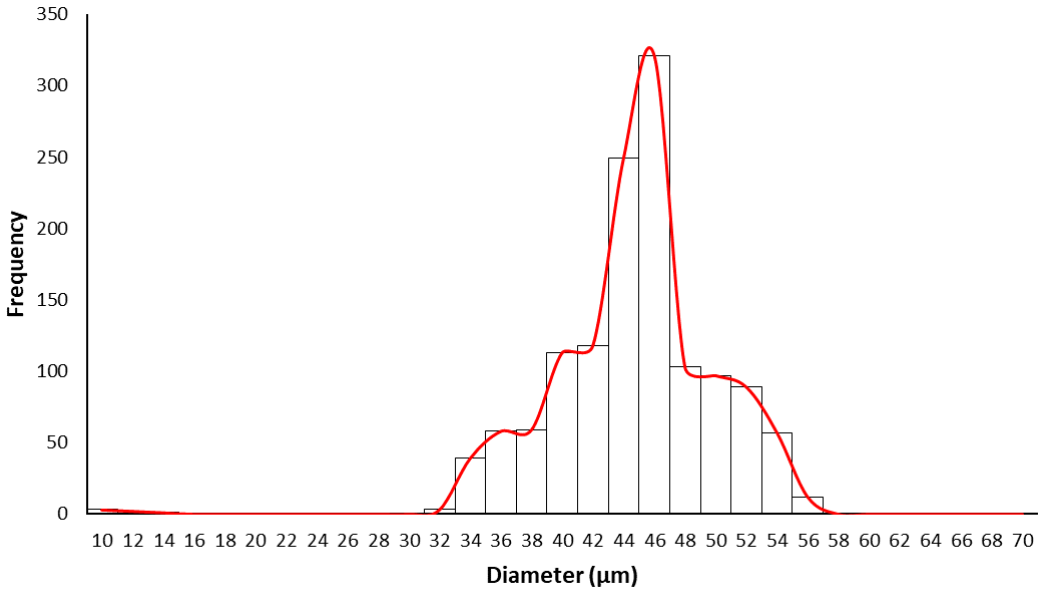

Figure: A-5 : Count distribution of the VOAG generation at (0.003,0,0) for E5

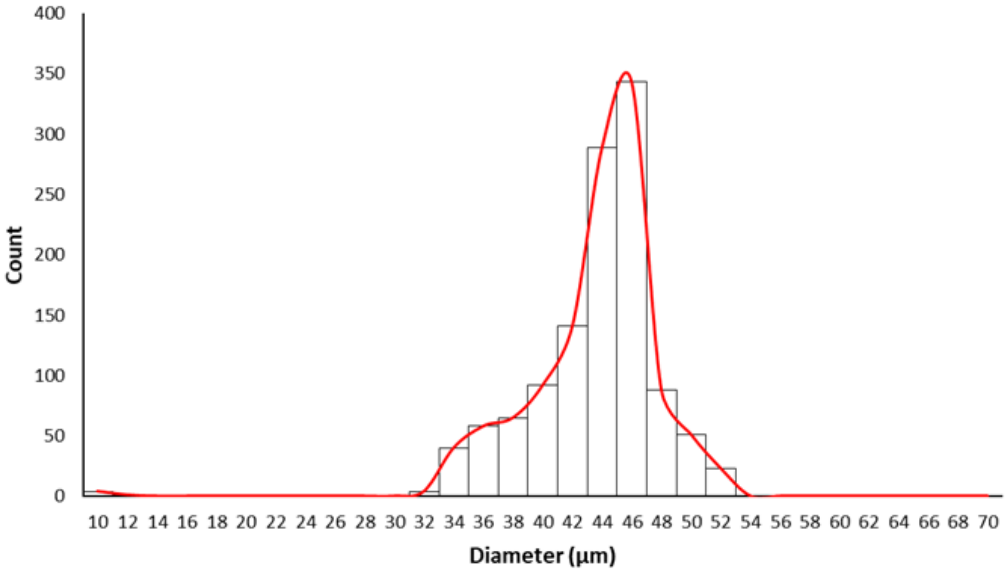

Figure: A-6 : Count distribution of the VOAG generation at (0.003,0,0) for E6

Annex B: The APS measurements of the dry residues of the NaCl-water solution droplets

Aerodynamic Diameter	Raw count					
	E1	E2	E3	E4	E5	E6
<0.523	86094	113605	590745	54223	45962	298930
0.542	7931	12059	57519	5649	5327	26923
0.583	6912	11611	50804	5484	5229	22570
0.626	6383	12280	46821	5764	5705	19614
0.673	5732	13873	42435	6354	6742	16705
0.723	5169	16403	34024	7229	8331	12344
0.777	4123	18370	21315	7895	9421	7566
0.835	3111	17954	10335	7606	8982	3920
0.898	2415	16700	5424	6990	8281	2214
0.965	1999	14355	3208	5931	7185	1382
1.037	1678	12114	2095	4875	6067	901
1.114	1381	9642	1574	3902	4920	586

1.197	1163	7675	1160	3131	4002	400
1.286	1024	6156	971	2607	3411	300
1.382	919	4842	703	2060	2585	252
1.486	811	3681	613	1542	2168	170
1.596	676	2710	545	1154	1603	155
1.715	591	1919	449	866	1159	124
1.843	505	1389	341	564	842	121
1.981	373	944	264	423	624	78
2.129	330	757	217	322	503	60
2.288	262	571	137	223	382	31
2.458	182	367	103	142	254	18
2.642	135	217	53	76	156	12
2.839	91	132	28	53	113	4
3.051	76	78	31	30	83	3
3.278	52	52	25	13	71	2
3.523	43	24	11	10	48	1

3.786	20	23	10	7	29	1
4.068	18	10	4	8	37	0
4.371	18	8	4	9	25	1
4.698	9	1	4	4	21	0
5.048	5	6	2	3	16	0
5.425	4	4	3	3	11	0
5.829	4	2	1	0	13	0
6.264	1	1	2	0	7	0
6.732	2	2	0	4	7	0
7.234	3	1	1	0	5	2
7.774	6	1	1	0	6	0
8.354	37	5	16	16	12	6
8.977	140	11	31	50	64	15
9.647	134	17	24	36	47	10
10.37	36	26	7	12	15	3
11.14	28	6	9	6	11	0
11.97	15	5	5	5	8	2

12.86	5	3	0	2	3	1
13.82	2	1	1	0	1	0
14.86	1	0	0	0	1	0
15.96	0	0	0	0	0	0
17.15	0	0	0	0	0	0
18.43	0	0	0	0	0	0
19.81	0	0	0	0	0	0

Table 0:1 The APS measurements of the dry residues of the NaCl-water solution droplets for E1,E2, E3, E4, E5, and E6.